

Deposition and Characterization of Magnetron Sputtered
Beta-Tungsten Thin Films

Jiaying Liu

Submitted in partial fulfillment of the
requirements for the degree of
Doctor of Philosophy
in the Graduate School of Arts and Sciences

COLUMBIA UNIVERSITY

2016

© 2016

Jiaying Liu

All Rights Reserved

ABSTRACT

Deposition and Characterization of Magnetron Sputtered Beta-Tungsten Thin Films

Jiaying Liu

β -W is an A15 structured phase commonly found in tungsten thin films together with the bcc structured W, and it has been found that β -W has the strongest spin Hall effect among all metal thin films. Therefore, it is promising for application in spintronics as the source of spin-polarized current that can be easily manipulated by electric field.

However, the deposition conditions and the formation mechanism of β -W in thin films are not fully understood. The existing deposition conditions for β -W make use of low deposition rate, high inert gas pressure, substrate bias, or oxygen impurity to stabilize the β -W over α -W, and these parameters are unfavorable for producing β -W films with high quality at reasonable yield. In order to optimize the deposition process and gain insight into the formation mechanism of β -W, a novel technique using nitrogen impurity in the pressure range of 10^{-5} to 10^{-6} torr in the deposition chamber is introduced. This technique allows the deposition of pure β -W thin films with only incorporation of 0.4 at% nitrogen and 3.2 at% oxygen, and β -W films as thick as $1\mu\text{m}$ have been obtained. The dependence of the volume fraction of β -W on the deposition parameters, including nitrogen pressure, substrate temperature, and deposition rate, has been

investigated. The relationship can be modeled by the Langmuir-Freundlich isotherm, which indicates that the formation of β -W requires the adsorption of strongly interacting nitrogen molecules on the substrate.

The dependence of β -W formation on the choice of underlayer materials has also been investigated. The β -W phase can only be obtained on the underlayer materials containing non-metallic elements. The dependence is explained by the existence of strong covalent bonds in β -W compared with that in α -W. The nickel and permalloy underlayers are the only exception to the above rule, and β -W has been successfully deposited on permalloy underlayer using very low deposition rate for spin-diffusion length measurement of β -W.

The permalloy thin films usually take the (111) texture, since its (111) planes have the lowest surface energy. However, permalloy thin films deposited on β -W underlayer can achieve (002) texture using amorphous glass substrates. Therefore, the permalloy/ β -W bilayer system can work as a seed layer for the formation of (002) textured films with fcc or bcc structure. The mechanism of the (002) texture formation cannot be explained by the existing models.

The β -W to α -W phase transition was characterized by differential scanning calorimetry. The enthalpy of transformation is measured to be 8.3 ± 0.4 kJ/mol, consistent with the value calculated using density functional theory. The activation energy for the β -W to α -W phase transformation kinetics is 2.2 eV, which is extremely low compared with that of lattice and grain boundary diffusion in tungsten. The low activation energy might be attributed to a diffusionless shuffle transformation process.

Table of Contents

List of Figures	iv
List of Tables	viii
Acknowledgements	ix
1 - Introduction	1
1.1 Introduction.....	1
1.2 Organization of the Dissertation.....	2
2 – Background and Motivation	4
2.1 Tungsten Thin Films in Electronics Industry.....	4
2.2 β -Tungsten Thin Films in Spintronics.....	5
2.2.1 Properties of β -Tungsten Thin Films.....	5
2.2.2 Spin Hall Effect in β -Tungsten Thin Films.....	6
2.3 Deposition of Tungsten Thin Films.....	10
2.3.1 Chemical Vapor Deposition.....	10
2.3.2 Sputter Deposition.....	12
3 – Experimental Techniques	15
3.1 Sputter Deposition.....	15
3.1.1 Sputter Deposition Equipment.....	15
3.1.2 Gas Impurity Monitoring.....	17
3.1.3 Substrate Temperature Control.....	18
3.2 Characterization Techniques.....	19
3.2.1 X-Ray Diffraction.....	19
3.2.2 X-Ray Reflectivity.....	21
3.2.3 X-Ray Photoelectron Spectroscopy.....	23
3.2.4 Transmission Electron Microscopy.....	25
3.2.5 Electrical Resistivity Measurement.....	31
3.2.6 Differential Scanning Calorimetry.....	33

4 – Deposition Conditions of β-W Thin Films	36
4.1 Experimental Details	36
4.1.1 Sputter Deposition of Tungsten Thin Films.....	36
4.1.2 Characterization of Tungsten Thin Films	37
4.2 Results	39
4.1.2 Film Composition Measurement.....	39
4.1.2 Relationship between β -W Formation and Deposition Conditions by XRD and Resistivity Measurement	45
4.1.3 Microstructure of β -W Thin Films by TEM	52
4.3 Discussion	56
4.3.1 Advantages of β -W Deposition with Nitrogen Impurity	56
4.3.2 Modeling the Effect of Deposition Parameters on β -W Formation.....	57
4.4 Summary	62
5 – Deposition of β-W on Other Underlayers and Substrates.....	64
5.1 Motivation	64
5.2 Experimental Details	65
5.3 Results	67
5.3.1 Relationship Between Underlayer Materials and β -W Formation.....	67
5.3.2 Deposition of β -W on Permalloy Underlayer	69
5.4 Discussion	72
5.4.1 Effect of Underlayer Crystalline Structure	72
5.4.2 Effect of Underlayer Chemistry	73
5.5 Summary	76
6 – Formation of (002) Textured Permalloy on β-W	77
6.1 Motivation	77
6.2 Experimental Details	78
6.3 Results	79
6.3.1 Formation of (002) Textured Permalloy on β -W	79
6.3.2 The Limitation of (002) Texture Formation.....	82

6.4	Discussion	84
6.4.1	Lattice Mismatch Model for (002) Texture Formation.....	84
6.4.2	Surface Energy Model for (002) Texture Formation.....	85
6.4.2	Structure Zone Model for (002) Texture Formation.....	89
6.5	Summary	92
7	– Differential Scanning Calorimetry Characterization of β-W to α-W Phase Transition	93
7.1	Experimental Details	93
7.1.1	Sputter Deposition of Thin Films	93
7.1.2	Preparation of Free-Standing β -W Flakes.....	94
7.1.3	DSC Specimen Assembly and Measurement	94
7.2	Results	96
7.3	Discussion	101
7.4	Summary	105
8	– Conclusions	106
8.1	Summary	106
8.2	Suggestions for Future Work	107
	Bibliography	109

List of Figures

Figure 2.1. The unit cell of A15 structured β -W.

Figure 2.2. Schematic diagram of spin Hall effect in thin films [Awschalom, *et al.*, 2009].

Electrically-injected electrons become spin polarized, and the electrons with green arrows indicating the direction of their spin polarization experience anisotropic spin scattering in the presence of spin-orbit coupling as a result of the spin Hall effect.

Figure 3.1. Schematic diagram of X-ray photoelectron spectroscopy [Kibel 2003].

Figure 4.1. The XPS spectrum of β -W thin films after the surface oxide was removed by argon ion beam bombardment.

Figure 4.2. The RGA spectrum of base pressure in the chamber prior to the introduction of Ar for deposition.

Figure 4.3. The shape of the XPS peaks of W, O, and N elements in the β -W thin films.

Figure 4.4. The RGA spectrum of base pressure after the deposition of β -W films.

Figure 4.5. The XRD pattern of the 112 nm-thick W film deposited at 1.2×10^{-5} torr N_2 .

Figure 4.6. The XRD pattern of the 14nm tungsten films deposited at different N_2 pressure.

Figure 4.7. The electrical conductivity of 14 nm β -W thin films. The volume fraction of β -W was calculated using equation 4.1.

Figure 4.8. The relationship between the volume fraction of β -W in the films and N_2 pressure.

The films are 14 nm thick and were deposited at 50W. The volume fraction of β -W was calculated using equation 4-1.

Figure 4.9. The XRD pattern of tungsten films deposited at fixed pressure of 1.2×10^{-5} torr N_2 and different powers of 25W, 50W, and 100W.

Figure 4.10. The relationship between the N_2 pressure and the volume fraction of β -W at different deposition power.

Figure 4.11. The dependence of β -W volume fraction on substrate temperature for films deposited at the N_2 pressure of 1.2×10^{-5} torr.

Figure 4.12. Bright-field transmission electron micrographs of 14 nm-thick W films deposited at N_2 pressures of 2.0×10^{-8} (a), 2.2×10^{-6} (b), 3.9×10^{-6} (c) and 1.2×10^{-5} torr (d). The selected area diffraction patterns are shown as insets in the lower right. Figure (e) is a high-resolution transmission electron micrograph of β -W grains with atomic resolution. The white circle in (b) is used to mark a region of β -W.

Figure 4.13. The EELS spectrum of β -W grains. No evidence of nitrogen was found in β -W grains as indicated by the absence of energy peaks at 400 eV.

Figure 4.14. The bright-field cross-section TEM image of the β -W thin films.

Figure 5.1. XRD patterns of W/Cr and W/CoFeB films on amorphous glass substrates. The W layers were deposited at 1.2×10^{-5} torr of N_2 pressure.

Figure 5.2. The dependence of β -W formation on underlayer materials. β -W phase was observed on underlayer highlighted in green, while only α -W was observed in tungsten films deposited on underlayers highlighted in orange. The elements highlighted in yellow were not studied in this work.

Figure 5.3. The XRD pattern of tungsten film on Ni underlayer. The tungsten film was deposited at 1.2×10^{-5} torr N_2 .

Figure 5.4. The XRD pattern of tungsten films deposited at 50W and 10W on permalloy underlayers with 1.2×10^{-5} torr N_2 .

Figure 5.5. The XRD pattern of Ta 5nm/Cu 5nm/permalloy 5nm/W 30nm/Cu 5nm/Ta 5nm structure used for the ferromagnetic resonance measurement.

Figure 6.1. The XRD pattern of 15nm permalloy films deposited on 14nm β -W underlayer.

Figure 6.2. The electron diffraction pattern of cross-sectional permalloy/ β -W specimen.

Figure 6.3. The dark field TEM image of (002) oriented permalloy grains.

Figure 6.4. The XRD pattern of the Ni-Fe alloy thin films deposited on β -W underlayers.

Figure 6.5. The shape of islands in fcc structured films to maximize the area of the (111) surfaces by forming (A) (111) texture and (B) (002) texture [Feng *et al.*, 1994].

Figure 6.6. The classification of deposition parameters in structure zone model [Wang *et al.*, 2014].

Figure 6.7. The schematic diagram of the process in which the fast growing grains shown as grain a envelope the slow growing ones shown as grain b [Mahieu *et al.*, 2006].

Figure 7.1. The schematic diagram for packing the β -W flakes into envelopes for DSC measurement [Berry 2007].

Figure 7.2. The XRD pattern of the β -W/SiO₂/Cu/Si structure measured with θ - 2θ scan.

Figure 7.3. The DSC curves of β -W flakes obtained at 40°C/min heating rate. The curves are displaced for clarity.

Figure 7.4. The DSC curves of β -W flakes measured at different heating rates. The curves were obtained by subtracting the curves of the second scans from those of the first scans. The curves are displaced for clarity.

Figure 7.5. The plot showing the relationship between peak temperatures and heating rates in DSC. The slope is the activation energy of the β - to α -W phase transition.

Figure 7.6. The classification of diffusionless classification [Cohen *et al.*, 1979].

List of Tables

Table 2.1. The experimental spin Hall angle of metal thin films.

Table 4.1. The composition of β -W thin films calculated from XPS spectrum.

Table 4.2. The relative intensity and peak positions of β -W and α -W XPS spectrum.

Table 4.3. The values of P_0 and n as fitting parameters of equation 4-2.

Table 5.1. Relationship between structure of the underlayers and the formation of β -W phase in tungsten thin films.

Table 6.1. Surface energy of elemental metals [Tyson *et al.*, 1977].

Table 7.1. The peak temperatures of DSC curves measured at different heating rates.

Acknowledgements

First of all, I would like to express my deepest appreciation to my PhD advisor, Professor Katayun Barmak. She not only serves as my research advisor and provided invaluable knowledge and directions to my projects at Columbia University, but she also supported me strongly in exploring a wide variety of opportunities in the industry.

Second, I would like to acknowledge my friends and advisors in industry, Bincheng Wang and Tomoko Seki at Western Digital Corporation, Isaac Lauer and Renee Mo at IBM Watson. They provide me the opportunity to experience the life in computer hardware industry and apply my knowledge to the application of products, which in turn helps me to gain a deeper understanding of my research projects at Columbia University.

Third, I would like to thank the staff at Brookhaven National Laboratory, Lihua Zhang, Kim Kisslinger, Fernando Camino, Ming Lu, Aaron Stein, Dmytro Nykypanchuk, and Peter Stevens, for their knowledge and instruction during my work at the Center for Functional Nanomaterials and National Synchrotron Light Source.

Finally, I would like to thank my wife Min Chen, and my parents Dehua Li and Shuhe Liu, for their support during my ups and downs during my PhD.

1 - Introduction

1.1 Introduction

Spintronics involves the manipulation and detection of the spin moment in solid-state systems [Žutić *et al.*, 2004], and it is regarded as a new paradigm in place of conventional charge-based electronics with the advantages of non-volatility, low power consumption and high integration density [Wolf *et al.*, 2001]. Spintronics relies on the transport properties of spin polarized current [Žutić *et al.*, 2004], which was conventionally generated by passing a charge current through a ferromagnetic contact [Johnson *et al.*, 1985]. Nowadays, the spin Hall effect is regarded as a promising mechanism for the generation of spin-polarized current without requiring the use of a magnetic field or ferromagnetic materials [Jungwirth *et al.*, 2012]. β -W, with its giant spin Hall effect, is among the materials with the highest efficiency in converting the electric current into a spin current [Pai *et al.*, 2012], hence it has been adopted as the prototypical material in the design of spintronic devices [Pai *et al.*, 2012, Hao *et al.*, 2015].

On the other hand, although β -W was discovered more than 60 years ago [Hägg *et al.*, 1954], there has been no definite conclusions about the nature of β -W and its mechanism of formation. It has been shown that the formation of β -W depends sensitively upon the deposition parameters, such as the thickness of the films [Pai *et al.*, 2012, Noyan *et al.*, 1997, Rossnagel *et al.*, 2002], the pressure of inert gas [Radić *et al.*, 2012, Vink *et al.*, 1993, Susa *et al.*, 1985, Aouadi *et al.*, 1992], and the presence of oxygen impurity [Maillé *et al.*, 2003, Shen *et al.*, 2000, Pai *et al.*, 2012, Hao *et al.*, 2015, Weerasekera *et al.*, 1994, Basavaiah *et al.*, 1968], but to the knowledge of the author, no empirical models that could quantitatively describe the relationship between the formation mechanism of β -W and the deposition parameters exists. In particular, the role of oxygen impurity is still under debate, as some researchers suggested that β -W should be a

non-stoichiometric oxide with the formula W_3O [Hägg *et al.*, 1954, Sinha, 1972], while others showed the oxygen element in β -W films to be in zero valence state, indicating that β -W should be an allotrope of α -W [Petroff *et al.*, 1973, Mannella *et al.*, 1956].

The work in this thesis introduces a novel technique of β -W deposition by magnetron sputtering. The relationship between the deposition parameters and the formation of β -W phase is to be investigated, and the corresponding empirical model will be articulated to provide insight into the mechanism of β -W formation and the role of gas impurities. The microstructure, transport properties and thermodynamics of β -W are then investigated experimentally. In addition, the use of β -W underlayer as a seed layer for the formation of (002) textured permalloy films will be demonstrated.

1.2 Organization of the Dissertation

Chapter 2, “Background and Motivation”, reviews the applications of α -W and β -W thin films in the electronics industry. As the most important feature of β -W thin films is associated with the giant spin Hall effect, the physics of the spin Hall effect is reviewed as well. Then the existing deposition techniques of β -W films by chemical vapor deposition and physical vapor deposition are reviewed, as well as their advantages and disadvantages for spintronic devices manufacturing.

Chapter 3, “Experimental Techniques”, introduces the principles of the experimental equipment involved in this thesis for thin film deposition and characterization, including the details of the magnetron sputtering deposition process, the principle of X-ray diffraction, X-ray reflectivity, X-ray photoelectron spectroscopy, transmission electron microscope and specimen preparation, electrical resistivity measurement, and differential scanning calorimetry.

Chapter 4, “Deposition Conditions of β -W Thin Films”, provides details about the relationship between the formation of the β -W phase and the deposition parameters, including nitrogen gas pressure, substrate temperature and deposition rate. Then the composition, volume fraction of β -W, electrical resistivity and microstructure are experimentally characterized. The empirical model quantifying the relationship between β -W volume fraction and deposition parameters is established, and the physical mechanism of β -W formation is inferred from the empirical model.

Chapter 5, “Deposition of β -W on Other Underlayers and Substrates”, presents the dependence of β -W phase formation on substrate/underlayer materials, and the substrate/underlayer materials are classified based upon whether the formation of β -W is possible on the corresponding layers. Then the deposition conditions are optimized to obtain β -W films on permalloy underlayers.

Chapter 6, “Formation of (002) Textured Permalloy on β -W”, shows the possibility of obtaining (002) textured permalloy deposited on β -W underlayers under suitable conditions. Then the possible mechanism for the explanation of texture formation is discussed.

Chapter 7, “Differential Scanning Calorimetry Characterization of β -W to α -W Phase Transition”, presents the measurement of the thermodynamics and kinetics of the β -W to α -W phase transition by differential scanning calorimetry. The mechanism of phase transition is then discussed based on the activation energy of the phase transition.

Chapter 8, “Conclusions”, summarizes the findings of the previous chapters, and lists recommendations for future work in this area.

2 – Background and Motivation

2.1 Tungsten Thin Films in Electronics Industry

Tungsten is one of the conductive materials most widely used in semiconductor industry [Suguro *et al.*, 1988]. Tungsten has a body-centered cubic (bcc) structure, and is also named α -W in order to distinguish it from other phases [Petch, 1944]. The most common applications of α -W include the use of tungsten plugs to provide inter-layer electric contact between adjacent metal levels separated by a dielectric layer. Tungsten is superior over aluminum for the application of vias, in a large part because tungsten films deposited by chemical vapor deposition (CVD) have a better step coverage that allows better filling of holes with high aspect ratio [Pierson, 1999]. In addition, tungsten also has the following advantages in electronics production: (i) no lithographic patterning is necessary for selective tungsten deposition, (ii) the patterning of tungsten is straightforward with dry or wet etching technology, and (iii) CVD-deposited tungsten films have strong resistance against electromigration, interdiffusion and stress-related failures [Pierson, 1999].

In the recent years, there has been a growing interest in through-silicon via (TSV) as a technique for 3D semiconductor packaging [Knickerbocker *et al.*, 2008, Koester *et al.*, 2008]. The chips are stacked on top of each other and the interconnection between these chips is established by letting the plugs pass completely through the dies. Thusly, a shorter interconnection path is created, hence the parasitic loss and time delay of signal propagation can be reduced [Sarkar, 2014]. Tungsten thin films, with their superior conformity, are considered one of the candidates as the choice of materials for TSV [Motoyoshi 2009, Selvanayagam *et al.*, 2008, Kikuchi *et al.*, 2008], and tungsten TSV has been realized in 300mm wafer production [Liu *et al.*, 2008].

In addition to its application in the electronics industry, tungsten thin films are also used as the reflection layers in multilayer X-ray mirrors [Kozhevnikov *et al.*, 1995]. The multilayer X-ray mirrors consist of alternating layers of highly reflective and highly transmissive thin films [Utsumi *et al.*, 1988], and the thickness of these layers are carefully tuned so that highly-focused X-ray beams with strong intensity can be generated by reflection and refraction [Kortright *et al.*, 1991, Thompson *et al.*, 1987]. Tungsten films are one of the most commonly-used materials as the reflective layers in X-ray mirrors with its high reflectivity, with carbon or beryllium as the transmissive layers [Suzuki 1989].

2.2 β -Tungsten Thin Films in Spintronics

2.2.1 Properties of β -Tungsten Thin Films

It is commonly found in tungsten thin films deposited at low temperatures that there exists a differently structured phase other than α -W [Petroff *et al.*, 1973, Tang *et al.*, 1984, Busta *et al.*, 1986, Paine *et al.*, 1987, Basavaiah *et al.*, 1968, Miller *et al.*, 1962]. This phase has a cubic A15 structure and is usually called β -W [Morcom *et al.*, 1974]. The unit cell of the A15 structure is shown in Figure 2.1. In addition to the difference in crystallographic structure, β -W also distinguishes itself from α -W with its higher electrical resistivity of about 5 to 10 times that of α -W at room temperature [Petroff *et al.*, 1973], and higher superconducting transition temperature at about 3K [Basavaiah *et al.*, 1968].

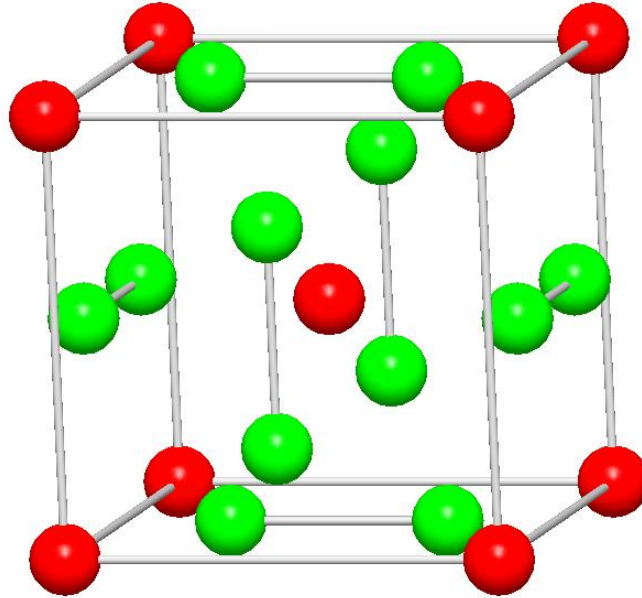


Figure 2.1. The unit cell of A15 structured β -W.

Due to its higher resistivity, the formation of β -W is usually considered undesirable, especially in the application of vias and TSV where the propagation delay becomes worse as the resistivity along the interconnection increases [Antinone *et al.*, 1983]. Therefore, the β -W phase needs to be converted into α -W phase by annealing at high temperatures. On the other hand, the interest in the application of β -W in spintronics has been sparked in the recent years as a result of the discovery of the giant spin Hall effect in β -W thin films [Pai *et al.*, 2012].

2.2.2 Spin Hall Effect in β -Tungsten Thin Films

Spin Hall effect (SHE) refers to a family of spin-dependent transport phenomena caused by spin-orbit coupling in materials. Due to the interaction between the spin and orbital

momentum in itinerant electrons, the spin polarization of the conduction electrons is no longer independent of its translational and orbital momentum [Dresselhaus 1955, Rashba 1960].

Instead, the electrons with opposite spins traverse the thin films along different directions. The schematic diagram of spin Hall effect is shown in Figure 2.2. As a result of the spin Hall effect, when an electric current flows through the film, a net spin current is generated without the adoption of ferromagnetic materials or magnetic field [Hirsch 1999, Zhang 2000, Dyakonov *et al.*, 1971]. Therefore, the spin Hall effect is promising as the source of spin-polarized current that can be simply manipulated by an electric field [Jungwirth *et al.*, 2012].

If there is no sink for the net spin polarization in the thin films, the spin momentum accumulates at the boundaries and creates imbalance on the opposite edges of the films [Takahashi *et al.*, 2008]. Therefore, the spin Hall effect can also be observed by the measurement of spin accumulated on the boundaries using spatially resolved techniques such as as Kerr microscopy [Kato *et al.*, 2004].

The spin-orbit couplings responsible for the spin Hall effect can have two possible sources: In the first case, the electrons with opposite spin polarization are skew scattered into different directions by spin-orbit coupled Mott scattering from the impurities. As this mechanism does not occur in ideally pure materials, it is regarded extrinsic [D'yakonov *et al.*, 1971, Hirsch 1999]. In the second case, the material itself has a spin-orbit coupled energy band structure, and this band structure gives rise to the spin-dependent electron trajectories in the film [Murakami *et al.*, 2003, Sinova *et al.*, 2004]. This mechanism is regarded intrinsic, as it does not require the existence of impurities as scattering centers.

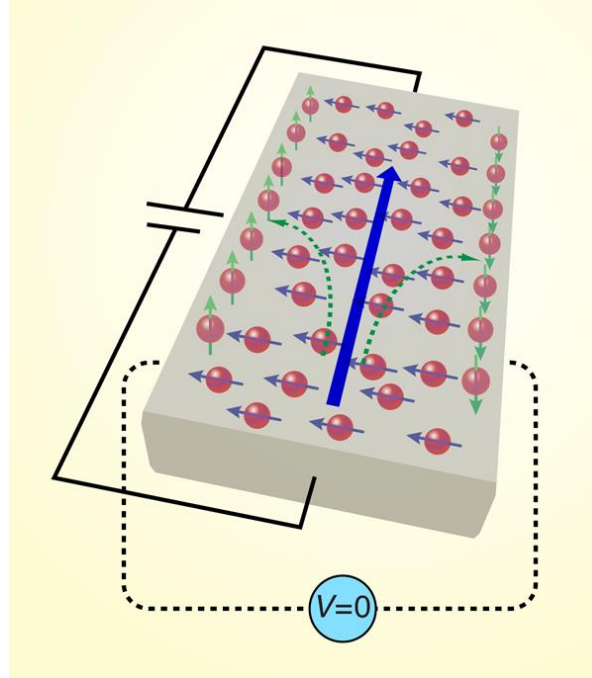


Figure 2.2. Schematic diagram of spin Hall effect in thin films [Awschalom, *et al.*, 2009].

Electrically-injected electrons become spin polarized, and the electrons with green arrows indicating the direction of their spin polarization experience anisotropic spin scattering in the presence of spin-orbit coupling as a result of the spin Hall effect.

The transverse spin current can be described by equation 2-1 as

$$J_s = \theta_{SH} (\sigma \times J_e) \quad (2-1)$$

where θ_{SH} is the spin Hall angle which is a characteristic parameter of materials, σ is the spin polarization unit vector, J_e is the electric current density, and $\hbar J_s / 2e$ is the spin current density [Pai *et al.*, 2012]. The efficiency of electric-to-spin current conversion can be characterized by the magnitude of spin Hall angle as in equation 2-2:

$$|\theta_{SH}| = |J_s / J_e| \quad (2-2)$$

The spin Hall angle can be calculated by measuring the magnitude of spin current caused by applying an electric current across the specimen. However, in practice, the measurement of spin current is very difficult. On the other hand, a spin current can also create an electric current with efficiency determined by the same spin Hall angle [Hirsch 1999], the latter of which can be easily measured with high accuracy. The phenomenon of electric current generation from the spin current is called the inverse spin Hall effect (I-SHE) [Hirsch 1999]. I-SHE has been observed in both semiconductors [Bakun *et al.*, 1984] and metals [Valenzuela *et al.*, 2006, Kimura *et al.*, 2007, Saitoh *et al.*, 2006]. The spin current can be injected from an electric current that has passed through a ferromagnetic contact, but the charge current generated by ISHE is difficult to extract as its magnitude is much smaller compared with that of the initial current. Therefore, a pure spin current, in which electrons with opposite spin polarization travel in opposite directions with the same magnitude, is favored for the measurement of inverse spin Hall effect. This pure spin current can be experimentally created by spin pumping, where the spin current is injected into the spin Hall layer from a ferromagnetic layer whose momentum is precessing as a result of external magnetic field. Then the spin Hall angle can be determined accurately from the magnitude of the corresponding electric current [Tserkovnyak *et al.*, 2002, Sandweg *et al.*, 2011].

In order to achieve spintronic devices with low power consumption, it is critical to identify materials with large spin Hall angle, so that the conversion from the charge to the spin current is power-efficient. The spin Hall angles of common metals are listed in Table 2.1 [Sinova *et al.*, 2015]. The table shows that β -W has the largest spin Hall angle among all metals under investigation. Table 2.1 also shows that the spin Hall angle of α -W is much smaller than that of

β -W, hence pure β -W thin films are desired for spintronics applications. In practice, the tungsten films are usually a mixture of both phases, and the deposition parameters of β -W need to be investigated and optimized.

Table 2.1. The experimental spin Hall angle of metal thin films.

Materials	Spin Hall Angle (%)	Reference
Al	0.032	Valenzuela <i>et al.</i> , 2006
Au	1.6	Hung <i>et al.</i> , 2013
Ag	0.7	Wang <i>et al.</i> , 2014
Cu	0.32	Wang <i>et al.</i> , 2014
Mo	-0.05	Mosendz <i>et al.</i> , 2010
Pt	5.6	Rojas-Sánchez <i>et al.</i> , 2014
Ta	-12	Liu <i>et al.</i> , 2012
α -W	-14	Wang <i>et al.</i> , 2014
β -W	-33	Pai <i>et al.</i> , 2012

2.3 Deposition of Tungsten Thin Films

2.3.1 Chemical Vapor Deposition

α -W thin films can be deposited by CVD and sputtering. CVD is the most commonly-used technique for W due to its ability to produce films with conformal step coverage, which makes it advantageous for the application of vias in integrated circuits. The CVD process takes place in semiconductor manufacturing by the reaction of equation 2-3:



The above reaction usually occurs at the temperature range between 300°C and 700°C, and the pressure of the precursors ranges from 10 torr to 1 atmosphere [Pierson, 1999].

The other reaction for W deposition in the CVD process involves the fluoridation of silicon substrates in equation 2-4 as



This reaction usually occurs at the temperature range of 310°C to 540°C and the pressure of the precursors ranges from 1 to 20 torr [Pierson, 1999]. This reaction proceeds at a much higher rate than the hydrogen reduction of WF_6 in equation 2-3 [Pierson, 1999], and it is self-limiting since the thickness of tungsten films is limited by the diffusion rate of WF_6 across the W films before reaching the silicon substrate.

Other precursors in addition to WF_6 can be used for CVD deposition of tungsten films, and the reactions take place as in equation 2-5 and 2-6 [Pierson, 1999]:



For the above deposition processes, the temperatures are around 600°C [Pierson, 1999].

As the deposition temperature of conventional CVD process is usually as high as 600°C, around which the kinetics of β -W to α -W phase transition is very rapid, the β -W phase is not detected in the CVD tungsten films. On the other hand, β -W phase has been identified in films obtained by CVD techniques that allow low temperature deposition. Low-pressure CVD (LPCVD) is a technique commonly-adopted to improve film uniformity and reduce unwanted gas-phase reaction [Cooke, 1985]. The LPCVD process takes place through the combined

process of equation 2-3 and equation 2-4 at a reduced gas pressure in the range of 0.1 Torr and decreased temperature of 300°C [Paine *et al.*, 1987]. At this reduced temperature, the β -W phase has long enough lifetime to survive the entire deposition process [Paine *et al.*, 1987].

Plasma-enhanced CVD (PECVD) technique takes advantage of the high-energy precursors generated as a result of plasma created by an RF field in the chamber, and the high-energy precursors are more likely to obtain enough thermal energy to overcome the reaction barrier than in the absence of a plasma. Therefore, PECVD can proceed at lower temperatures [Droes *et al.*, 1997]. β -W phase was identified in films deposited by PECVD by the reduction of WF_6 with H_2 [Tang *et al.*, 1984]. While the mixture of α - and β -W were identified in PECVD tungsten films deposited at the electrode temperature of 350°C, no α -W phase was observed in those deposited at 250°C or below [Tang *et al.*, 1984].

β -W phase has also been found as the product of reduction of WO_3 with hydrogen at about 500°C [Davazoglou *et al.*, 1997, Davazoglou *et al.*, 1997, Morcom *et al.*, 1974, Murugan *et al.*, 2011], as well as other non-stoichiometric tungsten oxide with the formula of WO_x . The observation of β -W along with other oxides, and the structural similarity between WO_3 and A15 structured compounds, lead to the belief that β -W is essentially a special form of off-stoichiometric tungsten oxide [Hägg *et al.*, 1954].

2.3.2 Sputter Deposition

The family of CVD techniques involves complicated gas transport and chemical reaction processes, as well as other factors that can affect the reaction kinetics including the change of precursor energy in the presence of plasma, the geometry of the reactor, and the reaction of

precursors with the substrate. Therefore, CVD deposition is not suitable for the study of the formation process of β -W phase in thin films. In comparison, sputter deposition is much less complex than CVD. The result of sputter deposition can also be generalized to other deposition instruments with different configurations, while the results of CVD are greatly influenced by the design of the reactor. Most importantly, the deposition parameters of sputtering are independent and can be externally manipulated, allowing the investigation of the influence of each parameter individually.

The influence of deposition parameters, including film thickness, inert gas pressure, substrate bias, substrate temperature and impurity gas pressure, on the formation of β -W phase have been investigated extensively [Petroff *et al.*, 1973, Maille *et al.*, 2003, Karabacak *et al.*, 2003, Radić *et al.*, 2012, Haghiri-Gosnet *et al.*, 1989, Durand *et al.*, 1996, Weeraseker *et al.*, 1994, Djerdj *et al.*, 2005, Rossnagel *et al.*, 2002, Noyan *et al.*, 1997]. At the initial stage of deposition with film thickness smaller than 10 nm, β -W phase was always found in the films. Then the films of a mixture of β -W and α -W phase were usually identified below 45nm. At large thickness (> 100 nm), α -W became the main phase in the films [Pai *et al.*, 2012, Noyan *et al.*, 1997, Rossnagel *et al.*, 2002]. Some studies also showed β -W phase was observable even at thickness of about 600nm [Noyan *et al.*, 1997], hence there has been no consensus on the critical thickness of β -W films.

The formation of β -W is particularly affected by the presence of oxygen impurity in the deposition chamber [Maille *et al.*, 2003, Shen *et al.*, 2000, Pai *et al.*, 2012, Hao *et al.*, 2015, Weeraseker *et al.*, 1994, Basavaiah *et al.*, 1968]. The oxygen impurity could be introduced from a pipeline connected to the chamber [Shen *et al.*, 2000], generated from the sputtering process of oxide targets [Maille *et al.*, 2003, Witham *et al.*, 1993], or produced by the segmentation of

water vapor in the chamber [Pai *et al.*, 2012, Weeraseker *et al.*, 1994, Basavaiah *et al.*, 1968, Arita *et al.*, 1993]. The presence of oxygen impurity stabilized the β -W phase against the α -W, and the β -W films also contained a high amount of oxygen contamination [Shen *et al.*, 2000].

The substrate bias could be used for selective deposition of α -W phase or β -W phase [Petroff *et al.*, 1973]. When the substrate was at zero bias or was positively biased, the β -W films always formed before reaching the critical thickness. On the other hand, films deposited on negatively-biased substrates only contained α -W [Petroff *et al.*, 1973]. As the amount of oxygen impurity, which was regarded as indispensable for the formation of β -W, in the films decreased at negative substrate bias, the formation of α -W vs β -W was regarded as the result of the change of reactivity of tungsten atoms by the variation of kinetic energy [Petroff *et al.*, 1973].

In addition, the formation of β -W was preferential at high inert gas pressure. At the argon pressure of 21 mTorr, β -W was the main phase of the films, while only α -W was detected in films deposited at 5 mTorr or lower [Radić *et al.*, 2012]. Qualitatively similar results were found by other researchers [Vink *et al.*, 1993, Susa *et al.*, 1985, Aouadi *et al.*, 1992]. The relationship between argon partial pressure and β -W formation can be attributed to the collision between argon and tungsten atoms, as a result of which the tungsten atoms might not have sufficient energy to be incorporated into the stable α -W grains after landing on the surface [Vink *et al.*, 1993]. This explanation has also been applied to the observation that the formation of β -W was favored at smaller deposition power ($<6\text{W cm}^{-2}$) [Collot *et al.*, 1988, Djerdj *et al.*, 2005] and negative bias [Petroff *et al.*, 1973, Hugon *et al.*, 1989].

3 – Experimental Techniques

3.1 Sputter Deposition

3.1.1 Sputter Deposition Equipment

Sputter deposition makes use of the bombardment of energetic ions to deposit thin films from solid targets. The vacuum of the chamber is maintained at better than 10^{-7} torr, as thin films are extremely prone to gas impurity contamination. The sputtering targets with the same composition of the films are connected to the negative terminal of a DC power supply as cathode. The deposition process takes place by introducing inert gas at the pressure range of 10^{-3} torr and applying a high voltage of hundreds of volts between the targets and the anode. The electric field creates a discharge region near the target consisting of positive inert gas ions such as Ar^+ , which are attracted to the sputtering target with negative potential. In that process, the surface of the targets are bombarded and the target atoms acquire enough energy to be released from the surface and travel to the substrates. Then the target atoms are adsorbed and condensate into continuous films until a certain thickness is reached.

Sputter deposition is favored for tungsten thin films over other types of physical vapor deposition techniques, including evaporation and electron-beam deposition. Both thermal evaporation and electron-beam deposition involve using evaporating the source materials into low-pressure vapor which then condenses onto the substrate into thin films. Tungsten has an extremely high melting point at 3422°C , so it is difficult to vaporize tungsten source or to find a suitable container stable at the corresponding temperatures. On the other hand, sputter deposition does not require the thermal evaporation of the source materials, as the energy of source atoms originates from the transfer of momentum from the

energetic ions in the plasma. Sputter deposition also has the advantages over CVD that no special recipes are needed for each individual metal. As magnetic random-access memory (MRAM) is composed of multiple layers of metal thin films, sputter deposition of β -W as the spin-current source of MRAM can be more easily integrated into the manufacturing process than CVD.

For non-conductive materials, DC sputtering is not sustainable, as the charges of inert gas ions accumulate on the surface of the non-conductive targets over time and create a potential that prevents further bombardment of ions onto the targets. Therefore, the deposition of nonconductive materials is realized with radio-frequency (RF) sputtering usually at 13.56 MHz. In that process, the impedance of insulators drops to finite values and allow the current to pass through at high frequency, therefore the charges on the surface of the target are neutralized by the AC current.

The DC and RF sputtering techniques suffer from the disadvantage of low deposition rate, as the ions have a low density and a short life-time by neutralization. Magnetron sputtering overcomes this short-coming by creating a confining magnetic field with a permanent magnet attached onto the back of the targets. The magnetic field, together with the electric field created by the power supply, confines the motion of electrons along to the direction of $E \times H$, where E is the electric field and H is the magnetic field, and these electrons collide with the Ar atoms and generate Ar ions. In this way, the ions are restricted to the surface of the targets, which greatly increases the frequency of impingement between the ions and surface atoms of the targets. As a result, higher deposition rate can be achieved. Magnetron sputtering also has the additional benefit that the critical inert gas pressure

required to ignite the plasma is lower, thereby the amount of gas contamination in the films can be reduced.

3.1.2 Gas Impurity Monitoring

The vacuum environment is very important for sputter deposition, and the control of the pressure of reactive gas impurities, such as nitrogen, water vapor and oxygen, is especially important in optimizing the properties of the deposited thin films. In particular, the formation of β -W is extremely sensitive to the pressure of oxygen impurity in the chamber even at pressures as low as 10^{-6} torr [Hao *et al.*, 2015], hence monitoring the oxygen partial pressure is essential in order to understand its effect on the formation of β -W in thin films.

The pressure of all species of gas in the deposition chamber is monitored by a Stanford residual gas analyzer (RGA). The RGA is essentially a mass spectrometer analyzing the composition of the gas sampled from the main chamber. These gas molecules are ionized by the energetic electrons emitted from the filament in the RGA. Some of the gas molecules undergo fragmentation from interaction with electrons, so there could be multiple species of fragments corresponding to a single species of gas. The ions are filtered using a quadrupole filter which only allows the fragments with a particular charge-to-mass ratio to pass and rejects other fragments by neutralization on the poles. The fragments across the filter with definite mass-to-charge ratio are then collected and counted by Faraday cup or electron multiplier detectors, and the partial pressure of the corresponding gas in the main chamber is calculated proportionally.

The Stanford RGA is only able to work below 10^{-4} torr, therefore it cannot be used for in-situ monitoring during the deposition, which requires a flow of inert gas at the pressure range of 10^{-3} torr. Instead, the RGA spectra are obtained before and after the deposition process at the pressure range of 10^{-5} to 10^{-8} torr without argon in the chamber.

3.1.3 Substrate Temperature Control

The substrate can be heated to high temperatures during the deposition process, and the substrate temperature is an important factor in the stability of β -W phase. Due to the sequential arrival of atoms during the deposition, each atom can diffuse with high surface mobility for a short period until it is buried by the subsequent layers. Henceforth, surface diffusivity can dominate over grain boundary and lattice diffusivity in thin films deposited at high temperatures, and its value can be orders of magnitude higher. The high mobility of surface atoms as a result of substrate heating allows the modification of film properties requiring the migration of atoms, including segregation, surface roughening or smoothening, intermixing across the interfaces, thin film epitaxy, and phase transition. Therefore, it is critical to control the substrate temperature for the optimization of film properties.

The deposition of β -W can be adversely affected at high substrate temperatures, as the β to α -W phase transition can proceed rapidly due to the high surface diffusivity. On the other hand, the relationship between substrate temperature and β -W formation can provide insight into the formation mechanism of β -W phase. Therefore, deposition of β -W films at elevated temperatures is conducted even though the formation of β -W is unfavorable under such conditions.

The heating elements in the deposition system used for this thesis consists of a radiative filament and a thermocouple. The radiative filament itself is first heated to high temperature by Joule heating, and the thermal radiation from the filament is absorbed by the substrate. The temperature is monitored by the thermocouple near the back of the substrate, and tuned by a PID controller. The difference between the temperature read at the back and the front surface of the substrates is calibrated using a calibration wafer with multiple thermocouples attached to its front surface, and a calibration chart is compiled by recording the temperatures at the two sides of the substrates at different set temperatures.

3.2 Characterization Techniques

3.2.1 X-Ray Diffraction

X-ray diffraction (XRD) is a measurement technique widely-used to study the crystallography of solid materials. The presence of phases in a mixture can be identified from the appearance of their diffraction peaks in the XRD patterns, and their corresponding volume fractions can be quantified from the integrated intensity of the peaks. In thin films, the crystallites often develop a preferred orientation, which can be studied by XRD techniques such as rocking curve, pole figures, and reciprocal space mapping with a proper selection of X-ray optics and diffraction geometry. In addition, the strain, stress and the average size of coherently diffracting regions (often assumed to be grains) of the films can also be investigated by the change of positions and shapes of the diffraction peaks in XRD patterns.

The PANalytical diffractometer used in this thesis makes use of a Bragg-Brentano geometry. The source and detector of the diffractometer are maintained on a parafocusing circle centered at the specimen. The divergent X-ray beam emitted from the source incidents upon the

surface of the sample, and the diffracted beams are automatically refocused at the detector slit due to the parafocus geometry. Narrow slits are used at the source and the detector in order to restrict the divergence angle of the X-ray beam as well. The Bragg-Brentano geometry provides a good combination of intensity and peak shape. Due to the lack of a precise collimation procedure of the X-ray beams, the angular resolution of diffractometer with this geometry is not very high, but it is enough for most applications such as phase identification.

The peaks in the diffraction pattern are generated due to the interference between X-ray beams reflected on parallel crystal planes, and the position of the peaks follow Bragg's law as given in equation 3-1

$$2d_{hkl} \sin \theta = \lambda \quad (3-1)$$

where d_{hkl} is the spacing between parallel planes indexed by their Miller index (hkl), 2θ is the diffraction angle, λ is the X-ray wavelength. Therefore, the presence of a phase can be determined from the observed planar spacing in the diffraction pattern.

The out-of-plane texture can be determined from the θ - 2θ scanning geometry. During the measurement, the source and detector move with the same angular speed in opposite directions, so that the angle between the surface and the incident beam is kept the same as that between the surface and the diffracted beam. The scattering vector of the specimen detected by the XRD is determined by the incident and outgoing X-ray wave-vector as in equation 3-2

$$k = k_{out} - k_{in} \quad (3-2)$$

where k_{out} is the diffracted beam, k_{in} is the incident beam, and k is the reciprocal vector of the specimen. Hence the reciprocal vector measured by the θ - 2θ scan is always perpendicular to the surface of the specimen.

In addition to phase identification, the grain size can also be measured by XRD using the Scherrer formula in equation 3-3 as

$$\tau = \frac{K\lambda}{\beta \cos \theta} \quad (3-3)$$

where τ is the grain size, λ is the X-ray wavelength, β is the full-width half maximum of the diffraction peak in radians, and θ is the peak angle. The grain size measured by equation 3-3 is along the direction of the reciprocal vector k in the specimen calculated from equation 3-2.

Although the grain size is isotropic for most bulk and powder materials, it is usually anisotropic in thin films which often develop a columnar grain structure. Therefore, grain size determined using equation 3-3 in θ - 2θ scan is orientated perpendicular to the surface of the films and is often equal to the film thicknesses. In the cases where the in-plane grain size measurement is needed, grazing-incidence XRD can be performed in which the incident and outgoing vector is almost parallel to the surface henceforth the reciprocal vector is in-plane.

3.2.2 X-Ray Reflectivity

The X-ray diffractometer can also be used for X-ray reflectivity (XRR) measurement for film thickness determination. XRR is a non-destructive and non-contact technique applicable to films with thicknesses in the range of 2 to 200 nm at the precision of about 1-3 Å. Through more detailed analysis of experimental data, other useful metrics of thin films can be inferred,

including the density and roughness of single-layer films, and the intermixing and roughness at the interfaces in multilayer thin films.

Due to the difference in the electron density between adjacent layers, the X-ray beams are reflected at the interfaces, and the interference between the reflected X-ray beams creates intensity modulation which is then recorded by the XRR detector. For a monochromatic X-ray beam of wavelength λ incident upon the surface of a specimen at a grazing angle θ , the intensity of the reflected beam is recorded at the same angle in a θ - 2θ scan, because of the specular nature of the reflection on the smooth surface. Since the refractive index of X-ray in the film is smaller than that of the air, below a critical angle θ_c total external reflection occurs, and the critical angle is useful in estimating the density of the film. Above θ_c , the reflection from different interfaces interfere with each other, giving rise to the oscillation of the intensity recorded by the detector. The period of the interference fringes is inversely proportional to the periodicity of the films, thereby the thickness of the films can be extracted from the pattern of the fringes by finding the peak of the Fourier spectrum in reciprocal space. The roughness of the layer can either be estimated from how fast the oscillation decays at higher incident angle, or quantitatively calculated by fitting the curve using Fresnel optics. In practice, simulation software is used to calculate all parameters, including thickness, composition, and interface roughness as fitting parameters in the simulation.

Since the film thickness is much larger compared with the wavelength of X-ray, the interference fringes are located at grazing angles below 10° . The need to measure the XRR curve at such small angles requires the use of a diffractometer with ultra-high angular resolution, and the use of receiver and source slits is not enough to achieve enough angular resolution. Therefore, Rigaku Ultima III diffractometer at Brookhaven National Laboratory with parallel-beam

geometry was used for the XRR measurements. The diffractometer makes use of a Gobel mirror consisting of carefully-tuned multilayer crystals to convert the divergent X-ray beam into a parallel beam. The diffracted beam is analyzed by Soller slits containing a family of parallel slits. The slits have small spacing compared with their length, hence each slit works as a narrow receiver slit to limit the divergence angle of the X-ray beams.

3.2.3 X-Ray Photoelectron Spectroscopy

X-ray photoelectron spectroscopy (XPS), also known as electron spectroscopy for chemical analysis (ESCA), is a technique for the measurement of chemical composition near the surface of materials. The schematic diagram of the physical process during the measurement is shown in Figure 3.1 [Kibel, 2003]. A monochromatic X-ray beam with known photon energy $h\nu$ is generated from the bombardment of electrons onto Al or Mg target. When the X-ray photons with high enough energy are absorbed by the specimen, a core electron is excited into the vacuum energy level and released from the specimen. The corresponding binding energy of the core electrons as $-E_{bind}$ is an indication of the species of the atoms and their valence states. Since the energy levels of the core electrons are discrete, the kinetic energy of electrons detected by the analyzer is peaked at the position according to equation 3-4 as:

$$E_{kinetic} = h\nu - E_{bind} - \phi \quad (3-4)$$

where $E_{kinetic}$ is the kinetic energy of electrons analyzed by the detector, $h\nu$ is the energy of the X-ray photons, E_{bind} is the binding energy of electrons in the solid, ϕ is determined by the work function of the analyzer and the sample and is usually regarded as a constant at the scale of

several eV. In that way, the binding energy of the core electrons can be inferred from the position of peaks in the XPS spectrum, which in turn gives information on the elements present in the films. The position of XPS peaks is also influenced by the valence state of the atoms, since the change of electronic configuration of atoms gives rise to the shift of peak positions. The concentration of the elements can also be measured by XPS from the integrated intensity of the peaks, which is proportional to the concentration of the corresponding elements.

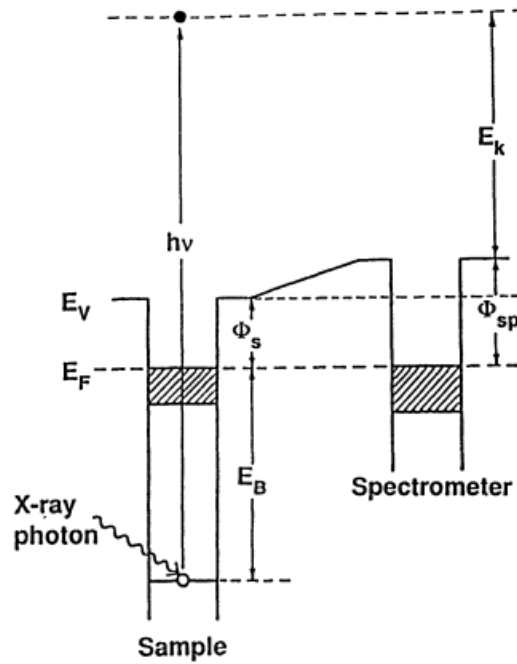


Figure 3.1. Schematic diagram of X-ray photoelectron spectroscopy [Kibel 2003].

The surface sensitivity of the XPS originates from the extremely small mean-free path of the electrons in the sample. The range of energy spectrum of XPS is between 100eV and

1200eV, and electrons have a mean free path of 0.5-2.0nm in this energy range. In addition, the escape depth decreases even further when the electron velocity becomes more parallel to the surface. The above factors make XPS an extremely surface sensitive measurement technique. For many metal materials such as Al and W, a thin oxide layer at the thickness of about 2 to 10 nm forms on the surface when the film is exposed to air, and this surface oxide layer prevents the XPS measurement of the layers underneath. Therefore, the removal of oxide under ultra-high vacuum environment is necessary prior to the XPS measurement. High energy argon ion beams are commonly used to sputter away the surface layers allowing for the measurement of the films underneath.

3.2.4 Transmission Electron Microscopy

Transmission electron microscopy (TEM) can be used to study the local crystallographic structure, morphology, and electronic structure of materials at extremely high resolution. In the TEM column, a beam of high energy electrons is generated from a source such as tungsten filament, LaB₆ source or field emission gun, and the electrons are collimated and focused by the magnetic lens. When the electrons travel through the specimen, they are scattered as a result of the strong electron-matter interaction. As a result, the transmitted electron beams have a spatial distribution of intensity associated with the microstructure of the specimen. The spatial distribution of intensity of electron beams is then magnified and recorded by the a fluorescent screen or a charge-coupled detector. High resolution images can be produced with the TEM because the de Broglie wavelength of high energy electron at keV is much smaller than the optical wavelength. The TEM images are useful for examining the microstructure of crystalline metal thin films, which usually have grain sizes smaller than 100 nm, making their

microstructure not amenable to other microscopy techniques such as optical microscopy or scanning electron microscopy.

Due to the wave nature of highly collimated electron beams, they can be diffracted from the gratings formed by the lattice planes in the crystalline specimen, and the crystallography of the specimen such as lattice constant and grain orientations can be deduced from the electron diffraction patterns. The electron diffraction pattern is different from that obtained from θ - 2θ scan of XRD, because the electron diffraction only captures the reciprocal vectors perpendicular to the beam and hence parallel to the surface for plan view specimen, while the θ - 2θ scan in XRD only detects the reciprocal vectors perpendicular to the surface of the specimen. In inhomogeneous specimen, TEM can study the distribution of phases in a mixture, by combining the microstructure imaging and electron diffraction techniques, and the use of selected-area diffraction aperture allows the extra freedom of the choice area of interest though limited by the aberration.

The imaging mode of TEM can be enhanced by selecting a subset of the electron beams. The transmitted electron beams consist of a direct beam at the center and a number of diffracted beams with their positions determined by the crystallography of the specimen. An objective aperture can be inserted to only allow selected beams to pass through. The bright field image mode is applied when the direct beam is selected, and it has the advantage that the contrast at the grain boundaries is enhanced, which allows the microstructure to be observed in weakly contrast specimens with weak contrast. On the other hand, if a subset of diffracted beams are selected, then the TEM is operating in the dark field image mode. In that case, only grains with orientation and structure that can give rise to the selected diffracted beams will show up as bright in the

image, hence the distribution of phases or grain orientations can be investigated by dark field imaging.

In both bright and dark field image mode, only the intensity of the electron wave is recorded by the fluorescent screen or charge-coupled detectors. On the other hand, the phase of the wave is indispensable in reconstructing the image at atomic resolution. In order to reconstruct the phase of the electron beams, the TEM needs to operate at high-resolution TEM (HRTEM) mode. In this mode, an objective aperture is not used, hence both the direct and diffracted beams are retained. During the propagation of these waves through the objective lens, interference between these beams takes place, which determines the distribution of intensity at the imaging plane. In this way, the relative phases of different beams are converted into the total intensity, and microstructure images with atomic resolution can then be reconstructed with the phase information. HRTEM is extensively used to analyze the crystalline structure of specimens. It also has the capability to characterize point defects, stacking faults and dislocations defects.

In addition to the microstructure and crystallography, the chemistry of the specimen such as elemental distribution and valence, can be studied using electron energy loss spectroscopy (EELS) in analytical TEM. As the electron beams travel through the specimen, some electrons lose kinetic energy to the atoms in the specimen through inelastic scattering, and the amount of energy loss measured by a spectrometer indicates the species of atoms the electrons collide with. By scanning the electron beam as a probe around the specimen, the distribution of elements can be deduced from EELS. Other details about the electronic configuration and elemental excitations in the specimen can also be inferred from the EELS spectrum, by making assumptions about the mechanism responsible for electron energy loss.

Although the TEM is a powerful tool with the capability to provide a lot of information about the specimen at high spatial resolution, the sample preparation process is extremely time-consuming. Since it is necessary that the electron beams transmit through the specimen, and the electron-matter interaction with the specimen is very strong, the specimen has to be electron transparent, which places the requirement that its thickness should be less than about 100nm. Therefore, the TEM samples have to be thinned prior to observation. The thinning procedure usually starts with a rough but efficient mechanical preprocessing. A 3mm diameter disk which is the standard size for TEM holders is carved out of the specimen using ultrasonic disk cutter. The head of the ultrasonic disk cutter is a hollow circle with a diameter slightly larger than 3mm, and it is oscillating at the frequency of kHz with small amplitude. A lubricant of silicon carbide powder is applied between the head and the specimen, which also serves as abrasive. As the powder oscillates together with the head, the friction between the powder and the specimen makes way for the head to penetrate through, leaving 3m diameter disks at their original positions.

The disks are then mounted onto the tripod polisher using a mounting wax for a rough mechanical thinning. The tripod polisher has three adjustable micrometers that allows heights on each edge individually tuned to maintain a horizontal orientation. The substrate of the disk is then mechanically thinned on a rotary polisher with lapping films attached to the wheels rotating at about 10 to 20 rpm. The lapping films contain diamonds of different grits which serve as the abrasive responsible for the mechanical thinning procedure, and the grits of the lapping films are chosen to achieve the proper balance between the efficiency of thinning with large grits and the low level of mechanical damage with small grits. The disks are thinned to about 100 μm , then polished using cloth and alumina dispersion.

After the initial thinning, the dimpler, a more delicate polishing equipment, is used to make a dimple at the center of the disk, so that the center is thin enough for electron beams to pass through, while the edges are still robust to provide mechanical support during the handling of the specimen. The dimpler works by using a rotary polishing wheel attached to an arm with counter balancing weight at the other end, and the weight can be adjusted so that only a gentle force is applied to the center of the disk. Diamond paste and suspension are used as both the abrasive and lubricant of the polishing process, and the grits of the diamonds are selected so that the surface damage from scratching is minimized. The thickness of the disk is monitored either in-situ by a micrometer or ex-situ by a measuring optical microscope. In particular, the thickness of specimen with thin metal films and silicon substrates can be inferred from the observation of back-transmitted light. With a white light source at the back of the specimen, red transmitted light indicates the thickness at the center to be about 10 μ m, and the yellow transmitted light indicates the thickness of about 5 μ m. At the end, alumina suspension is used to remove all the mechanical damage on the surface, which can then be checked by the dark field optical microscope.

Ion milling is used as the final step to thin the sample down to electron transparency. The ion milling systems usually contain two ion guns as the source of energetic Ar ion beams. These guns are positioned at grazing angle of about 7 to 10 degrees with respect to the specimen surface. The Ar ion beams are generated by high voltage at about 50kV and impingements towards the sample surface from nearly parallel directions with the current of about 40mA. The incident ion beams mills away material from the surface and thins the specimen to tens of nanometers.

The ion milling should be conducted so that the specimen is thinned to electron transparency without destroying the integrated structure of the disk. Therefore, it is critical to stop the milling process immediately when the thickness of the thinnest area is small enough for TEM observation. An optical microscope is used for in-situ monitoring of the morphology of the thinnest areas through a transparent window. When the thickness of the center is close to the optical wavelength, the interference between incident and reflected lights consisting of different wavelengths results in the creation of colorful concentric rings. Then the voltage and current of the ion beams are reduced to prevent destroying the thinnest part of the specimen. The milling continues until a small hole appears at the center of the rings and the ion milling is stopped immediately. The area around the hole has a thickness of about tens of nanometers, which makes it suitable for TEM examination.

The above techniques are useful for the preparation of plan-view TEM samples. In many cases, cross-sectional images are desirable in order to observe the structure of the interfaces in multilayer films. Focused ion beam (FIB) is the most convenient technique for preparing cross-sectional TEM samples. It is generally conducted in a scanning electron microscope equipped with focused ion guns, hence the thinning process can be in-situ monitored by electron beam imaging, and the ability of in-situ monitoring is especially useful for inhomogeneous specimen with specific area of interest.

The principle of FIB involves using a focused ion beam to mill away the atoms at the designated positions. The species of the ions is usually gallium, because gallium has very low fusion point, excellent mechanical and thermal properties, and the energy peaks of gallium do not overlap with those of most other materials hence will not interfere with the chemical analysis by analytical TEM [Ayache *et al.*, 2010]. Prior to the deposition, a layer of metal or carbon is

deposited on top of the area of interest, in order to protect the area from getting milled or damaged by the ion beam. Then the gallium ion beam is generated from a gallium reservoir in contact with a tungsten emission tip. The liquid gallium that flows through the tungsten tip is accelerated by an electric field and the resulting ions incident upon the sample surface, milling away the area it impinges with. A bridge is carved out of the sample and thinned by repeatedly milling on both sides of the bridge. At the later stage, the mechanical damage from the ion beams is removed by reducing the voltage and current of the beam. After the sample is thin enough for TEM observation, a sharp tip is positioned next to the bridge, and a layer of platinum is deposited between the tip and the bridge to attach the specimen to the tip. Then the TEM specimen is lifted off the matrix and attached onto TEM sample holder with the same technique.

3.2.5 Electrical Resistivity Measurement

The van der Pauw measurement is a convenient tool in measuring the resistivity of thin films, it is widely used in semiconductor manufacturing industry [Miccoli *et al.*, 2015] for determining the acceptance requirement of silicon and gallium arsenide wafers [Bullis *et al.*, 1970]. It can also be used to characterize the resistivity of metallization as interconnect on integrated circuits and measure the concentration of dopant in semiconductor wafers due to the reduction of resistivity in the presence of dopants [Bullis *et al.*, 1970].

The technique consists of four spring loaded sharp point probes typically made from gold or tungsten carbide. Two of the probes are the current probes and the other two are the voltage probes. A low current in the order of 100 mA is generated by a low output impedance current source, and traverses the thin film from one current probe to the other. In the meanwhile, a

voltage drop takes place between any two points on the surface as a result of Ohm's law, and the voltage across the two voltage probes is measured by a high input impedance voltmeter. Because of the separation of the current source and voltage probes, the voltage measured in this technique is essentially independent of contact resistance, which is the main advantage of the four-probe technique over two-probe methods.

The resistivity of the film can be calculated with a geometric factor that takes into account of the thickness, sample shape and size, sample edge effect. After this factor is calculated from theory or obtained by calibration, the measurement of resistivity can be conducted efficiently. For square thin film sample, the geometric factor for the sample shape and edge effect is known, and the following resistances are measured by swapping the current and voltage probes:

$$R_{ij,kl} = \frac{V_{kl}}{I_{ij}} \quad (3-5)$$

where i, j, k, l are the position of contact on the edge of the samples. In total 8 resistances are measured, and the sheet resistance and resistivity are calculated as below:

$$R_{vertical} = (R_{12,34} + R_{34,12} + R_{21,43} + R_{43,21}) / 4$$

$$R_{horizontal} = (R_{23,41} + R_{41,23} + R_{32,14} + R_{14,32}) / 4$$

$$R = (R_{vertical} + R_{horizontal}) / 2 \quad (3-6)$$

$$\rho = 4.53tR$$

$$R_s = 4.53R$$

where ρ and R_s are resistivity and sheet resistance respectively.

3.2.6 Differential Scanning Calorimetry

Power-compensated differential scanning calorimetry (DSC) is a thermal analysis technique with the ability to measure heat absorbed or released during a reaction at high temperatures. DSC consists of a specimen chamber and a reference chamber which has exactly the same configuration. During the reaction in the specimen chamber, a different amount of heat needs to be supplied to the specimen depending on whether the reaction absorbs or releases heat. Power compensation by feedback circuits is employed to keep the temperature difference between the specimen and the reference zero, and the difference in power supplied to the two chambers corresponds to the change of heat associated with the reaction or phase transition in the specimen.

For a first-order phase transition which takes place at a particular temperature, the difference in power is usually peaked at the critical temperature. The total enthalpy ΔH associated with the first-order phase transition can then be found by calculating the area under the peak as

$$\Delta H = \int_{t_1}^{t_2} \left[\left(\frac{d\Delta H}{dt} \right)_{sample} - \left(\frac{d\Delta H}{dt} \right)_{reference} \right] dt \quad (3-7)$$

Isothermal and non-isothermal modes are the two of the most commonly used modes in DSC operation. In the isothermal mode, both the specimen and the reference chambers are kept as designated temperatures, and the difference in power supplied to the chambers is recorded as a function of time. On the other hand, in the non-isothermal mode, the temperatures of both chambers are raised linearly in time at a pre-defined heating rate β , and the difference in power

supplied is recorded as a function of temperatures. The isothermal mode has the advantage that the reaction takes place at a fixed temperature, therefore the kinetics of the reaction for a particular curves has only time as the variable. By repeating the isothermal DSC at different temperatures, the dependence of reaction kinetics on temperature and time can be easily separated. However, the isothermal mode suffers from a very small signal-to-noise ratio, hence the shape of the DSC curves are usually smeared and the baselines are not well-defined. It also has an initial stage when the DSC just reaches the pre-designated temperatures and has not become stabilized yet. A significant portion of the reactions could take place in the region, but the data are not usable before the equipment becomes stabilized.

On the other hand, although the data of non-isothermal mode are difficult to interpret as the time and temperature are intertwined, this mode has a much higher signal to noise ratio and a well-defined baseline. It also avoids the problem of instability by starting the measurement at temperatures much lower than the temperature range of interest. Therefore, the non-isothermal mode is usually chosen as the primary technique for DSC measurement. Since the kinetics of reaction could be complicated by the coupling between the time and temperature variables, the quantitative thermodynamic and kinetic modeling process needs to be adopted in order to extract the parameters of the reactions.

Calibrations for temperature, thermal lag, enthalpy and baseline must be done for the proper DSC operation. The temperature calibration is conducted by comparing true temperatures, usually the melting temperature of indium, to measured temperatures read by the thermocouples. The thermal lag calibration is performed by adjusting the onset temperature for a known reaction at different heating rates, in order to account for the heat capacity of the instruments. The enthalpy calibration proceeds by comparing the true enthalpies of melting of high purity

reference metals to the measured values. The purpose of baseline calibration is to obtain reliable and repeatable baseline which needs to be subtracted to get the heat associated with the reactions.

Although DSC is a powerful and technique in quantifying the reaction and phase transition kinetics, the scope of its applications is limited by the requirement that the mass of the specimen is at least in the range of milligrams, hence it is not directly applicable to thin films with mass usually only in the range of 0.01 milligrams. In addition, the films are usually deposited on substrates, the latter of which takes the major portion of mass in the system. Therefore, the signal of the films will be overwhelmed by that from the substrates. In order to overcome the above difficulties, the films for DSC measurement in this thesis is deposited to the thickness of micrometers in order to achieve enough mass. In addition, a sacrificial layer is used between the substrate and the films, so that the films could be lifted off by selectively etching the sacrificial layer using wet chemistry. This technique has been realized in the DSC measurement of FePt thin films using copper as the sacrificial layer and nitric acid as the etchant [Berry 2007, Wang 2011]. However, the same recipe cannot be applied to the investigation of β -W, because the thickness of β -W films is limited to less than 50nm before the β -W to α -W phase transition occurs. β -W also has a strong selectivity against the underlayer materials, hence the choice of sacrificial layers is limited. Therefore, it is critical to develop a recipe for preparing β -W specimen for DSC measurement.

4 – Deposition Conditions of β -W Thin Films

4.1 Experimental Details

4.1.1 Sputter Deposition of Tungsten Thin Films

Tungsten thin films were prepared by DC magnetron sputtering from 99.95% 3” diameter tungsten targets onto glass substrates. The substrates, including oxidized silicon and amorphous glass substrates, were cleaned in acetone and isopropyl alcohol and dried using nitrogen gas prior to deposition. The base pressure of the chamber was better than 2×10^{-8} torr before N_2 gas was introduced, and the mass spectrum of the gas composition was recorded with the Stanford RGA. Then N_2 gas was first introduced into a closed load lock at the pressure range of 100 to 700 torr, then flowed into the main chamber through an extremely small leakage at the gate between the load lock and the chamber. In this way, the gate of the load lock acted as a leak valve which allowed the N_2 pressure to be maintained in the range of 10^{-6} to 10^{-5} torr, and the pressure of N_2 in the chamber was controlled by the pressure at the load lock and measured by a cold cathode gauge. The typical values include the N_2 pressure of 1.2×10^{-5} torr N_2 in the main chamber with 730 torr in the load lock. 20 minutes are allowed for the gas flow to stabilize, and then the partial pressure of residual gas was recorded by the RGA in order to ensure no additional O_2 impurity flowed into the chamber together with N_2 .

For films deposited at elevated substrate temperatures, the substrates were heated to designated temperatures using the radiative filament corrected by the calibration curve. The temperature was maintained for 4 hours prior to the deposition. The extended time not only stabilized the temperature, but also allowed the gas impurities especially water vapor desorbed from the deposition chamber to be pumped away.

During the deposition, 3 mTorr Ar is introduced into the chamber flowing at 20 sccm as the sputtering gas. The tungsten films were deposited at the power of 25W, 50W and 100W onto the rotating substrates in the presence of argon and nitrogen gas. The typical deposition rates of tungsten were around 1 nm per minute at 50W. After the deposition was completed, the mass spectrum of residual gas was recorded again by the RGA.

4.1.2 Characterization of Tungsten Thin Films

PANalytical X-ray diffractometer with Bragg-Brentano geometry was used to perform a continuous θ - 2θ scan. The X-ray beam was generated from a Cu target with Cu $K\alpha$ -1 wave length of 1.540598 nm. The electric voltage and current through the Cu target were maintained at 45 kV and 40 mA, respectively. In order to obtain the balance between the repeatability, efficiency and angular resolution, the data were acquired using the same configuration of the optics, including the use of 15 mm mask in front of the detector to confine the area of the X-ray beam, 0.5 mm divergence slit and 1 mm anti-scattering slit to optimize the tradeoff between intensity and angular resolution. A linear detector was used to collect the diffracted X-ray beams, and this detector contained 255 channels and spanned 5° in space. The ability of the linear detector to efficiently collect signal from a wide angle allowed the quantification of phases in ultrathin films at about 10nm thickness.

The X-ray reflectivity measurement was conducted using Rigaku Ultima III XRD at Center for Functional Nanomaterials at Brookhaven National Laboratory. Prior to the measurement, the position and angle of the specimen were adjusted, so that the intensity of the reflected beam was maximized. In this way, the specimen was properly aligned to the optics of

the diffractometer. The reflectivity curve was recorded between $\theta = 0^\circ$ to 3° , and was analyzed using Rigaku Reflectivity simulation software.

The resistivity of the thin films were measured with Signatone CM-170 probe station at Center for Functional Nanomaterials at Brookhaven National Laboratory. This equipment had four spring loaded probes contacted to corners of the films, and the van der Pauw method was used to extract the value of electrical resistivity. Since tungsten films easily get oxidized in air, the measured resistivity consisted of contributions from both the tungsten and the oxide layer.

The 20nm β -W films were used for the XPS measurement at Evans Analytical Group. Since the surface of the films was covered by a thin layer of oxide, the oxide layer was removed first in the ultra-high vacuum inside the XPS chamber by the bombardment of Ar ion beam. After 30 minutes of bombardment, the intensity of the oxygen peak became a constant and did not decrease with further bombardment, thus the surface oxide had been removed and the oxygen peak originated from the bulk of the films. After the surface cleaning, 30 minutes of pumping time was allowed so that the Ar atoms adsorbed on the specimen surface could be removed. Then the XPS measurement was conducted using the X-ray beam generated by an Al target.

The plan-view TEM samples were prepared by mechanical thinning, dimpling, and then ion milling until a small hole was observed at the center of the specimen. The cross-sectional TEM samples were prepared by first coating the specimen by carbon film then shaped and thinned using focused-ion beam equipped on Helios scanning electron microscopy.

The plan-view bright-field images were obtained using JEOL 2100-F TEM at Center for Functional Nanomaterials at Brookhaven National Laboratory. An objective aperture is used so that only the direct beam could transmit and the corresponding bright field images were

captured. The HRTEM images were captured without using the objective aperture, so the beams interfered and the phase could be reconstructed at the imaging plane. The EELS spectrum was captured using JEOL 2100-F TEM.

The images of the cross-sectional TEM were obtained using similar method in the FEI Talos F200X TEM at Columbia University. A double tilt holder was used in order to orient the Si substrate along its zone axis to minimize the number of Si diffraction spots. Then the bright field images and dark field images were recorded by charge-coupled devices. The cross-sectional sample was prepared by the Evans Analytical Group.

4.2 Results

4.2.1 Film Composition Measurement

The spectrum of β -W film after the surface oxide was removed by argon ion beam bombardment is shown in Figure 4.1. The background of the spectrum is generated by the Bremsstrahlung radiation inherent in the non-monochromatic X-ray sources [Kibel 2003]. The XPS spectrum shows the existence of tungsten, oxygen, and nitrogen elements in β -W films with the detection limit of 1 at%.

The composition of the β -W film was calculated from the ratio of the peak areas corrected by the emission coefficient of the corresponding elements, and the result is shown in Table 4.1. Although the oxygen molecules were removed from the chamber prior to the deposition, as evidenced by the RGA spectrum in Figure 4.2, the film still contains about 3 at% oxygen. On the other hand, although the pressure N_2 gas was in the range of 10^{-5} to 10^{-6} torr, and

it was higher than that of other gas impurity as shown in Figure 4.2, the β -W film only contains negligible amount of nitrogen element.

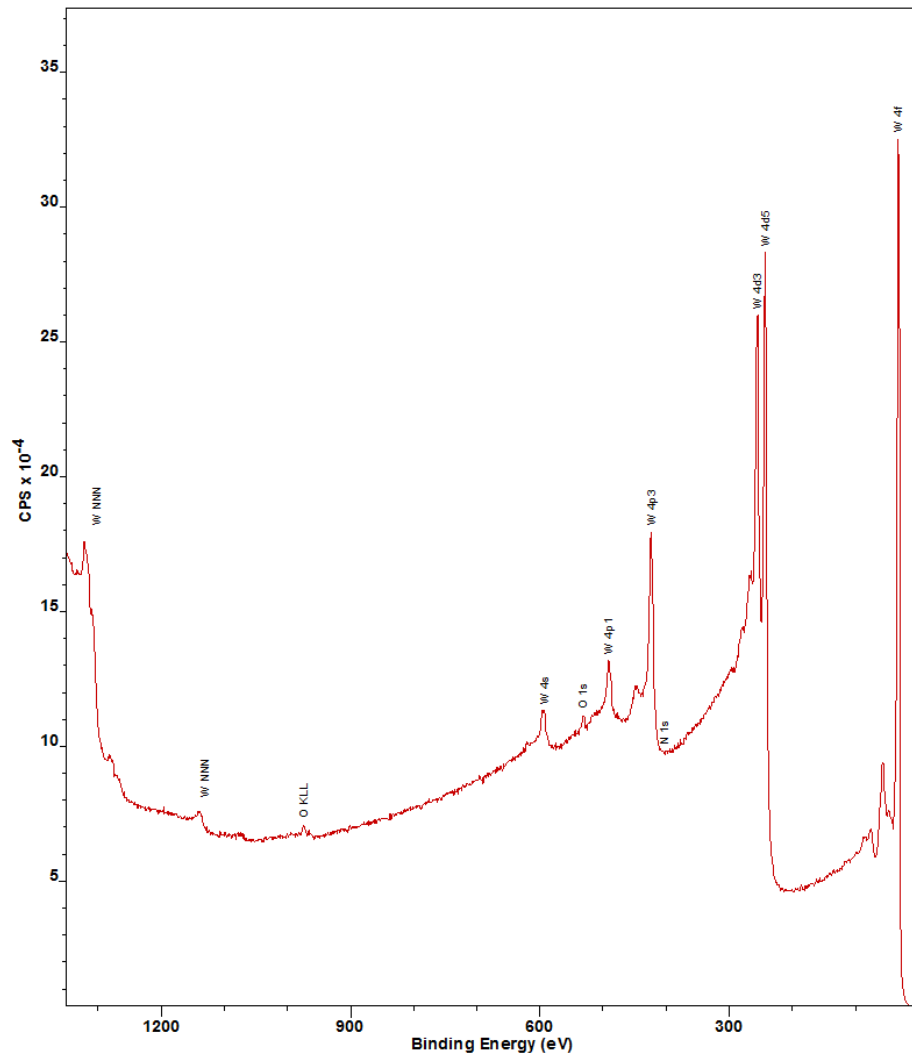


Figure 4.1. The XPS spectrum of β -W thin films after the surface oxide was removed by argon ion beam bombardment.

The shape of XPS peaks of W, O and N elements respectively are shown in Figure 4.3. The tungsten peaks contain the contribution from the electrons in the state of $5p_{3/2}$, $4f_{5/2}$ and $4f_{7/2}$. The relative intensity of the peaks and their positions of β -W, along with the values of pure α -W are shown in Table 4.2. The relative intensity and the positions of W peaks in β -W are the same as those of α -W. On the other hand, the peak of tungsten oxide and nitride should be located at about 39eV, which is not observed in the spectrum. Therefore, it is concluded that the deposition procedure of tungsten films with N_2 impurity could produce β -W films with high purity.

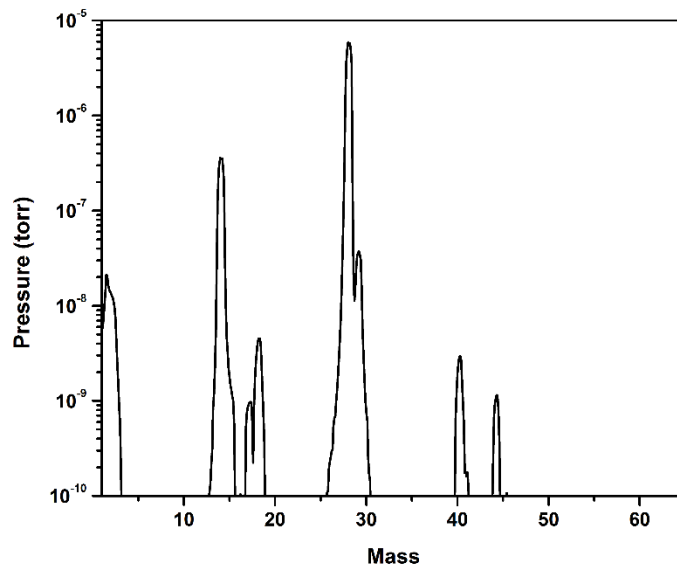


Figure 4.2. The RGA spectrum of base pressure in the chamber prior to the introduction of Ar for deposition.

The low concentration of nitrogen element at 0.4 at% could be attributed to the non-volatility of nitrogen molecules. As shown by the study of reactive sputtering of tungsten nitride in argon/nitrogen mixture [Baker *et al.*, 2002, Shen *et al.*, 2000], in order to achieve nitrogen

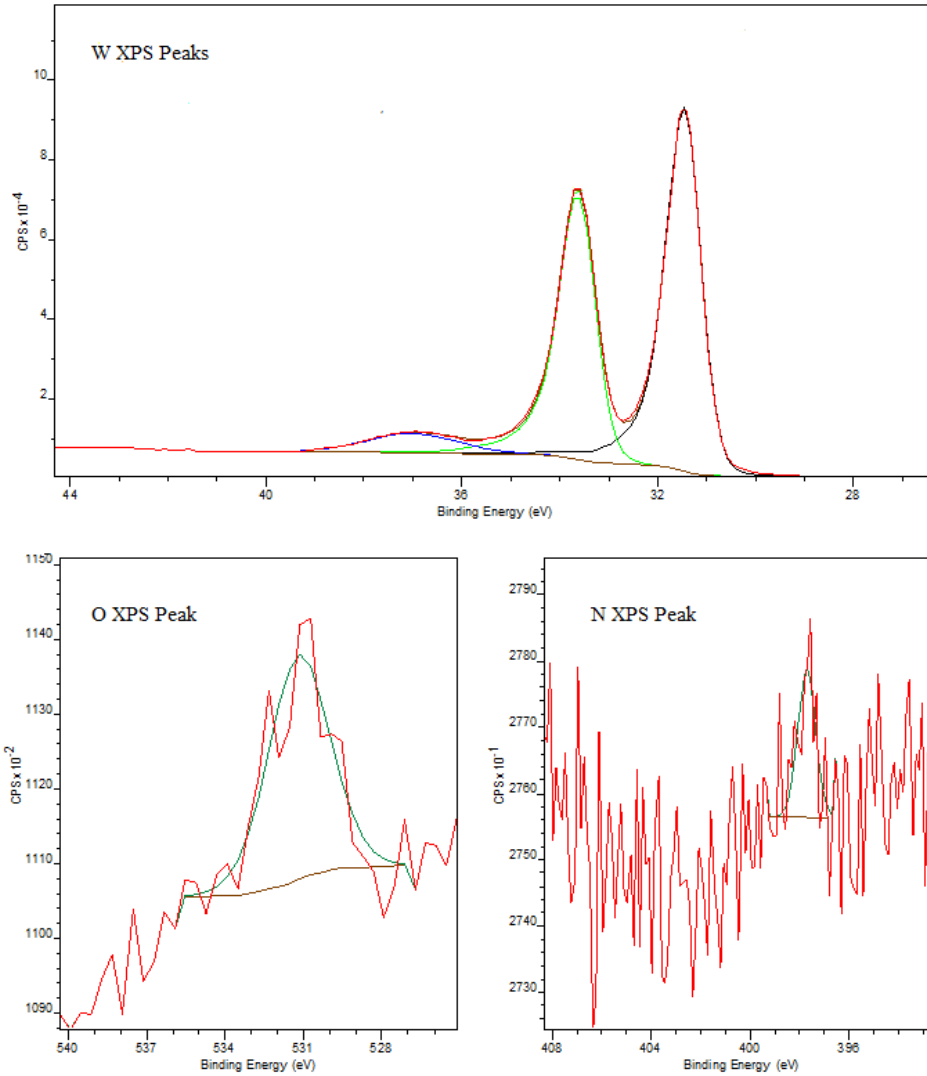


Figure 4.3. The shape of the XPS peaks of W, O, and N elements in the β -W thin films.

concentration of about 10 at%, the pressure of nitrogen gas in the deposition chamber needs to be in the order of 1 mTorr. Therefore, it is understandable that the concentration of nitrogen atom in β -W deposited at the N_2 pressure of 10^{-5} torr is negligible in the films.

Table 4.1. The composition of β -W thin films calculated from XPS spectrum.

Element	at %
W	96.4
O	3.2
N	0.4

On the other hand, the presence of 3.2 at% oxygen element could be attributed to the reaction of W atoms with the residual water vapor in the chamber, since the sputtered atoms are highly reactive before being incorporated and buried inside the films. This explanation is evidenced by the RGA spectrum obtained after the deposition as shown in Figure 4.4. Prior to the deposition, the absence of ions with mass-to-charge ratio of 32 indicates the absence of O_2^- , and the presence of ions with mass-to-charge ratio of 16 shows the existence of O^- in the residual gas. Therefore, the O atoms could only originate from the cleavage of H_2O molecules instead of O_2 molecules. After the deposition, the signal of O^- ions has a smaller magnitude, while the concentration of H^- increased as indicated by the higher signal at mass-to-charge ratio of 1 and 2. The change of RGA spectrum is consistent with the explanation that the water vapor is decomposed into hydrogen gas by the W atoms. Therefore, the oxygen incorporated inside the β -W is caused by the residual water vapor in the chamber instead of oxygen molecules. It is difficult to remove the water vapor with the deposition equipment used in this thesis, since the water vapor has a relatively high boiling point and hence a slow pumping speed with turbo

pumps, so the purity of the β -W is optimum. On the other hand, ideally the content of oxygen in β -W could be removed by baking the chamber, and the removal of oxygen does not interfere with the formation of β -W phase. Therefore, this technique could theoretically deposition pure β -W films with negligible N or O contamination.

Table 4.2. The relative intensity and peak positions of β -W and α -W XPS spectrum.

Peak	Relative Intensity in β -W(%)	Relative Intensity in α -W(%)	Peak Position in β -W(eV)	Peak Position in α -W(eV)
W 5p _{3/2}	6.56	6.3	37.02	36.87
W 4f _{5/2}	40.28	40.1	33.57	33.46
W 4f _{7/2}	53.17	53.6	31.40	31.30

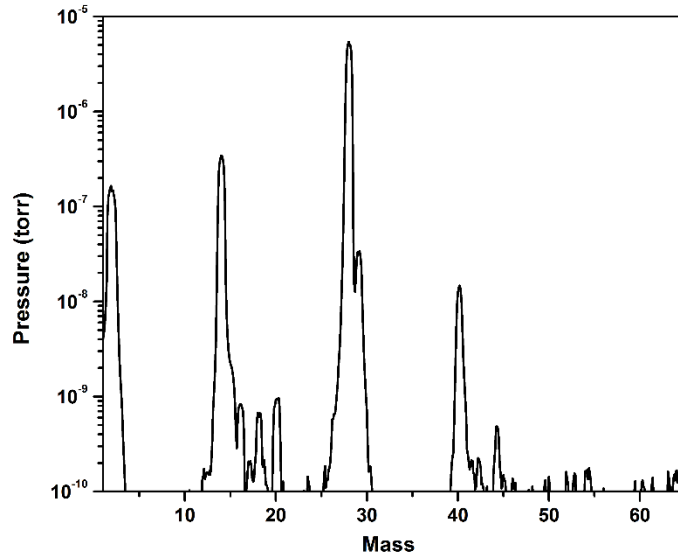


Figure 4.4. The RGA spectrum of base pressure after the deposition of β -W.

4.2.2 Relationship between β -W Formation and Deposition Conditions by XRD and Resistivity Measurement

The XRD pattern of the 112 nm-thick W film deposited at 1.2×10^{-5} torr N_2 is shown in Figure 4.5. The film consists primarily of β -W with a lattice constant of 0.506 ± 0.001 nm, close to the value reported in the references [An 2005, O'Keefe *et al.*, 1995, Kizuka *et al.*, 1993]. In addition to β -W, the presence of a small amount of α -W is indicated by its weak (211) peak in the XRD pattern. Since it has always been found that the volume fraction of β -W decreases in films with larger thicknesses and gets completely transformed into α -W above 100nm [Pai *et al.*, 2012, Choi *et al.*, 2011, Rossnagel *et al.*, 2002], the dominance of β -W in the 112 nm thick films shown in Figure 4.5 confirms that the use of N_2 as the impurity gas during sputtering facilitates the formation of β -W.

In order to quantify the volume fraction of β -W, the XRD measurements of 14-nm-thick tungsten films deposited in N_2 were used. The XRD patterns of these films deposited at different pressures of N_2 are shown in Figure 4.6. The (211) and (200) peaks of β -W phase get stronger while the central (210) peak becomes weaker as the pressure of N_2 increases. Therefore, it is concluded that the N_2 in the deposition chamber has a significant influence on the formation of β -W phase.

In order to quantify the volume fraction of β -W, some complications caused by the crystallographic structure and texture of α - and β -W phases need to be addressed. As shown in Figure 4.5, the (110) peak from α -W and the (210) peak from β -W coincide, since the angular resolution of the diffractometer used in this study is not high enough to resolve them. The (200) peak from α -W is also absent as a result of crystallographic texture of this phase in the films. Therefore, the presence of α -W can only be determined through the appearance of its (211) peak,

which is extremely weak and cannot be observed for thinner films or those containing only a small

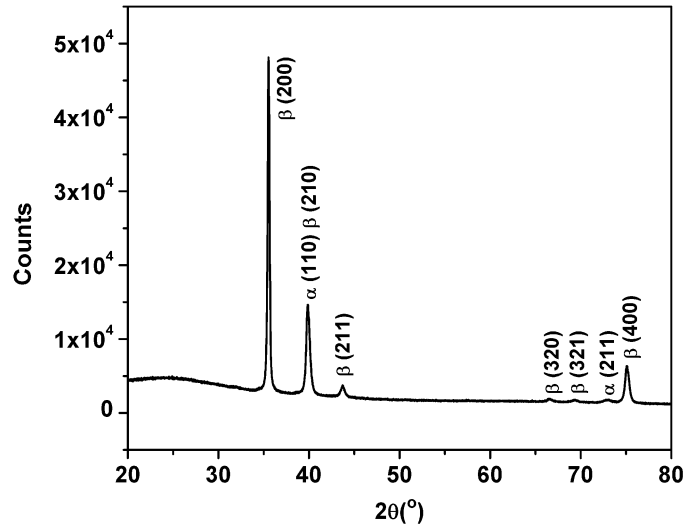


Figure 4.5. The XRD pattern of the 112 nm-thick W film deposited at 1.2×10^{-5} torr N_2 .

amount of α -W. The calculation of volume fraction is also complicated by the presence of texture in the films, which modulates the intensity of individual XRD peaks of both phases. The above difficulties are addressed by using Klug's equation [Perchinsky *et al.*, 2009] under the assumption that the preferred crystallographic texture in the film is invariant with the phase fraction under fixed thicknesses, and that the X-ray absorption lengths in both α -W and β -W phase are the same. In that way, the XRD pattern can be regarded as a superposition of the patterns of α -W and β -W multiplied by their volume fraction, respectively. The overlapping peak at about 40° as the superposition of the (110) α -W and (210) β -W reflections is used for the calculation, as the intensity of this peak is the most sensitive to the change of β -W volume fraction. Furthermore, the intensity of this peak is invariant with deposition parameters at fixed β -W volume fraction.

Klug's equation for these peaks can thus be written in equation 4-1 as:

$$I = f_{\alpha}I_{\alpha,110} + f_{\beta}I_{\beta,210} \quad (4-1)$$

where f_{α} , f_{β} are the volume fraction of α - and β -W, I is the total peak intensity at around $2\theta = 40^{\circ}$, $I_{\alpha,110}$ and $I_{\beta,210}$ are respectively the intensity of (110) α -W and (210) β -W peaks of reference samples containing only one phase, and are taken from the XRD spectra of films deposited with no N_2 and 1.2×10^{-5} torr of N_2 , respectively.

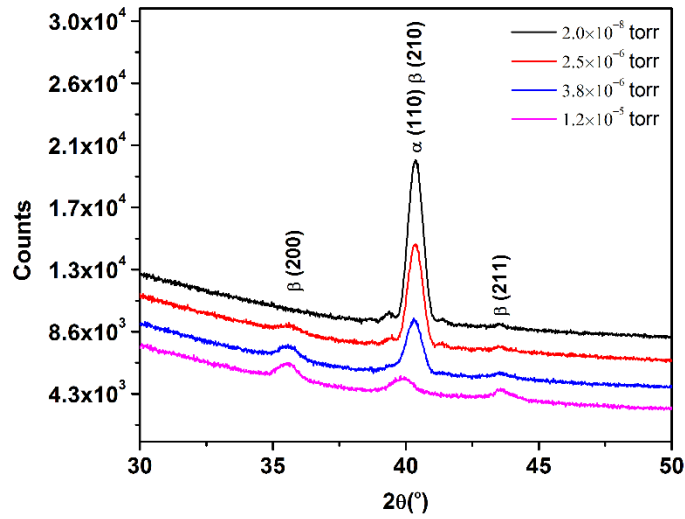


Figure 4.6. The XRD pattern of the 14nm tungsten films deposited at different N_2 pressure in the chamber.

The resistivity measurement of β -W is adopted to verify the volume fraction calculated from equation 4-1. The dependence of conductivity on β -W volume fraction is shown in Figure 4.7. The resistivity of the single phase α -W film is calculated as $24 \mu\Omega\cdot\text{cm}$, in good agreement with the values of 19 to $30 \mu\Omega\cdot\text{cm}$ for 10 nm-thick films reported previously [Choi *et al.*, 2011, Rosnagel *et al.*, 2002]. The resistivity of the single-phase β -W film was measured as $160 \mu\Omega\cdot\text{cm}$, and this value is approximately seven times of that of single phase α -W film, consistent with prior studies that the resistivity of β -W films is 5 to 10 times those for α -W films [Petroff *et al.*, 1973]. Therefore, it is permissible to use the films deposited at no N_2 and 1.2×10^{-5} torr N_2 as references in equation 4-1 for the calculation of β -W volume fraction.

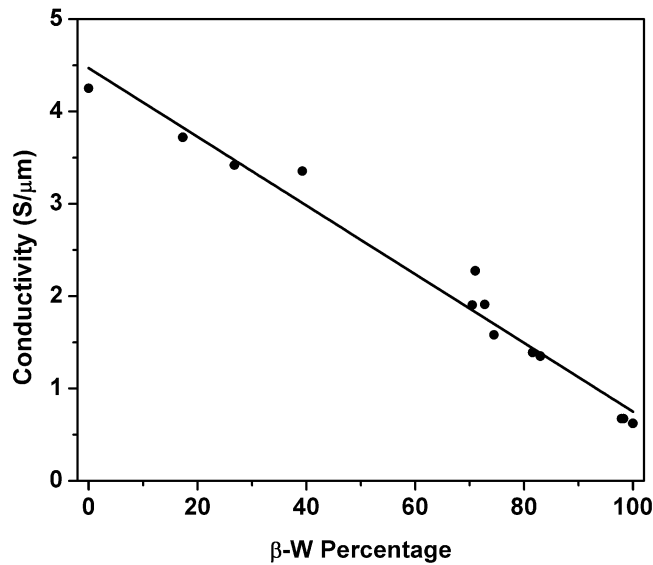


Figure 4.7. The electrical conductivity of 14 nm β -W thin films. The volume fraction of β -W is calculated using equation 4.1.

In the intermediate region of the deposition conditions, the tungsten films contains a mixture of α - and β -W, and the conductivity shows a linear dependence upon the volume fraction of β -W calculated from the corresponding XRD patterns. The linear dependence on phase fraction for conductivity is commonly found for two-phase mixtures, which contain spherical particles with conductivity at the same order of magnitude [Kasap et al., 2007]. Therefore, the self-consistency of equation 4-1 is shown as self-consistent.

The relationship between f_β calculated using equation 4-1 and nitrogen partial pressure is shown in Figure 4.8. There is only a small amount of β -W formed below 10^{-6} torr N_2 . As the pressure of nitrogen is increased, the volume fraction of β -W increases sharply and saturates to 100% at a pressure of approximately 7×10^{-6} torr N_2 .

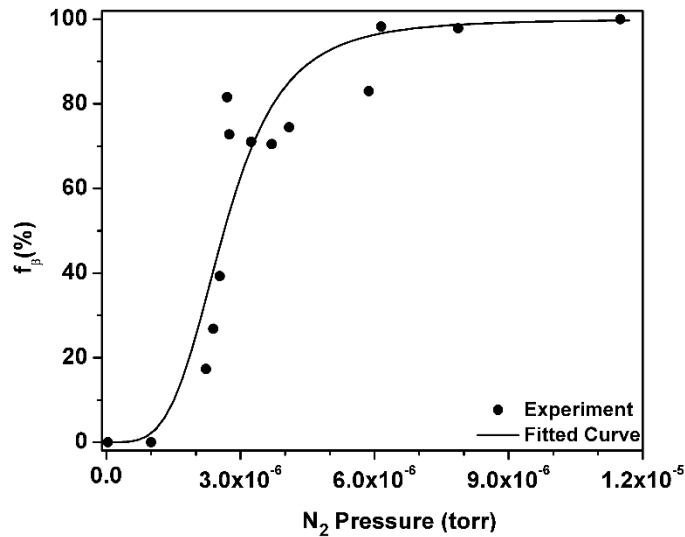


Figure 4.8. The relationship between volume fraction of β -W in 14 nm-thick films deposited at 50W and the N_2 pressure. The volume fraction of β -W is calculated using equation 4-1.

In addition to the films deposited at 50W, the XRD pattern of films deposited at 1.2×10^{-5} torr N_2 with different power is shown in Figure 4.9, and it is clear that the volume fraction of β -W decreases with higher deposition rate/power at fixed nitrogen pressure. This observation is consistent with the process that the formation of β -W was made possible without introducing gas impurity by simply depositing at ultra-low powers of 3W [Hao *et al.*, 2015]. The relationship between the N_2 pressure and the volume fraction of β -W deposited at different power is shown in Figure 4.10. The change of the shape of the curves indicates that the relationship between β -W volume fraction and the partial pressure is coupled to its dependence on deposition power.

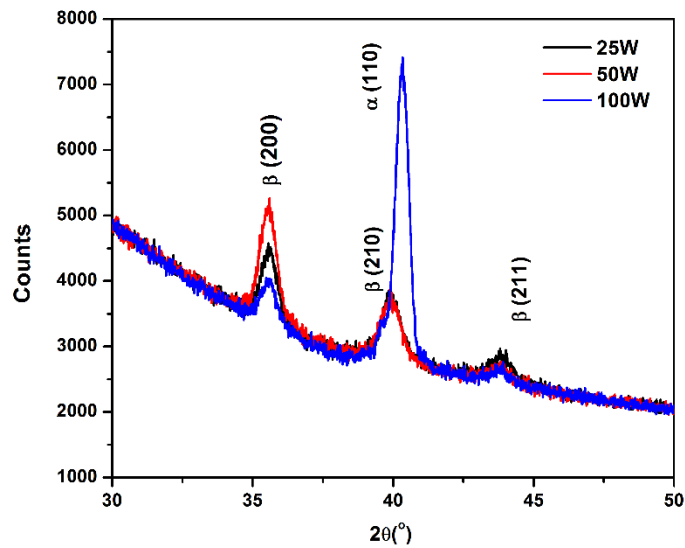


Figure 4.9. The XRD pattern of tungsten films deposited at fixed pressure of 1.2×10^{-5} torr N_2 and different power of 25W, 50W, and 100W.

The dependence of β -W volume fraction on substrate temperature during deposition at a fixed pressure of N_2 of 1.2×10^{-5} torr is shown in Figure 4.11. The figure shows f_β decreases at higher substrate temperatures, hence lower substrate temperature is favored for the deposition of

β -W films. The relationship between the substrate temperatures and β -W volume fraction will be used to model the formation process of β -W phase, as will be discussed in the following section.

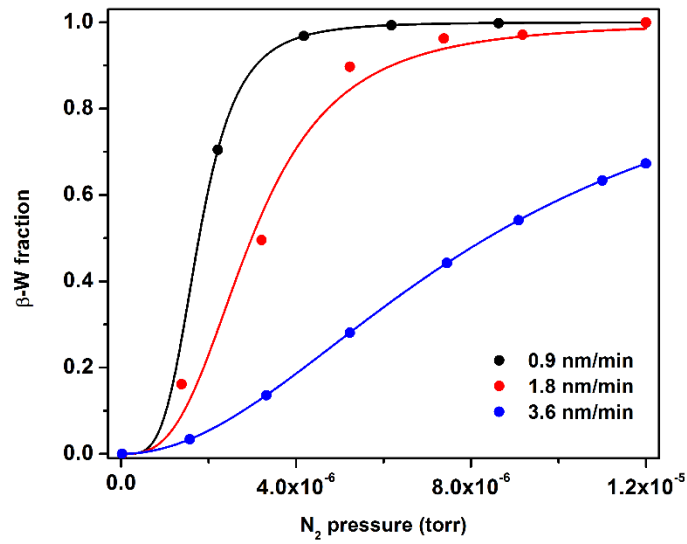


Figure 4.10. The relationship between the N_2 pressure and the volume fraction of β -W with different deposition power.

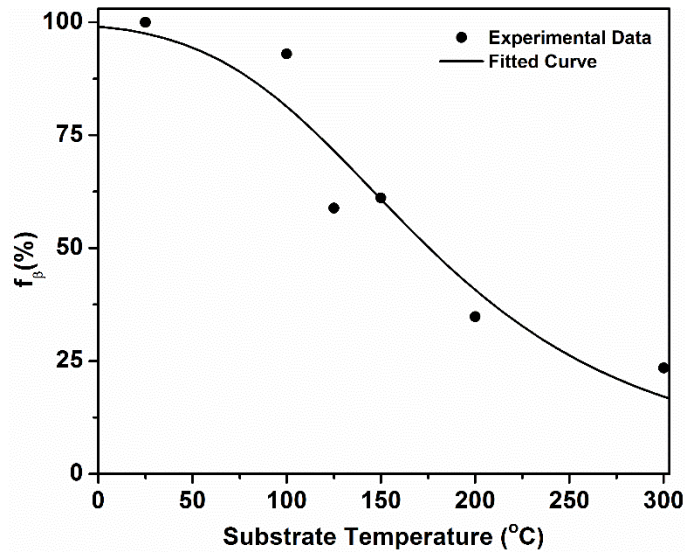


Figure 4.11. The dependence of β -W volume fraction on substrate temperature for films deposited at the N_2 pressure of 1.2×10^{-5} torr.

4.2.3 Microstructure of β -W Thin Films by TEM

The plan-view bright field image and the corresponding electron diffraction patterns of W films deposited under different pressure of N_2 is shown in Figure 4.12. The film deposited at 2×10^{-8} torr contains only α -W at a grain size of about 70 nm as seen in Figure 4.12(a). At higher pressure of N_2 , an increasing number of β -W grains appear. The grain size of β -W is determined to be about 4 nm using high resolution lattice images such as that seen in Figure 4.12(e). At the N_2 pressure of 1.2×10^{-5} torr, no α -W grains are identified. Therefore, it is concluded that the films deposited at the N_2 pressure of 1.2×10^{-5} torr contains only β -W, and it is justified to use the XRD pattern of such films as the reference for volume fraction calculation.

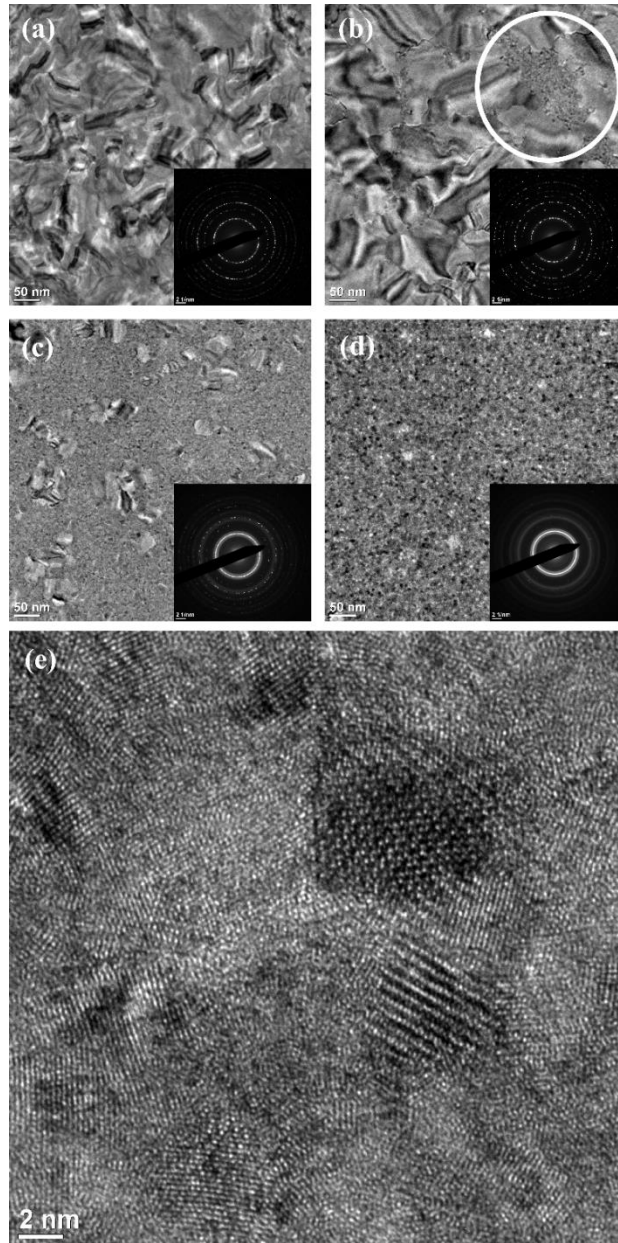


Figure 4.12. Bright-field transmission electron micrographs of 14 nm-thick W films deposited at N_2 pressures of 2.0×10^{-8} (a), 2.2×10^{-6} (b), 3.9×10^{-6} (c) and 1.2×10^{-5} torr (d). The selected area diffraction patterns are shown as insets in the lower right. Figure (e) is a high-resolution transmission electron micrograph of β -W grains with atomic resolution. The white circle in (b) is used to mark a region of β -W.

The EELS spectrum acquired by focusing the electron beam onto β -W grains is shown in Figure 4.13. No peaks corresponding to the existence of oxygen or nitrogen elements was observed in the spectrum, which is consistent with the measurement by XPS.

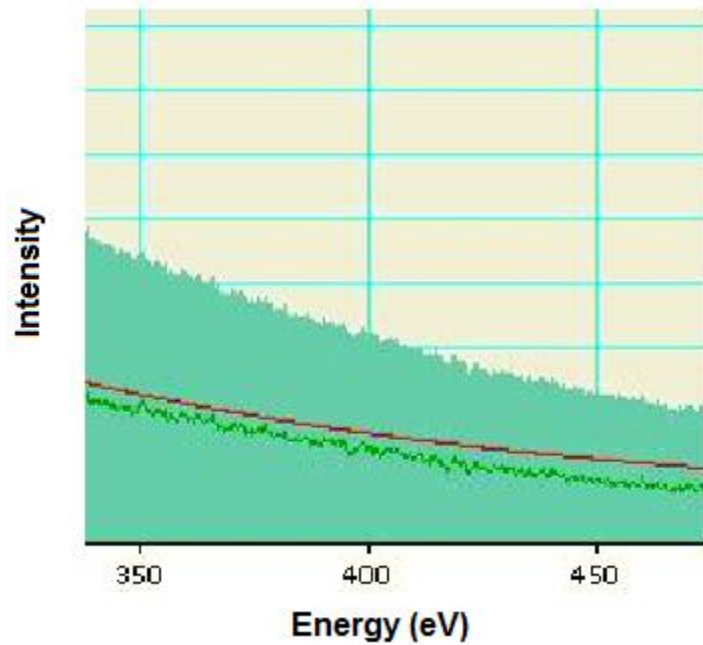


Figure 4.13. The EELS spectrum of β -W grains. No evidence of nitrogen was found in β -W grains as indicated by the absence of energy peaks at 400 eV.

The bright field image of the cross section of β -W is shown in Figure 4.14. Due to the extremely weak contrast at the grain boundaries, the microstructure of β -W is not as clear as that from the plan-view bright field image. The cross-sectional TEM image shows β -W still forms columnar grains with high aspect ratio even though the deposition is conducted with nitrogen impurity. Therefore, it is concluded that the interaction between N_2 molecules and tungsten

atoms is very weak that the out-of-plane growth of β -W grains is not interrupted by the nucleation of new β -W grains.

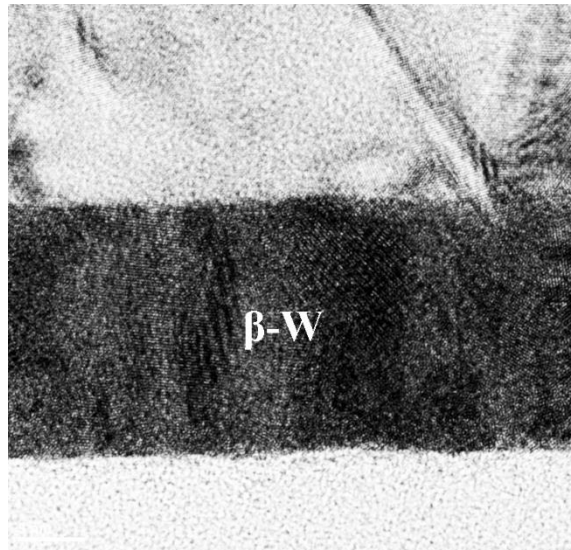


Figure 4.14. The bright-field cross-section TEM image of the β -W thin films.

4.3 Discussion

4.3.1 Advantages of β -W Deposition with Nitrogen Impurity

Some parts of this chapter are based on a manuscript entitled “Topologically Close-Packed Phases: Deposition and Formation Mechanism of Metastable β -W in Thin Films” by Liu and Barmak in journal *Acta Mater.* **104**, 223 (2016) [Liu, 2016].

In the previous studies of β -W deposition, oxygen impurity was used to stabilize the β -W thin films during the deposition process, and the pressure of oxygen gas needed to be higher than 3×10^{-5} torr in order to obtain β -W in tungsten films [Shen *et al.*, 2000]. However, the films were heavily contaminated by the presence of 10 at% oxygen as detected by XPS [Shen *et al.*, 2000]. At higher oxygen pressure, the films were amorphized due to the formation of oxide. In addition, the use of oxygen gas in the deposition chamber oxidizes other sputtering targets and creates water vapor which is difficult to pump away. Therefore, despite its effect in stabilizing β -W, oxygen impurity is undesirable in the production of high quality of β -W films for spintronics. On the other hand, the method introduced here using nitrogen impurity is available for the deposition of β -W films that contain only 0.4 at% nitrogen. Furthermore, the 3 at% oxygen impurity in the films can always be eliminated in deposition systems with better base pressure or by baking the system to drive off the water molecules adsorbed on chamber walls, since oxygen is not responsible for the formation of β -W phase. This technique also has the advantage that the N_2 impurity is non-volatile, hence the surface of other targets is not contaminated and no additional gas contamination such as water vapor would be created. Therefore, the technique of depositing β -W films with nitrogen impurity is advantageous over oxygen in most aspects.

As mentioned above, the deposition of β -W have also been realized using negative bias, high argon pressure, or extremely low deposition power, and these methods all suffer from

certain disadvantage compared with that using N₂ impurity. Biasing the substrate is very difficult to control and is rarely used in the manufacturing process, hence the deposition of β -W with bias requires upgrading the existing deposition equipment. On the other hand, β -W deposition with N₂ impurity can be realized simply by mixing the Ar gas with N₂ with specific ratio. The methods adopting high argon pressure and low deposition power both suffer from the disadvantage of low deposition rate, which has a negative influence on the yield of manufacturing. In comparison, the deposition technique using N₂ allows reasonable deposition rates while the β -W phase remains stable. In conclusion, the β -W deposition technique with N₂ impurity has the advantages of simple realization and high manufacturing yield.

4.3.2 Modeling the Effect of Deposition Parameters on β -W Formation

It was speculated that β -W was essentially a type of A15 structured tungsten oxide with a composition that is off its AB₃ stoichiometry [Hägg *et al.*, 1954, Sinha 1972]. However, the XPS and EELS spectra show that the nitrogen impurity responsible for the formation of β -W is not significantly incorporated in the films, and the oxygen element detected by XPS is not the factor controlling the volume fraction of β -W in the films. Therefore, it can be concluded that β -W is in nature an A15 structured allotrope of α -W instead of an A15 structured compound.

Considering the absence of nitrogen element in the films, as well as the difficulty in reaction between nitrogen and tungsten atoms, it can be inferred that nitrogen gas stabilizes the β -W through weak physical interaction instead of strong chemical reactions. On the other hand, there is no direct experimental technique that allows a straightforward determination of the effect of N₂, because the absence of nitrogen in β -W films makes it impossible to conduct any measurements on the state of nitrogen element such as its valence state by nuclear magnetic

resonance spectroscopy, and the in-situ measurement of the formation process of β -W by UHV equipment is not feasible in the sputter deposition process. Therefore, the only reasonable way to investigate the formation process of β -W with N_2 impurity is to model the dependence of β -W volume fraction on the deposition conditions.

The dependence of f_β , the volume fraction of β -W, on N_2 pressure, P_{N_2} , in Figure 4.8 shows a sigmoidal shaped curve. Assuming the tungsten films can only be a mixture of α -W and β -W phase, the function describing the dependence of f_β upon P_{N_2} has to satisfy the following requirements: (i) it must be a monotonically increasing function of P_{N_2} , (ii) it must approach zero as P_{N_2} approaches zero, and, 3) it must approach 100% as P_{N_2} goes to infinity. One function that fulfills the above requirements has the following form in equation 4-2 as:

$$f_\beta = \frac{(P_{N_2} / P_o)^n}{1 + (P_{N_2} / P_o)^n} \quad (4-2)$$

where P_{N_2} is the pressure of N_2 , P_o is a fitting coefficient that is invariant with N_2 pressure when other parameters are kept fixed. The best fit to the experimental data in Figure 4.8 gives the values of $P_o = 2.63 \times 10^{-6}$ torr and $n = 3.97 \approx 4$.

Equation 4-2 has the form of the Langmuir-Freundlich (LF) adsorption isotherm, where f_β is equivalent to the surface coverage of adsorbed species, and P_o is equivalent to $1/K_{LF}$ where K_{LF} is the equilibrium constant [Masel 1996]. Given the similarity between equation 4-2 and LF isotherm, it is reasonable to infer that the adsorption of N_2 onto the glass substrates is an integral step in the formation of β -W phase in thin films.

In the LF isotherm, the exponent n is the index of heterogeneity describing the non-uniform distribution of adsorption enthalpies and affinities over the substrate surface. This exponent is usually between 0 and 1, for the case of non-interacting adsorbates [Masel 1996]. Exponents $n > 1$ indicate adsorbate-adsorbate interactions, such as the situation where the adsorption of hydrogen on the (110) surface of a Ni film [Christmann *et al.*, 1974] with an exponent is $n = 1.5$ [Masel 1996]. Therefore, the value of the exponent in the current study with $n = 3.97 \approx 4$ implies the strong attractive adsorbent-adsorbent interaction which makes the adsorbed nitrogen species behaves effectively like clusters consisting of n molecules. The similarity between the equation for the surface coverage of such clusters and the volume fraction of β -W leads to the conclusion that on the surface of the substrate where such clusters exist, the formation of β -W takes place; In areas free of such nitrogen clusters, α -W forms instead. Thus, as surface coverage of nitrogen increases at higher pressure, so does the volume fraction of β -W relative to α -W.

In order to show that the similarity between equation 4-2 and the LF isotherm is not coincidence, the above mechanism can be further supported by modeling the variation of f_β with substrate temperature at a fixed P_{N_2} shown in Figure 4.11. Assuming an thermally-activated adsorption, P_0 is then given by equation 4-3 as

$$P_0 = P_{0e} e^{-\frac{E}{RT}} \quad (4-3)$$

where E is the activation energy, and P_{0e} is the pre-exponential term that is invariant to the pressure and substrate temperature with other parameters fixed. By fitting the data in Figure

4.11 for f_β obtained at a fixed nitrogen pressure of $P_{N_2} = 1.2 \times 10^{-5}$ torr and power of 50W, the values of P_{oe} and E are calculated as 4.0×10^{-5} torr and 6.8 kJ/mol, respectively. The value of the activation energy is in close agreement with the activation energy of 7 kJ/mol [Wittcoff 2012] for the physisorption of N_2 molecules onto glass substrates. Therefore, the similarity between these activation energies provides independent evidence for the conclusion that the adsorption of nitrogen molecules onto the glass substrate is involved in the formation of β -W in thin films.

The power dependence of β -W formation was investigated by fitting the data in Figure 4.10 using equation 4-2, and the parameters P_0 and n were treated as fitting variables that have implicit dependence on the deposition rate. The results of the fitting in Figure 4.10 show that equation 4-2 can be used to describe the dependence of β -W on N_2 pressure at all powers, thereby this equation is likely to account for the mechanism for β -W formation in thin films.

The values of the fitting parameters are shown in Table 4.3. The value of P_0 , which is effectively the pressure of N_2 when the volume fraction of β -W is 50%, has larger values at larger deposition rates, and this trend is consistent with the observation that the formation of β -W phase is more difficult at higher deposition rates.

Table 4.3. P_0 and n as fitting parameters in equation 4-2 at different deposition rates.

Deposition Rate (nm/min)	Power (W)	P_0 (10^{-6} torr)	n
0.9	25	1.78	4
1.8	50	2.98	3
3.6	100	8.37	2

On the other hand, the value of n decreases when the power increases. Since the value of n indicates the degree of attractive interaction between N_2 molecules, the observed trend shows the attractive interaction decreases at higher deposition power, and this observed trend can be rationalized as follows: Essentially, there is no intrinsic attractive interaction between N_2 molecules except for the negligible van der Waals force, so the attractive interaction between adsorbed N_2 molecules as shown in the model is mediated by their mutual interaction with W atoms. As multiple N_2 molecules are attracted to the same W atom, an effective attractive interaction will appear between these N_2 molecules. At higher deposition rates, the flux of W atoms increases relative to the density of N_2 molecules, hence the number of attraction center is larger and fewer N_2 molecules are attracted to the same center, resulting in the decrease of degree of interaction n . In addition, accompanying the increase of the deposition rate is usually the higher kinetic energy of the sputtered atoms, which makes it easier for the W atoms to break out of bonds with N_2 molecules. As a result, the effective interaction between the W and N_2 molecules decreases further at higher deposition rates. In conclusion, the decrease of n at higher deposition rates can be explained by the decrease in the interaction between tungsten atoms and N_2 molecules by higher tungsten flux and larger kinetic energy of tungsten atoms.

Additional clues about the role of N_2 molecules in nucleation of α -W and β -W can be obtained by examining the microstructures seen in the TEM images. As seen in Figure 4.12 (a), α -W has a relatively large grain size of about 70 nm, from which it is concluded that the nucleation of α -W is difficult. In addition, since it is reported that post-deposition annealing even at temperatures as high as 850 °C did not result in any observable grain growth [Rosnagel *et al.*, 2002, Choi *et al.*, 2011], thus the grain size of α -W is determined by its nucleation density at the time of deposition. In contrast, the grain size of \sim 4 nm for β -W implies a large density of

nucleation sites, which are likely to originate from the heterogeneous nucleation on the small clusters of interacting nitrogen adsorbates. In other words, the nitrogen adsorbates on the surface of the glass substrate provide the nucleation sites for β -W, allowing it to nucleate more readily than α -W, and the density of such nucleation sites determines the volume fraction of β -W in thin films.

To address why β -W can more readily nucleate on the adsorbed nitrogen clusters, it is useful to consider that the A15 structure is a topologically close-packed Frank-Kasper structure [Graef *et al.*, 2012]. Topologically close-packed structures have exclusively tetrahedral interstices by contrast to other simple metal structures (fcc, hcp, bcc) that have a mixture of tetrahedral and octahedral interstices. It is speculated that the nitrogen adsorbate clusters provide suitable templates for the formation of the W tetrahedra, which then pack as edge-sharing tetrahedra to form the icosahedral triangulated coordination polyhedra (CN12 Kasper polyhedra) that in turn form the crystalline grains of the A15 structure [Graef *et al.*, 2012]. The formation of every new edge-sharing tetrahedron requires the addition of only a single W atom to an existing triangular face.

4.4 Summary

The β -W films were deposited by introducing N_2 gas in the pressure range of 10^{-6} to 10^{-5} torr into the chamber, and this deposition method is advantageous over the existing methods such as by using oxygen impurity, high argon pressure, and low deposition power. A model has been proposed to quantify the dependence of volume fraction of β -W on deposition parameters. The model shows that the nucleation of β -W takes place on N_2 clusters adsorbed onto the substrate, and this model is able to explain the relationship between volume fraction of β -W and the

deposition parameters, including nitrogen pressure, deposition rate and substrate temperature, and mechanism based on the model is also supported by the evidence from the microstructure of the films.

5 – Deposition of β -W on Other Underlayers and Substrates

5.1 Motivation

It has been shown in previous chapters that the formation of β -W is made possible on amorphous SiO_2 layer in the presence of N_2 impurity. However, in addition to amorphous SiO_2 underlayer, it is common for electronic device fabrication that the films be deposited onto other functional underlayers, such as TaN/Ta as adhesion layer for Cu electrodeposition [Gupta 2009], and it is likely that the β -W needs to be deposited on certain dielectric layers as well. However, it has also been shown that the choice of underlayer materials can have a significant effect on the crystallographic and transport properties of the films, such as texture, phase transformation and resistivity [DeHaven *et al.*, 1998], and β -W, as a metastable phase, does not form on all underlayer materials, thus it is important to find an appropriate underlayer for obtain β -W phase in thin films and optimize its performance in spintronics.

The deposition of β -W on layers other than SiO_2 can facilitate the study of its spin transport properties. Spin diffusion length is an important spin transport property of β -W, and this parameter characterizes the mean diffusion distance of electrons between spin-flipping collisions [Bass *et al.*, 2007]. Spin diffusion length of β -W can be experimentally determined by depositing β -W onto a soft magnetic layer such as permalloy, then measuring the shape of the microwave absorption spectrum at the ferromagnetic resonance conditions. The shape of the resonant absorption peak changes with respect to that without β -W, because extra microwave energy is absorbed by the precessing moment in the soft magnetic layer and is converted to the spin current dissipated in β -W [Tao *et al.*, 2014, Zhang *et al.*, 2013]. The non-magnetic materials to be studied can be deposited before or after the soft magnetic layer. However, it is critical that the change of spectrum is only caused by the additional dissipation in the β -W film, hence the

deposition conditions of the soft magnetic layers need to be invariant. Since the properties of the soft magnetic layer, such as microstructure, resistivity and magnetic anisotropy, could have different value between films deposited on β -W and on the substrate directly, the soft magnetic films have to be deposited prior to β -W in order to guarantee that its properties are invariant with and without β -W, and this is the experimental configuration in nearly all spin pumping experiments [Tao *et al.*, 2014, Zhang *et al.*, 2014]. In short, the spin diffusion length of β -W can be accurately determined only if β -W can be deposited on soft magnetic layer in a consistent manner. The ferromagnetic resonance measurement of β -W has been conducted using amorphous CoFeB film as the underlayer [Hao *et al.*, 2015], which is not as ideal as the permalloy film because permalloy has low anisotropy field. Therefore, it is important to develop the deposition parameters of β -W films on permalloy underlayer for accurate measurement of its spin diffusion length.

Furthermore, results presented in earlier chapters showed that the formation process of β -W depends critically upon the adsorption of N_2 on its underlayer; therefore, the nature of underlayer is expected to have a significant influence on the formation of β -W. In other words, the deposition of β -W on other underlayers could potentially lead to a better understanding of its formation process and its relationship to the chemistry, structure and gas adsorption of the underlayer materials.

5.2 Experimental Details

The conductive underlayer materials studied were C, Mg, Al, Ti, V, Cr, Mn, Fe, Co, Ni, Cu, Zr, Nb, Mo, Hf, Ta, W, Pt, $Co_{40}Fe_{40}B_{20}$, and permalloy, and these underlayers were deposited by DC magnetron sputtering onto glass substrates. The amorphous ceramic

underlayers included B, Si, Al₂O₃, SiO₂, and these films were deposited by RF magnetron sputtering onto glass substrates. All the depositions were conducted at 2×10^{-8} torr base pressure, and an argon flow at the pressure of 3×10^{-3} torr was used as the sputtering gas. The thicknesses of the underlayers were around 20 nm.

In addition to the amorphous ceramic underlayers, crystalline ceramic underlayers were also used and these underlayers were single-crystal ceramic substrates including MgO, sapphire (Al₂O₃) and quartz (SiO₂). These underlayers were annealed in air at 600°C for 1 hour in order to remove the adsorbed water vapor, then transferred immediately into the deposition chamber. Then they were annealed further at 300°C in the chamber for 1 hour in order to remove the small amount of water vapor adsorbed during the transfer, and cooled to room temperature in the vacuum overnight.

After the preparation of underlayers and substrates, 14 nm tungsten films were deposited at 50W power and 1.4 nm/minute for all underlayers/substrates with the exception of permalloy and Fe_xNi_{1-x}. The deposition rates of tungsten films on Fe-Ni alloy films were varied from 1.4 nm/min to 0.3 nm/minute in order to examine the conditions for the formation of β-W on these underlayers. The base pressure in the chamber for tungsten deposition contained 1.2×10^{-5} torr N₂ and 3mTorr Ar was used as the sputtering gas.

Following the deposition, the phases of tungsten films were examined by X-ray diffraction and electrical resistivity measurement, and were examined only using resistivity measurement for films deposited on single-crystal substrates due to the incompatibility of PANalytical XRD with crystalline substrates.

5.3 Results

5.3.1 Relationship Between Underlayer Materials and β -W Formation

Examples of XRD patterns of W/Cr and W/CoFeB are shown in Figure 5.1, and the figure shows that β -W phase can be stabilized on N_2 on CoFeB but not on Cr underlayer. The resistivity measurement also shows consistent results, as the films containing mainly β -W phase have conductivity of less than $1 \text{ S}/\mu\text{m}$, while those that primarily consist of α -W phase have conductivity of about $4 \text{ S}/\mu\text{m}$. Therefore, the underlayer materials play an important role in the formation of β -W in films deposited with N_2 impurity.

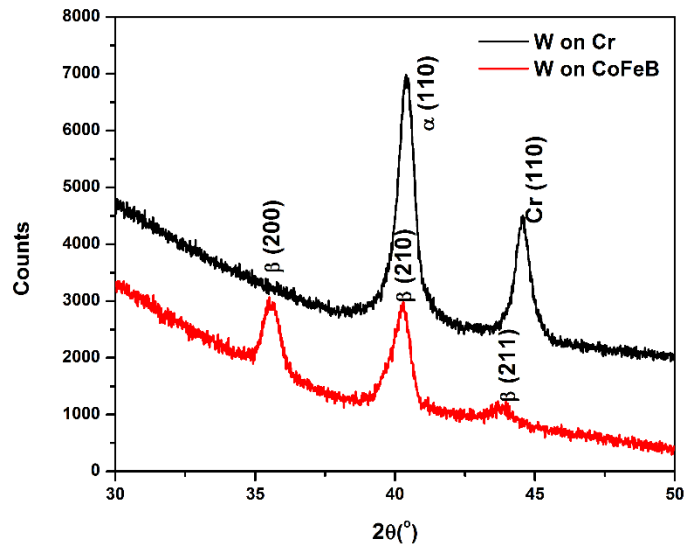


Figure 5.1. XRD patterns of W/Cr and W/CoFeB films on amorphous glass substrates. The W layers were deposited at 1.2×10^{-5} torr of N_2 pressure.

element name	atomic number	symbol	atomic weight
beryllium	4	Be	9.012182
lithium	3	Li	6.941
lithium	19	Li	6.941
sodium	11	Na	22.98977
sodium	11	Na	22.98977
magnesium	12	Mg	24.3050
magnesium	12	Mg	24.3050
potassium	19	K	39.0983
potassium	19	K	39.0983
calcium	20	Ca	40.078
calcium	20	Ca	40.078
scandium	21	Sc	44.95591
scandium	21	Sc	44.95591
titanium	22	Ti	47.867
titanium	22	Ti	47.867
vanadium	23	V	50.9415
vanadium	23	V	50.9415
chromium	24	Cr	51.9961
chromium	24	Cr	51.9961
manganese	25	Mn	54.93805
manganese	25	Mn	54.93805
iron	26	Fe	55.845
iron	26	Fe	55.845
cobalt	27	Co	58.9332
cobalt	27	Co	58.9332
nickel	28	Ni	58.6934
nickel	28	Ni	58.6934
copper	29	Cu	63.546
copper	29	Cu	63.546
zinc	30	Zn	65.409
zinc	30	Zn	65.409
gallium	31	Ga	72.64
gallium	31	Ga	72.64
germanium	32	Ge	72.64
germanium	32	Ge	72.64
arsenic	33	As	74.9216
arsenic	33	As	74.9216
selenium	34	Se	78.96
selenium	34	Se	78.96
bromine	35	Br	79.904
bromine	35	Br	79.904
krypton	36	Kr	83.798
krypton	36	Kr	83.798
rubidium	37	Rb	85.468
rubidium	37	Rb	85.468
strontium	38	Sr	87.62
strontium	38	Sr	87.62
yttrium	39	Y	88.90585
yttrium	39	Y	88.90585
zirconium	40	Zr	91.224
zirconium	40	Zr	91.224
niobium	41	Nb	92.90638
niobium	41	Nb	92.90638
molybdenum	42	Mo	95.94
molybdenum	42	Mo	95.94
technetium	43	Tc	98
technetium	43	Tc	98
ruthenium	44	Ru	101.07
ruthenium	44	Ru	101.07
rhodium	45	Rh	102.9055
rhodium	45	Rh	102.9055
palladium	46	Pd	106.42
palladium	46	Pd	106.42
silver	47	Ag	107.8682
silver	47	Ag	107.8682
cadmium	48	Cd	112.411
cadmium	48	Cd	112.411
indium	49	In	114.818
indium	49	In	114.818
tin	50	Sn	118.710
tin	50	Sn	118.710
antimony	51	Sb	121.760
antimony	51	Sb	121.760
tellurium	52	Te	127.60
tellurium	52	Te	127.60
iodine	53	I	126.9045
iodine	53	I	126.9045
xenon	54	Xe	131.293
xenon	54	Xe	131.293
barium	56	Ba	137.327
barium	56	Ba	137.327
lanthanum	57	La	138.90545
lanthanum	57	La	138.90545
cesium	55	Cs	132.90545
cesium	55	Cs	132.90545
thorium	90	Th	232.0377
thorium	90	Th	232.0377
protactinium	91	Pa	231.03688
protactinium	91	Pa	231.03688
uranium	92	U	238.02891
uranium	92	U	238.02891
neptunium	93	Np	237.04817
neptunium	93	Np	237.04817
plutonium	94	Pu	244.06422
plutonium	94	Pu	244.06422
americium	95	Am	243.06138
americium	95	Am	243.06138
curium	96	Cm	247.07035
curium	96	Cm	247.07035
berkelium	97	Bk	247.07035
berkelium	97	Bk	247.07035
californium	98	Cf	251.0832
californium	98	Cf	251.0832
einsteinium	99	Es	252.0832
einsteinium	99	Es	252.0832
fermium	100	Fm	257.1035
fermium	100	Fm	257.1035
mendelevium	101	Md	258.1035
mendelevium	101	Md	258.1035
nobelium	102	Nb	259.1035
nobelium	102	Nb	259.1035
lawrencium	103	Lr	262.1035
lawrencium	103	Lr	262.1035
bohrium	104	Bh	264.1035
bohrium	104	Bh	264.1035
hassium	105	Hs	277.1035
hassium	105	Hs	277.1035
meitnerium	106	Mt	288.1035
meitnerium	106	Mt	288.1035
darmstadtium	107	Ds	289.1035
darmstadtium	107	Ds	289.1035
roentgenium	108	Rg	290.1035
roentgenium	108	Rg	290.1035
copernicium	109	Cn	285.1035
copernicium	109	Cn	285.1035
nihonium	110	Nh	286.1035
nihonium	110	Nh	286.1035
flerovium	111	Fl	289.1035
flerovium	111	Fl	289.1035
tennessium	112	Ts	289.1035
tennessium	112	Ts	289.1035
oganeson	114	Og	289.1035
oganeson	114	Og	289.1035
livermorium	116	Lv	289.1035
livermorium	116	Lv	289.1035
tennessium	115	Ts	289.1035
tennessium	115	Ts	289.1035
copernicium	112	Cn	285.1035
copernicium	112	Cn	285.1035
bohrium	107	Bh	264.1035
bohrium	107	Bh	264.1035
hassium	108	Hs	289.1035
hassium	108	Hs	289.1035
meitnerium	109	Mt	288.1035
meitnerium	109	Mt	288.1035
darmstadtium	110	Ds	289.1035
darmstadtium	110	Ds	289.1035
roentgenium	111	Rg	290.1035
roentgenium	111	Rg	290.1035
copernicium	112	Cn	285.1035
copernicium	112	Cn	285.1035
nihonium	113	Nh	286.1035
nihonium	113	Nh	286.1035
flerovium	114	Fl	289.1035
flerovium	114	Fl	289.1035
tennessium	115	Ts	289.1035
tennessium	115	Ts	289.1035
oganeson	116	Og	289.1035
oganeson	116	Og	289.1035
livermorium	117	Lv	289.1035
livermorium	117	Lv	289.1035
tennessium	115	Ts	289.1035
tennessium	115	Ts	289.1035
copernicium	112	Cn	285.1035
copernicium	112	Cn	285.1035
bohrium	107	Bh	264.1035
bohrium	107	Bh	264.1035
hassium	108	Hs	289.1035
hassium	108	Hs	289.1035
meitnerium	109	Mt	288.1035
meitnerium	109	Mt	288.1035
darmstadtium	110	Ds	289.1035
darmstadtium	110	Ds	289.1035
roentgenium	111	Rg	290.1035
roentgenium	111	Rg	290.1035
copernicium	112	Cn	285.1035
copernicium	112	Cn	285.1035
nihonium	113	Nh	286.1035
nihonium	113	Nh	286.1035
flerovium	114	Fl	289.1035
flerovium	114	Fl	289.1035
tennessium	115	Ts	289.1035
tennessium	115	Ts	289.1035
oganeson	116	Og	289.1035
oganeson	116	Og	289.1035
livermorium	117	Lv	289.1035
livermorium	117	Lv	289.1035
tennessium	115	Ts	289.1035
tennessium	115	Ts	289.1035
copernicium	112	Cn	285.1035
copernicium	112	Cn	285.1035
bohrium	107	Bh	264.1035
bohrium	107	Bh	264.1035
hassium	108	Hs	289.1035
hassium	108	Hs	289.1035
meitnerium	109	Mt	288.1035
meitnerium	109	Mt	288.1035
darmstadtium	110	Ds	289.1035
darmstadtium	110	Ds	289.1035
roentgenium	111	Rg	290.1035
roentgenium	111	Rg	290.1035
copernicium	112	Cn	285.1035
copernicium	112	Cn	285.1035
nihonium	113	Nh	286.1035
nihonium	113	Nh	286.1035
flerovium	114	Fl	289.1035
flerovium	114	Fl	289.1035
tennessium	115	Ts	289.1035
tennessium	115	Ts	289.1035
oganeson	116	Og	289.1035
oganeson	116	Og	289.1035
livermorium	117	Lv	289.1035
livermorium	117	Lv	289.1035
tennessium	115	Ts	289.1035
tennessium	115	Ts	289.1035
copernicium	112	Cn	285.1035
copernicium	112	Cn	285.1035
bohrium	107	Bh	264.1035
bohrium	107	Bh	264.1035
hassium	108	Hs	289.1035
hassium	108	Hs	289.1035
meitnerium	109	Mt	288.1035
meitnerium	109	Mt	288.1035
darmstadtium	110	Ds	289.1035
darmstadtium	110	Ds	289.1035
roentgenium	111	Rg	290.1035
roentgenium	111	Rg	290.1035
copernicium	112	Cn	285.1035
copernicium	112	Cn	285.1035
nihonium	113	Nh	286.1035
nihonium	113	Nh	286.1035
flerovium	114	Fl	289.1035
flerovium	114	Fl	289.1035
tennessium	115	Ts	289.1035
tennessium	115	Ts	289.1035
oganeson	116	Og	289.1035
oganeson	116	Og	289.1035
livermorium	117	Lv	289.1035
livermorium	117	Lv	289.1035
tennessium	115	Ts	289.1035
tennessium	115	Ts	289.1035
copernicium	112	Cn	285.1035
copernicium	112	Cn	285.1035
bohrium	107	Bh	264.1035
bohrium	107	Bh	264.1035
hassium	108	Hs	289.1035
hassium	108	Hs	289.1035
meitnerium	109	Mt	288.1035
meitnerium	109	Mt	288.1035
darmstadtium	110	Ds	289.1035
darmstadtium	110	Ds	289.1035
roentgenium	111	Rg	290.1035
roentgenium	111	Rg	290.1035
copernicium	112	Cn	285.1035
copernicium	112	Cn	285.1035
nihonium	113	Nh	286.1035
nihonium	113	Nh	286.1035
flerovium	114	Fl	289.1035
flerovium	114	Fl	289.1035
tennessium	115	Ts	289.1035
tennessium	115	Ts	289.1035
oganeson	116	Og	289.1035
oganeson	116	Og	289.1035
livermorium	117	Lv	289.1035
livermorium	117	Lv	289.1035
tennessium	115	Ts	289.1035
tennessium	115	Ts	289.1035
copernicium	112	Cn	285.1035
copernicium	112	Cn	285.1035
bohrium	107	Bh	264.1035
bohrium	107	Bh	264.1035
hassium	108	Hs	289.1035
hassium	108	Hs	289.1035
meitnerium	109	Mt	288.1035
meitnerium	109	Mt	288.1035
darmstadtium	110	Ds	289.1035
darmstadtium	110	Ds	289.1035
roentgenium	111	Rg	290.1035
roentgenium	111	Rg	290.1035
copernicium	112	Cn	285.1035
copernicium	112	Cn	285.1035
nihonium	113	Nh	286.1035
nihonium	113	Nh	286.1035
flerovium	114	Fl	289.1035
flerovium	114	Fl	289.1035
tennessium	115	Ts	289.1035
tennessium	115	Ts	289.1035
oganeson	116	Og	289.1035
oganeson	116	Og	289.1035
livermorium	117	Lv	289.1035
livermorium	117	Lv	289.1035
tennessium	115	Ts	289.1035
tennessium	115	Ts	289.1035
copernicium	112	Cn	285.1035
copernicium	112	Cn	285.1035
bohrium	107	Bh	264.1035
bohrium	107	Bh	264.1035
hassium	108	Hs	289.1035
hassium	108	Hs	289.1035
meitnerium	109	Mt	288.1035
meitnerium	109	Mt	288.1035
darmstadtium	110	Ds	289.1035
darmstadtium	110	Ds	289.1035
roentgenium	111	Rg	290.1035
roentgenium	111	Rg	290.1035
copernicium	112	Cn	285.1035
copernicium	112	Cn	285.1035
nihonium	113	Nh	286.1035
nihonium	113	Nh	286.1035
flerovium	114	Fl	289.1035
flerovium	114	Fl	289.1035
tennessium	115	Ts	289.1035
tennessium	115	Ts	289.1035
oganeson	116	Og	289.1035

The relationship between the β -W phase formation in tungsten films and the underlayer materials is shown in Figure 5.2. β -W phase was detected in underlayers highlighted in green, while only α -W phase was found in those highlighted in orange. Note that although β -W was found with Ni underlayers, the tungsten film contain primarily α -W phase, as shown in the XRD pattern of tungsten on Ni in Figure 5.3.

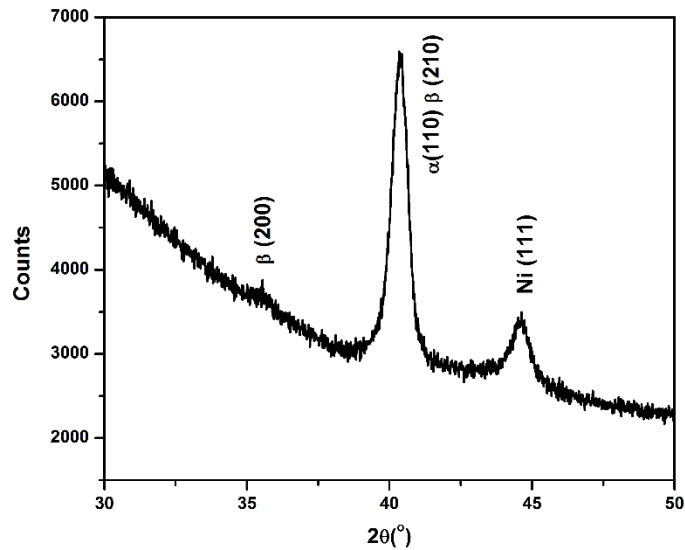


Figure 5.3. The XRD pattern of tungsten film on Ni underlayer. The tungsten film was deposited at 1.2×10^{-5} torr N_2 .

5.3.2 Deposition of β -W on Permalloy Underlayer

Since a small volume fraction of β -W on Ni has been achieved, the deposition conditions need to be optimized for obtaining β -W thin films. In chapter 4 it was shown that lower substrate temperatures, higher N_2 partial pressure and lower deposition power are favorable for the

formation of β -W. Since the deposition is conducted at room temperature and no liquid nitrogen cooling is available for the equipment used in the current work, it is difficult to get the substrate temperature lower than room temperature. On the other hand, increasing the N_2 pressure also has the risk of amorphizing the tungsten films or forming tungsten nitride, and these undesirable phases are difficult to detect as they do not give rise to any peak in XRD. Therefore, lowering the deposition power is the only method to obtain higher volume fraction of β -W in the thin films in the current studies.

The XRD pattern of tungsten films deposited on permalloy at 50W and 10W at a pressure of 1.2×10^{-5} torr N_2 is shown in Figure 5.4. The plot shows that although the films deposited at

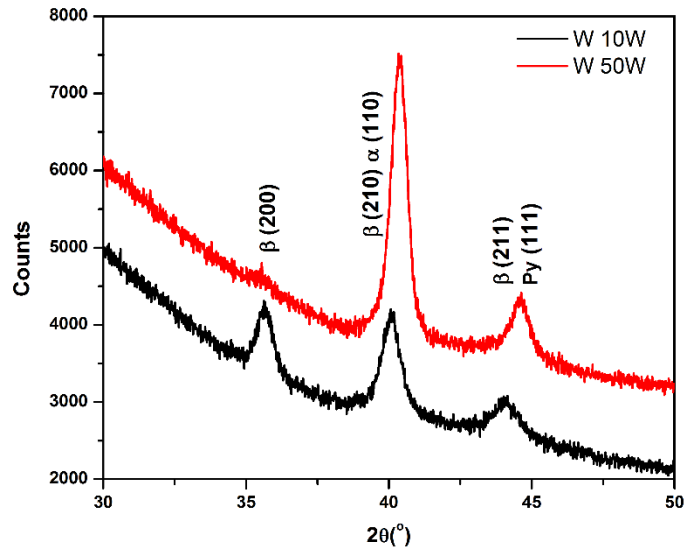


Figure 5.4. The XRD pattern of tungsten films deposited at 50W and 10W on permalloy underlayers with 1.2×10^{-5} torr N_2 .

50W only exhibit small peaks associated with β -W, the intensity of these peaks is greatly increased for films deposited at 10W. By comparing the peak intensity with those deposited directly on SiO₂ layers, the films deposited at 10W should contain only β -W phase.

In order for the measurement of spin diffusion length by ferromagnetic resonance, other functional layers are needed to make the full structure. The full structure (from bottom to top) comprises 5nm Ta layer as the adhesion layer, 5nm Cu layer as spacer between permalloy and Ta, 5nm permalloy responsible for the absorption of microwave signals in ferromagnetic

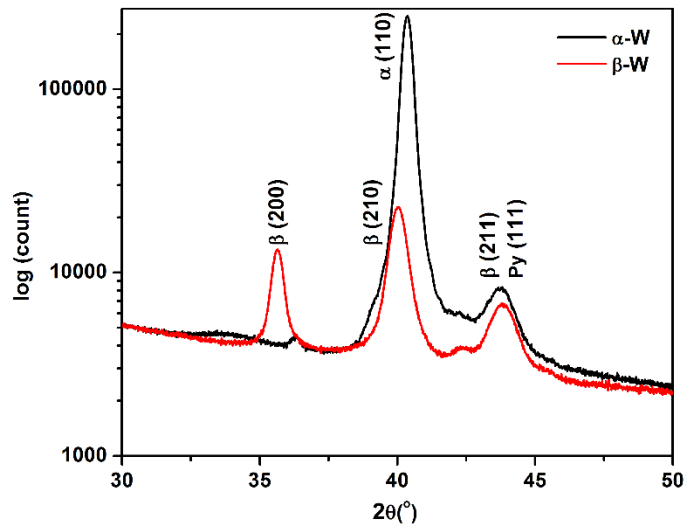


Figure 5.5. The XRD pattern of Ta 5nm/Cu 5nm/permalloy 5nm/W 30nm/Cu 5nm/Ta 5nm structure used for the ferromagnetic resonance measurement.

resonance experiments, 30nm α/β -W films which contribute to the enhancement of damping as a result of spin pumping, another 5nm Cu layer as spacer between W and the top Ta layer, and

another 5nm Ta layer as the cap layer against oxidation. The corresponding XRD patterns are shown in Figure 5.5. The tungsten films deposited without N₂ contains only α -W, while those deposited using N₂ contains mostly β -W. The ferromagnetic resonance measurement of the above full structures is ongoing by Wei Cao in Professor William Bailey's group at Columbia University.

5.4 Discussion

5.4.1 Effect of Underlayer Crystalline Structure

The deposition of α -Ta and β -Ta is more extensively studied than β -W, and it has been shown that the formation of low-resistivity α -Ta also has a strong dependence on the underlayer/substrate materials, hence the concepts about the influence of underlayers on the formation of β -Ta can be adapted for the study of β -W. The β -Ta phase forms on most of the underlayer materials [Clevenger *et al.*, 1992, Hieber *et al.*, 1982, Jiang *et al.*, 1993], except that α -Ta phase dominates for films deposited on underlayers including Cu [Koyano *et al.*, 1993], Al [Hoogeveen *et al.*, 1996], Nb [Face *et al.*, 1987, Morohashi 1995] and Ta₂N [Stavrev *et al.*, 1999]. The origin of the stability of α -W phase on these underlayers is usually attributed to the small lattice mismatch between α -Ta and the surface of the underlayers, which favors the formation of α -Ta by minimizing the strain energy in the system [Face *et al.*, 1987, Morohashi 1995, Stavrev *et al.*, 1999].

The crystallographic structure of the underlayers and the phase formation in tungsten thin films is summarized in Table 5.1, in order to illustrate the effect of lattice structure of underlayers. The table shows that β -W can readily form on all amorphous underlayers including SiO₂, B, C, amorphous Si, Al₂O₃ and CoFeB, whereas only α -W was observed in films deposited

on metal underlayers regardless of their crystallographic structure. On the other hand, β -W phase can also form on crystalline substrates including Si, quartz and sapphire, as well as their corresponding amorphous underlayers or substrates. Therefore, whether β -W phase formation will occur cannot be predicted by the crystalline structure of the underlayers.

5.4.2 Effect of Underlayer Chemistry

The underlayer dependence of phase formation in β -Ta was also explained by the surface chemistry of underlayers [Feinstein *et al.*, 1973, Senkevich *et al.*, 2006]. It has been shown that the effect of underlayer materials can be classified into three categories [Feinstein *et al.*, 1973]:

1. On oxides and substrates that could readily form surface oxide in air at room temperatures such as Cu, β -Ta formed in the tantalum films;
2. On oxidation-resistant underlayers such as Au, α -Ta formed in the films;
3. On underlayers that did not form an oxide at room temperature but could be oxidized at elevated temperatures such as Ta₂N, α -Ta formed on the clean underlayers while β -Ta formed when the underlayer was oxidized at high temperatures.

Therefore, the presence of oxygen element on the surface of the underlayers could be indispensable for the formation of β -Ta phase. This conclusion was further supported by the observation of phase formation in tantalum films deposited on polymer underlayers [Senkevich *et al.*, 2006]. The polymer underlayers, including porous methyl silsesquioxane (MSQ), parylene-N (Pa-N) caulked porous MSQ, benzocyclobutene (BCB), and SiLK layers, all have the amorphous structures, but α -Ta was observed on Pa-N caulked porous MSQ, BCB and SiLK underlayers which are all hydrocarbon based, while β -Ta formed on porous MSQ underlayer that is oxygen rich. Therefore, the presence of oxygen, especially in the absence of a crystalline structure, could play an important role in determining the phase formation in tantalum thin films.

Table 5.1. Relationship between crystallographic structure of the underlayers and the phase formation in tungsten thin films.

Underlayer	Atomic Number	Structure	Lattice Constant (Å)	W Phase
V	23	bcc	3.03	α
Cr	24	bcc	2.91	α
Mn	25	bcc	8.91	α
Fe	26	bcc	2.87	α
Nb	41	bcc	3.30	α
Mo	42	bcc	3.15	α
Ta	73	bcc	3.30	α
α -W	74	bcc	3.17	α
Al	13	fcc	4.05	α
Cu	29	fcc	3.61	α
Pt	78	fcc	3.92	α
Mg	12	hcp	3.21, 5.21	α
Ti	22	hcp	2.95, 4.69	α
Zr	23	hcp	3.23, 5.14	α
Co	27	hcp	2.51, 4.07	α
B	5	amorphous	NA	β
C	6	amorphous	NA	β
Si [Lee <i>et al.</i> , 2016]	14	amorphous	NA	β
Si	14	Fd-3m	5.43	β
Al ₂ O ₃	NA	amorphous	NA	β
Al ₂ O ₃ (sapphire)	NA	R3c	4.76, 13.0	β
SiO ₂	NA	amorphous	NA	β
SiO ₂ (quartz)	NA	P6 ₂ 22	4.91, 5.40	β
CoFeB	NA	amorphous	NA	β
Ni	28	fcc	3.52	$\alpha+\beta$

The situation in tungsten thin films is more complicated than that in tantalum, as β -W could also form on clean CoFeB, B, C and Si underlayers which do not contain oxygen atoms. On the other hand, it is observed that these underlayers all contain certain amount of non-metal elements other than oxygen, while those only permitting the formation of α -W contain only metallic elements. Therefore, the necessity of oxygen for the formation of β -Ta can be generalized into the requirement of any non-metal elements in the underlayers for β -W, potentially above a critical concentration.

The requirement for the existence of non-metal elements in the underlayers can be qualitatively understood by the strong covalent bonds associated with these elements. Although α -W is a metal, it contains a mixture of covalent and metallic bonds, as a result of the ground state electronic configuration of bcc W with d^5s^1 instead of d^4s^2 in free tungsten atoms calculated from local spin density theory [Zunger *et al.*, 1979]. The covalent bonds in α -W originate from the localization of the 5d orbital electrons, while the metallic bonds in α -W come from the s electrons which are delocalized and shared among all atoms [Lassner *et al.*, 1999]. On the other hand, there have been studies on the electronic structure of compounds with A15 (β -W) structure and A_3B composition, such as V_3Si , in order to determine the nature of superconductivity in A_3B structured compounds [Wang 1973, Chiu *et al.*, 1982], and β -W can be viewed as a special example of the A_3B compounds with A and B are both tungsten atoms. The studies showed that [Wang 1973, Chiu *et al.*, 1982] there exist chains of covalent bonds in in A15 structured materials which are responsible for their superconducting behavior. Therefore, it is likely that the density of covalent bonds are important for the relative stability of α -W and β -W phase, and the covalent bonds in the underlayers could play an essential role at the initial stage of deposition in assisting the nucleation the β -W phase.

5.5 Summary

The multilayer structure for spin diffusion length measurement of β -W on permalloy layer was deposited by reducing the deposition power to 10W. The relationship between the underlayer materials and the formation of β -W was investigated by X-ray diffraction and resistivity measurement, and the results show that β -W could only form on underlayers containing non-metal elements. The principle of the classification could be explained by the requirement for the presence of covalent bonds in the underlayers, which could assist the nucleation of β -W phase by fulfilling the requirement of strong covalent bonds at the initial stage.

6 – Formation of (002) Textured Permalloy on β -W

6.1 Motivation

The special interaction between Ni and β -W has been shown by the unique capability of Ni and permalloy underlayers to allow the formation of β -W on their surface among all metallic crystalline underlayer in the previous chapter. In addition, as will be shown in this chapter, the special interaction between Ni and β -W could lead to the formation of (002) texture in permalloy thin film deposited on β -W underlayer.

For many applications of metallic thin films, the out-of-plane orientation of the films are important, in order to optimize the properties of the films which are mostly anisotropic. The (002) textured films with bcc or fcc structures are desirable, since the electronic and magnetic properties are often optimum along this direction. $L1_0$ FePt can be regarded as a special case of the fcc structure and it is the material used in heat-assisted magnetic recording technology [Gage *et al.*, 2016]. As the direction of writing field is perpendicular to the surface of the films for heat-assisted magnetic recording technology, the easy axis has to be oriented out-of-plane. Since the easy axis is parallel to the (001) orientation of $L1_0$ FePt due to its magnetocrystalline anisotropy, the $L1_0$ FePt has to adopt an (001) texture as magnetic recording media [Chen *et al.*, 2008]. Most of the studies on the formation of (001) textured $L1_0$ FePt involve the use of (002) oriented MgO substrate, which is too expensive for product manufacturing compared with the amorphous glass substrates used in hard drives. MgO underlayers deposited by RF sputtering are also used as the seed layer, but the deposition of MgO suffers from the problems of particle contamination and low yield. Therefore, it is beneficial to have the capability to deposit (002) textured metallic

films on amorphous substrates, which can also serve as the seed layer for obtaining the (001) texture in the films deposited on top.

There have been extensive studies in obtaining (002) texture in metal thin films deposited on amorphous substrates, and the most widely used recipe involves the deposition of (002) textured Cr films onto glass substrate with substrate temperature at about 300°C [Feng *et al.*, 1994, Duan *et al.*, 1990, Lee 1985, Pressesky *et al.*, 1991, Ravipati *et al.*, 1987]. However, the deposition process suffers from the disadvantage that it is not compatible with materials that are heat sensitive, such as the photoresist used in the process of lift-off patterning or with multilayer films that can easily interdiffuse into adjacent layers at elevated temperatures. In addition, it is difficult to deposit high quality Cr films. Therefore, the capability of depositing (002) textured metal thin films on amorphous substrates at room temperature could be beneficial in many applications in electronics and spintronics.

6.2 Experimental Details

The 14 nm β -W thin films were deposited by DC magnetron sputtering onto glass substrates at 1.2×10^{-5} torr N_2 at room temperature, and the deposition power was kept at 50W. Then the permalloy films were deposited from an alloy target with the composition of 81at% Ni-19at% Fe, and the Ni-Fe alloy films were deposited by DC magnetron sputtering at room temperature from the elemental targets with two sputter guns, and the composition of the films were adjusted by controlling the relative deposition rates of Ni and Fe atoms.

Following the deposition, the out-of-plane texture of the Ni-Fe films was examined by PANalytical XRD using θ - 2θ scan. The β -W/permalloy bilayer film was prepared as a cross-

sectional TEM specimen at Evans Analytical Group. The TEM specimen was examined using the Talos F200X TEM manufactured by FEI company. Prior to observation, the specimen was tilted using the double-tilt TEM holder so that the orientation of electron beam was along the [110] zone axis of the Si substrate. Then the dark field images and electron diffraction patterns were recorded using charge-coupled device camera of the TEM at 200kV.

6.3 Results

6.3.1 Formation of (002) Textured Permalloy on β -W

The XRD pattern of permalloy deposited on β -W is shown in Figure 6.1. The strong (002) peak and the absence of other peaks indicate that the permalloy is (002) textured. In contrast, permalloy films deposited on most underlayers usually exhibit (111) texture since the (111) plane of fcc metals and alloys has the lowest surface energy. Therefore, the presence of β -W underlayer is responsible for the generation of (002) texture in permalloy thin films.

The electron diffraction pattern of the cross-sectional TEM specimen is shown in Figure 6.2. The regular array of spots are from the silicon substrate. The diffraction pattern of β -W forms rings due to its polycrystalline nature. The diffraction pattern of permalloy contains only (002) spots, consistent with the (002) texture observed in XRD patterns. The diffraction spots form short arcs instead of continuous rings due to the presence of texture in the permalloy layer, and the small angle of arc indicates the strong degree of texture in the permalloy layer.

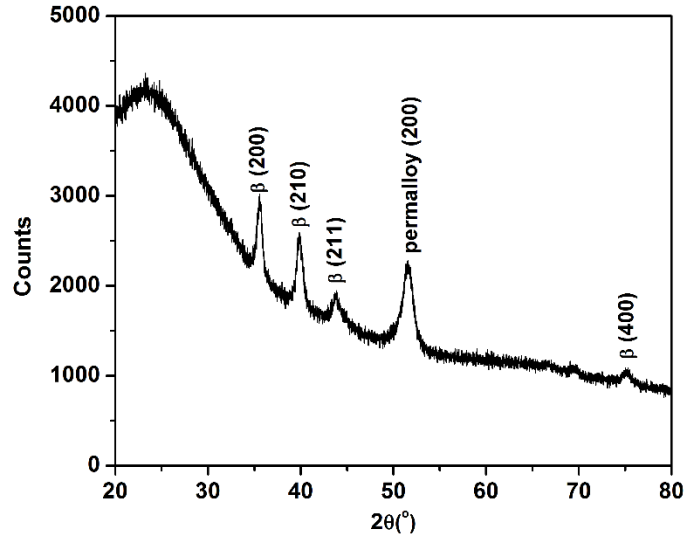


Figure 6.1. The XRD pattern of permalloy films deposited on 14nm β -W.

The dark field image of the cross-sectional sample is shown in Figure 6.3. The objective aperture was positioned so that only grains contributing to the (002) reflection of permalloy appear as bright in the figure. Figure 6.3 shows nearly all the grains appear as bright, hence the presence of the strong (002) texture in permalloy films is supported by the dark-field image.

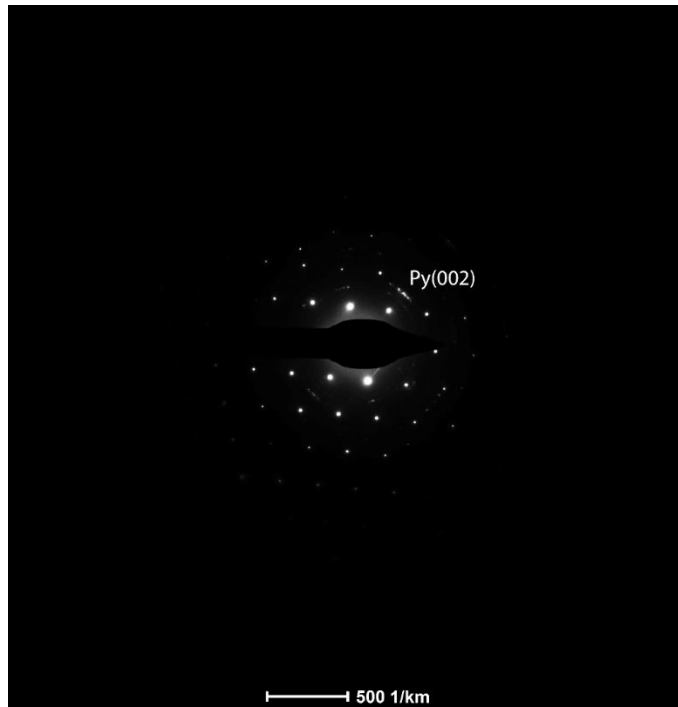


Figure 6.2. The selected area electron diffraction pattern of cross-sectional permalloy/ β -W specimen.

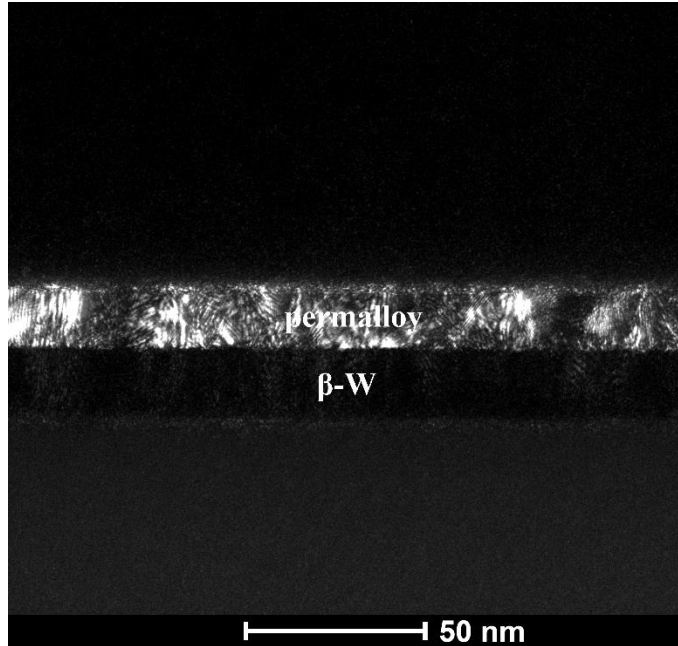


Figure 6.3. The dark field image of permalloy grains with (002) orientation.

6.3.2 The Limitation of (002) Texture Formation

The formation of (002) texture of Ni-Fe alloy on β -W has only a small processing window. Figure 6.4 shows the XRD pattern of Ni-Fe alloy thin films deposited on β -W with different composition. The degree of (002) texture can be estimated from the relative intensity of (002) and (111) diffraction peaks. The (002) texture is strongest at the composition range between 14~20 at% Fe, and becomes weaker on the two sides with too much or too little Fe. In addition, the degree of (002) texture is also dependent upon the thickness of the permalloy films, as it is only found in films thinner than 20 nm, and the texture decreases when the film thickness is larger.

It is worth noting that other bcc or fcc structured metal films, including Cu, Pt, V, Cr, Mn, Fe, Nb, Mo, Ta, W, and Al, were also deposited on β -W and their texture were measured by XRD using θ - 2θ scan. None of the above films exhibit (002) texture or even an enhancement in the degree of (002) texture compared with those deposited on glass substrates. Therefore, the formation of (002) textured permalloy films on β -W is in fact a very special case among all materials that were studied in this work, possibly due to the special interaction between nickel and β -W.

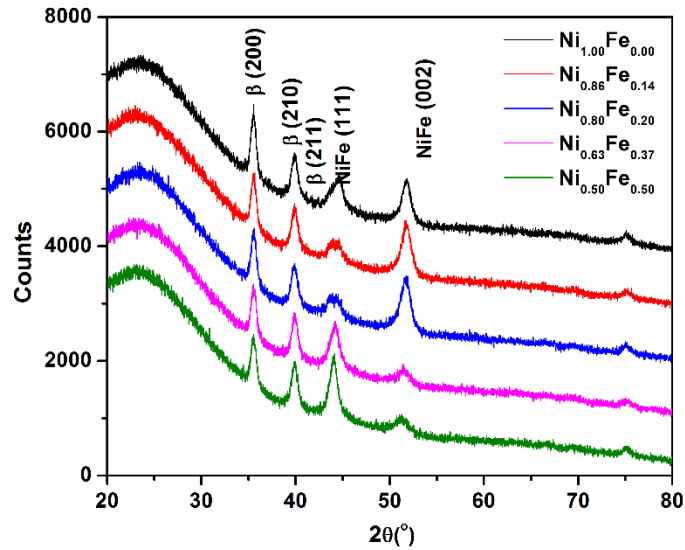


Figure 6.4. The XRD pattern of the out-of-plane texture of Ni-Fe alloy thin films deposited on β -W thin films.

6.4 Discussion

6.4.1 Lattice Mismatch Model for (002) Texture Formation

In most cases, the origin of the texture in thin films can be attributed to the effect of lattice mismatch between the film and the underlayer in the context of epitaxial growth [Freund *et al.*, 2009]. When both layers are crystalline, the misfit strain is expressed in equation 6-1 as

$$\varepsilon = \frac{a_{film} - a_{substrate}}{a_{substrate}} \quad (6-1)$$

where a_{film} , $a_{substrate}$ are the in-plane lattice constant of the film and substrate respectively. In order to minimize the strain energy, the orientation of the films is adjusted so that the lattice mismatch is minimized, hence the out-of-plane texture is determined by the orientation of the surface with the smallest lattice mismatch. In β -W/permalloy bilayer system, the lattice constant of permalloy and β -W along (001) direction is 0.35nm and 0.5 nm respectively. Therefore, the spacing between (001) planes in permalloy is very close to that between (110) planes of β -W. Therefore, the epitaxial relationship of (001) permalloy // (110) β -W is able to create the (002) textured permalloy thin films.

On the other hand, the mechanism of lattice mismatch requires a definite orientation of the underlayers, since there is a one-to-one correspondence between the orientation of the underlayer and that of the film [Freund *et al.*, 2009]. However, the XRD pattern in Figure 6.1 shows that the β -W underlayer has a random orientation, as (220), (210) and (211) peaks are observed in θ - 2θ scan. In addition, for (210) and (211) oriented β -W grains, the (110) reciprocal vector cannot lie in the plane. Therefore, the lattice mismatch model cannot be used to explain the formation of (002) texture permalloy on β -W.

6.4.2 Surface Energy Model for (002) Texture Formation

As β -W has extremely small grain size and the orientation of the grains is random, it is appropriate to consider β -W as an amorphous material with short-range order. From this perspective, a model for explaining the texture formation without resorting to the crystalline structures is more appropriate. The (002) texture in Cr films deposited on amorphous glass substrate [Feng *et al.*, 1994] has been explained by the minimization of total surface and interface energy, and this explanation does not require crystalline structure from the underlayers or the films. Therefore, this model is evaluated here for the explanation of (002) texture in permalloy films deposited on β -W underlayer.

During the initial stage of deposition at small thicknesses, a discontinuous layer consisting of individual islands nucleates instead of a continuous film. If the islands are thermodynamically stable, then their shape and orientation are determined by the minimization of the total surface and interfacial energy [Winterbottom 1967, Cahn *et al.*, 1988]. For permalloy with fcc lattice structure, the (111) surface is usually the one with the lowest surface energy. Therefore, the equilibrium shape of the islands will have the area of (111) surfaces maximized in order to minimize the total surface energy, and the corresponding scheme is shown in Figure 6.5. γ_{12} is the interfacial energy between two layers, and it can be the interfacial energy between β -W and either the (002) or (111) surface of permalloy determined by the texture of permalloy, and γ_2 is the surface energy of the underlayer. The shape of the islands is controlled by the ratio of the two surface energy. When the value of γ_{12} / γ_2 is small, the islands become short and wide so that more of the underlayer is covered by the film. On the other hand, in the case where γ_{12} / γ_2 is

large, by Winterbottom's construction [Winterbottom 1967] the islands become more equiaxed [Feng *et al.*, 1994]. For fcc structured films, as the films tend to maximize the area of the surfaces with the lowest surface energy, the (111) surfaces should be oriented parallel to the surface for short and wide islands, resulting into the (111) texture of the films. On the other hand, as the side surfaces of the equiaxed islands take the largest portion of the total area, the (111) surfaces should be located at the sides of the equiaxed islands, resulting in the (002) texture of the films. In conclusion, the fcc structured films have (002) texture when the value of γ_{12} / γ_2 is large and equiaxed grains are formed.

The large value of γ_{12} / γ_2 in β -W/permalloy system can be achieved with a large β -W – permalloy interface energy and small β -W surface energy. The calculated surface energy of the elemental metals is shown in Table 6.1 [Tyson *et al.*, 1977], and the results show that α -W has the highest surface energy among all elemental metals. On the other hand, the surface energy of β -W is likely to be equal or higher than that of α -W, due to the existence of stronger covalent bond in β -W. Therefore, it is unlikely that β -W can have a small surface energy. On the other hand, the interface energy between β -W and permalloy is not expected to be much larger than that between other amorphous underlayers and permalloy. Therefore, instead of a small γ_{12} / γ_2 , its value in β -W/permalloy bilayer should in fact be larger, hence (111) textured films are predicted instead of (002) texture, in contradiction to the experimental observations.

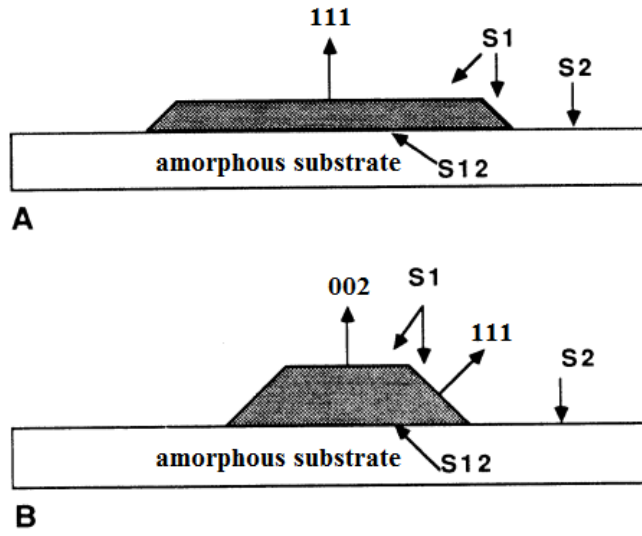


Figure 6.5. The shape of islands in fcc structured films to maximize the area of the (111) surfaces by forming (A) (111) texture and (B) (002) texture [Feng *et al.*, 1994].

Table 6.1. Surface energy of elemental metals [Tyson *et al.*, 1977].

Metal	Structure	Surface	Surface Energy (J m ⁻²)
Pb	fcc	(111)	0.593
Al	fcc	(111)	1.143
Ag	fcc	(111)	1.246
Au	fcc	(111)	1.506
Mn	fcc	(111)	1.543
Cu	fcc	(111)	1.790
Pd	fcc	(111)	2.003
Cr	bcc	(110)	2.354
Ni	fcc	(111)	2.380
Fe	bcc	(110)	2.417
Pt	fcc	(111)	2.489
V	bcc	(110)	2.622
Nb	bcc	(110)	2.655
Rh	fcc	(111)	2.659
Ta	bcc	(110)	2.902
Mo	bcc	(110)	2.907
Ir	fcc	(111)	3.048
W	bcc	(110)	3.265

There are other discrepancies between the model and the formation of (002) textured permalloy on β -W. According to the theory, after the initial stage where the (002) texture is developed at large value of γ_{12} / γ_2 , the (002) texture will gradually transition into the (111) texture for fcc structured films when the individual islands impinges with each other and coalescence into larger grains. Now that the surface area of the side of the grains becomes negligible compared with that of the top surface, the top surface should take the (111) orientation in order to minimize the total energy, thus (111) texture will be developed in thick films. This transition of texture in the model at the coalescence stage could explain the observation that (111) texture is observed for films at larger than 50 nm thickness. On the other hand, in order to

keep the transition into (111) texture from occurring, the films need to have large grain sizes, so that the distance between the grains is large which could effectively delay the onset of coalescence stage [Feng *et al.*, 1994]. However, the situation in permalloy is exactly the opposite, as permalloy has a grain size of about 10 nm which is smaller than most of the metal thin films. Therefore, the underlying assumptions of the surface energy model for (002) texture formation is in contradiction to the observation in permalloy/ β -W bilayers.

6.4.2 Structure Zone Model for (002) Texture Formation

Films deposited at different temperatures could have significantly different morphology and microstructure, and the relationship between temperature and film structure is expressed by the structure zone model. The structure zone model uses a single parameter, the reduced temperature as T_s / T_m , to separate the deposition conditions into different regions. There has been no consensus on the exact value of the boundaries, and several classifications are shown in Figure 6.6 [Wang *et al.*, 2014, Movchan *et al.*, 1969, Thornton 1974, Messier *et al.*, 1984]. As the deposition takes place at room temperature and the melting point of permalloy is about 1748K, the reduced temperature for permalloy deposition is 0.17. Therefore, the deposition of permalloy is likely to be in Zone I or Zone T. For films deposited in Zone I, because of the lack of grain boundary mobility during the growth of films, the films either adopt a random polycrystalline texture or become amorphous [Wang *et al.*, 2014], in contrary to the observation of (002) texture in permalloy films, thus only the mechanism for texture formation in Zone T need to be considered.

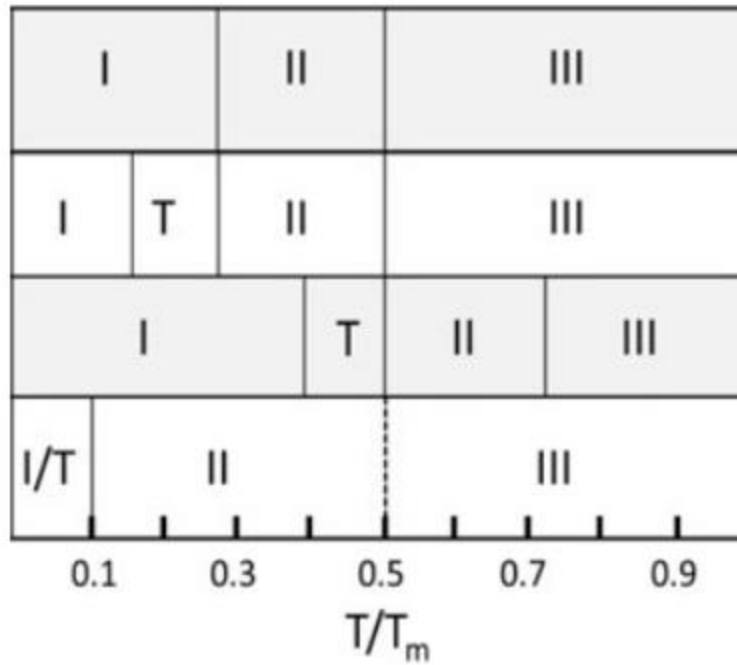


Figure 6.6. The classification of deposition parameters in structure zone model [Wang *et al.*, 2014].

In Zone T, the mobility of surface atoms is usually high enough for the growth of grains according to their kinetically determined crystal habit, while their mobility is not high enough for grain boundary migration and recrystallization. Since different surfaces grow at different rates, faceted grains will be observed with the orientation of the facets being those with the slowest growth rate. The surface with the slowest growth rate is usually the one with the smallest number of nearest neighbors offered to the adatoms originating from the sputtering process, hence fcc structured materials should have (111) as the slowest growing planes. Therefore, the grains will

have an orientation the same as the equiaxed grains in the surface energy model, except the orientation is determined by the reduced temperature instead of surface energy.

According to the structure zone model, the initial faceted nuclei can have random orientation. The nuclei grow into different height which is determined by the relative growth rates of their orientations before impingement. At the stage when the grains collide with each other and grain boundaries are created, no diffusion across the grain boundaries could occur due to the lack of energy in Zone T. However, the nuclei with (002) orientation with a faster growth rate could overgrow the adjacent (111) oriented nuclei, which will be gradually enveloped as shown in the schematic diagram in Figure 6.7. Eventually, all the grains that are not enveloped by other grains will have (002) out-of-plane orientation.

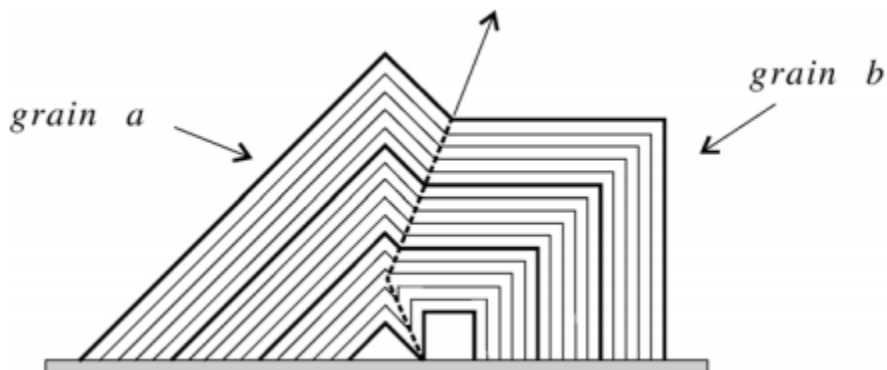


Figure 6.7. The schematic diagram of the process in which the fast growing grains shown as grain a envelope the slow growing ones shown as grain b [Mahieu *et al.*, 2006].

The structure zone model can be evaluated for the formation of (002) texture in permalloy, since the model place no requirement on the properties of the films except the reduced temperature. However, by the same reason, this model is too general in predicting all fcc structured films could have an (002) texture on amorphous substrate at appropriate substrate temperatures, which is in contrary to the experimental observation that (111) texture is commonly observed in fcc metal films such as Pt [Hecq *et al.*, 1981], Ir [Cha 1997], and Rh [Marot *et al.*, 2008]. In addition, due to the lack of dependence of film texture on other relevant parameters such as film thickness and alloy composition, the structure zone model cannot be applied to explain the transition of texture in permalloy films on β -W.

6.5 Summary

The deposition of (002) textured permalloy on β -W using amorphous glass substrates is demonstrated, and the dependence of the degree of texture on the deposition parameters is discussed. In order to explain the unique feature of (002) texture in permalloy, the lattice mismatch model, surface energy model, and structure zone model are applied to the β -W/permalloy bilayer system, but none of these model could provide a satisfactory explanation for the texture formation. Therefore, the origin of texture remains unresolved.

7 – Differential Scanning Calorimetry Characterization of β -W to α -W Phase Transition

7.1 Experimental Details

7.1.1 Sputter Deposition of Thin Films

Cu film with thickness of 300 nm was deposited onto 3 inch diameter Si(100) wafers at room temperature by DC magnetron sputtering. The Cu film is the sacrificial layer for lift-off with nitric acid. The previous chapters show that β -W cannot be deposited directly onto the Cu underlayer, as the tungsten film contains only α -W even in the presence of nitrogen impurities. Therefore, a spacer between Cu layer and W film is needed for the deposition of β -W, and the spacer has to be compatible with the chemistry of Cu lift-off recipe. Since β -W can be deposited on amorphous SiO₂ layer which is resistant to the nitric acid, the SiO₂ layer could be adopted as the spacer. Thus the SiO₂ layer with thickness of 100nm was deposited by RF magnetron sputtering. The deposition of both Cu and SiO₂ layers was performed with base pressure of better than 2×10^{-8} torr, and 3 mTorr argon flowing at 20 sccm was used as the sputtering gas. After the deposition of SiO₂ underlayer, the base pressure rose to 10^{-7} torr due to the release of oxygen atoms during the deposition process of SiO₂. Since the partial pressure of gas impurities is important in the formation of β -W, 2 hours pumping was conducted to reduce the base pressure back to the range of 10^{-8} torr. Then the 1 μ m-thick β -W films were deposited on the SiO₂ underlayer under the 3 mTorr Ar and 1.2×10^{-5} torr N₂. Following the deposition, the XRD pattern of the β -W/SiO₂/Cu/Si stacks was measured with Rigaku Ultima III diffractometer with parallel-beam geometry at Center for Functional Nanomaterials at Brookhaven National Laboratory., in order to determine the phase in tungsten films.

7.1.2 Preparation of Free-Standing β -W Flakes

The β -W and SiO_2 films were lifted-off from the substrate by using nitric acid, which dissolves Cu but does not react with tungsten or SiO_2 films. Free-standing flakes of W- SiO_2 bilayers were obtained after chemical etching. The flakes were then cleaned in distilled water, acetone and isopropyl alcohol. Then the SiO_2 layer was dissolved by dipping in 49% hydrofluoric acid for several seconds. The sputtered SiO_2 has very loose structure and its reaction rate with hydrofluoric acid is in the range of hundreds of nanometer per second, hence a short dipping can effectively remove all SiO_2 from the flakes. The tungsten films form dense oxide layer in hydrofluoric which prevents the reaction from proceeding, hence they were left intact. After the removal of SiO_2 layer, the W flakes were cleaned in distilled water, acetone and isopropyl alcohol again.

7.1.3 DSC Specimen Assembly and Measurement

The tungsten flakes need to be properly assembled in order for DSC measurement. Envelopes made of Pt foils were used as the container for the tungsten flakes, and Pt was favored over the standard Al pans because the maximum operating temperature of DSC using Al pans is limited by the melting point of Al to 600°C. The procedure for the construction of Pt envelopes were shown in Figure 7.1. The Pt pieces were made of 7 mm \times 7 mm \times 0.025 mm pieces of 99.99% pure foil. The Pt pieces were weighed and then folded into envelopes by folding three of the corners into the center, leaving one side open and shaping into one small pocket. Approximately 5 mg of film was placed in the envelope, then the last corner of the envelope was folded to the center and the envelope was flattened. The four corners of the envelopes were folded again into the center in order to keep the flakes tight inside. The weight of the specimen

could then be calculated as the difference between the envelope + sample weight and the original envelope weight. It is necessary to measure the sample weight by subtraction after the sample is loaded, since the loss of sample during handling and packing process is inevitable.

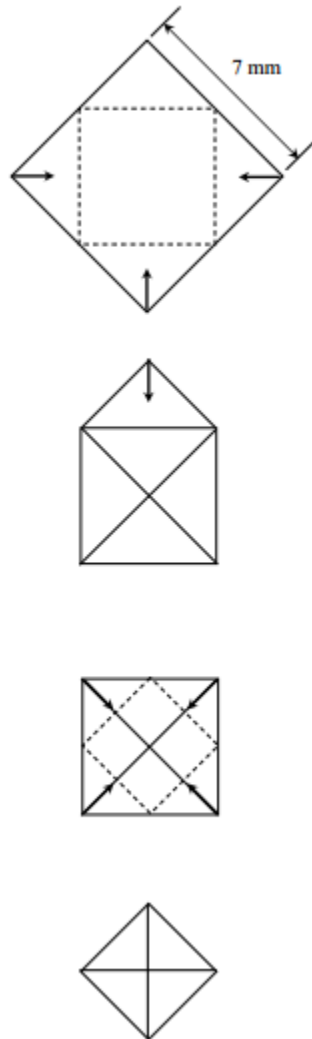


Figure 7.1. The schematic diagram for packing the β -W flakes into envelopes for DSC measurement [Berry 2007].

With the samples packed and weighed, DSC experiments were conducted in a Perkin Elmer DSC-7. Temperature, enthalpy and thermal lag were calibrated using In and Zn reference metals. Prior to the measurement, the DSC chamber was evacuated with a mechanical pump attached to the exhaust line for 45 minutes, then purged with argon for 30 minutes, in order to reduce residual oxygen and water vapor in the chamber. A DSC scan without any specimen at the heating rate of 40°C/min to 700°C was performed for instrument conditioning, so that the baseline of the equipment became stable. Then the non-isothermal DSC measurements were conducted with the flake-filled Pt envelope in the sample chamber and empty Pt envelope in the reference chamber, and the heating rates were chosen at 20, 40, 60 and 80 °C/min. After the first DSC scan for each specimen, a second DSC scan of the same specimen under the same conditions was conducted. As the β - to α -W phase transition is irreversible, the specimen after the first scan only contains α -W, hence the data of the second scan is only associated with the baseline of the instrument and the heat capacity of the specimen, which is assumed to be the same for α -W and β -W. By subtracting the data of the second scan from those of the first scan at corresponding temperatures, the signal containing only the contribution from the heat of β - to α -W phase transition.

7.2 Results

The XRD pattern of W/SiO₂/Cu/Si stacks is shown in Figure 7.2, and the presence of β -W phase is indicated by the corresponding strong diffraction peaks. On the other hand, the (200) peak of α -W at about $2\theta=58^\circ$ is not observed, therefore the 1 μ m films contain only β -W phase. The ability to obtain β -W in films at large thicknesses is one of the advantages of sputter deposition technique with N₂ impurity.

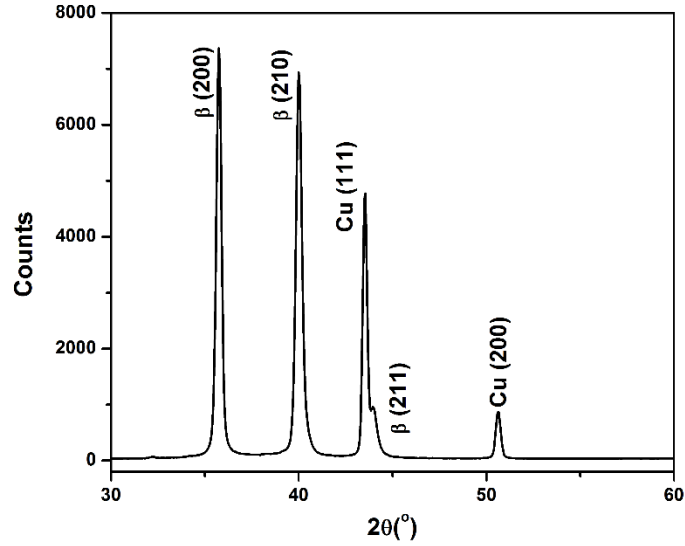


Figure 7.2. The XRD pattern of the β -W/SiO₂/Cu/Si structure measured with θ - 2θ scan.

The original DSC curves of the β -W in two consecutive scans of the same specimen are shown in Figure 7.3. The exothermic peak at about 500°C that is present in the first scan and absent in the second is caused by the change of enthalpy during β - to α -W phase transition. The signal caused only by the phase transformation is derived by subtracting the curve of the second scan from that of the first scan, and the corresponding results are shown in Figure 7.4. The exothermic peak is located at temperatures above 500°C, therefore the β -W should be kinetically stable below 500°C in post-deposition annealing treatments.

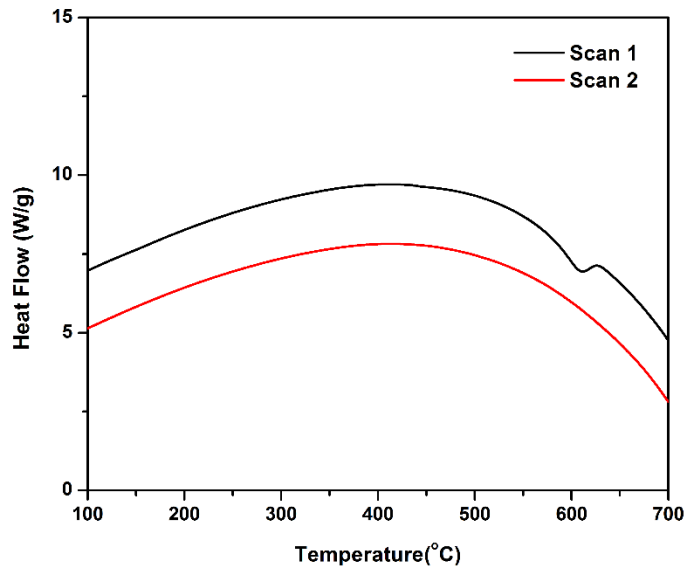


Figure 7.3. The DSC curves of β -W flakes obtained at 40°C/min heating rate. The curves are displaced for clarity.

The enthalpy of β - to α -W phase transition can be calculated from the area of the peak using equation 3-7, and the value is obtained by interpolating a sigmoid baseline below the peak as 8.3 ± 0.4 kJ/mol. On the other hand, the enthalpy of β -W with reference to α -W has been calculated using density functional theory as 8.7 kJ/mol [Jain *et al.*, 2013]. The similarity between the values in the experiment and the calculation indicates the peak observed in the curve of the first DSC scan is indeed caused by the β - to α -W phase transition.

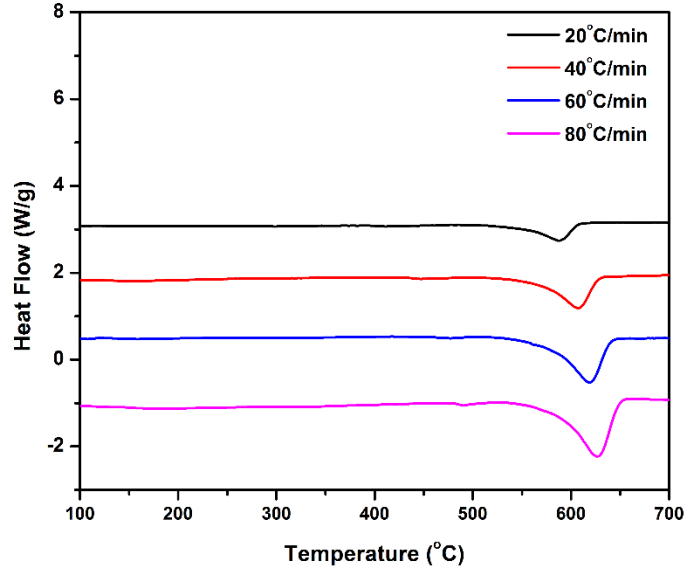


Figure 7.4. The DSC curves of β -W flakes measured at different heating rates. The curves were obtained by subtracting the curves of the second scans from those of the first scans. The curves are displaced for clarity.

The kinetics of the β - to α -W phase transition causes the shift of the peaks in non-isothermal DSC curve to higher temperatures at larger heating rate, and the shift of the peaks indicates the phase transition is a thermally activated process, in which the atomic energy needed to overcome the barrier for phase transition is supplied by their thermal vibration. The reaction rate constant of thermally activated process follows the Arrhenius equation as

$$k = k_0 \exp\left(-\frac{Q}{k_B T}\right) \quad (7-1)$$

where k is the rate constant, and Q is the corresponding activation energy.

The activation energy Q can be extracted from the shift of peaks with heating rates by Kissinger method [Kissinger 1957] according to equation 7-2 as

$$\ln \frac{k_B A}{Q} - \frac{Q}{k_B T_{peak}} = \ln \frac{\beta}{T_m^2} \quad (7-2)$$

where T_{peak} is the peak temperature in the DSC curves that only contain the signal from the phase transition, and it indicates the temperature at which the maximum phase transition rate occurs.

By plotting $\ln \frac{\beta}{T_m^2}$ as x-axis and $\frac{1}{k_B T_{peak}}$ as y-axis, the data points should lie on a straight line and

the slope of the straight line is the effective activation energy Q of the overall phase transition.

The peak temperatures obtained at different heating rates are listed in Table 7.1, and the plot with

$\ln \frac{\beta}{T_m^2}$ as x-axis and $\frac{1}{k_B T_{peak}}$ as y-axis is shown in Figure 7.5. The activation energy of β - to α -W

phase transition is calculated as 2.2 eV.

Table 7.1. The peak temperatures of DSC curves obtained at different heating rates.

β (°C/min)	T_{peak} (°C)
20	587
40	607
60	619
80	627

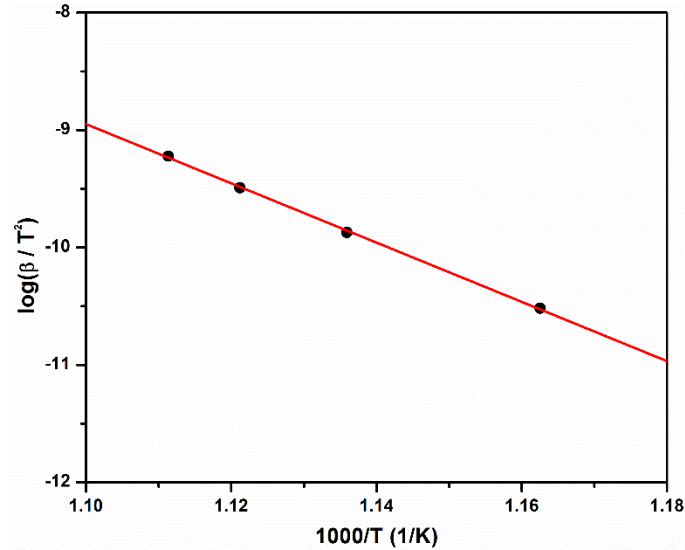


Figure 7.5. The plot showing the relationship between peak temperatures and heating rates in DSC. The slope is the activation energy of the β - to α -W phase transition.

7.3 Discussion

The activation energy of β - to α -W phase transition calculated from the slope of Kissinger plot is 2.2 eV. The activation energy has also been measured by post-annealing and resistivity measurement, and the reported value of β - to α -W phase transition are 0.75 eV [Tang *et al.*, 1984] in PECVD films, 0.7 eV for RF sputtered tungsten films [Petroff *et al.*, 1973], and 1.1 eV for DC sputtered films [Rossnagel *et al.*, 2002]. The difference in the reported value and the activation energy measured here could be attributed to the difference in specimen thicknesses in the different studies. In prior reports[Tang *et al.*, 1984, Petroff *et al.*, 1973, Rossnagel *et al.*, 2002], film thicknesses were in the range 20 nm, while the thickness of the specimen for DSC measurement is about 1 μ m. For thinner films, the phase transition could be influenced by the strain in the films, or the interface between the film and substrates, and these factors become less influential to the phase transition in 1 μ m films. Therefore, the value measured here by DSC is

intrinsic to the kinetics of β - to α -W phase transition and is close to the value of the bulk specimen.

On the other hand, the activation energies measured in all experiments are extremely small, considering that the tungsten has a very high melting point at 3422°C. In order to gain insight into the kinetics of β - to α -W phase transition, the activation energy is compared to that of other diffusion processes in tungsten materials. The lattice diffusion activation energy for α -W is about 7 eV [Mundy *et al.*, 1978], and the grain boundary diffusion activation energy for α -W is about 4 eV [Lee *et al.*, 1997] which is about half of that for lattice diffusion. For diffusional phase transition, the effective activation energy usually consists of that for diffusion as well as that for nucleation, since the diffusion across the energy barrier to reach destined atom configuration is necessary. However, both of the diffusion processes have higher activation energy compared to that of β - to α -W phase transition. On the other hand, although the activation energy is close to that for surface diffusion [Petroff *et al.*, 1973], the density of β -W is the same as α -W as evidenced by the measurement of X-ray reflectivity and density functional theory calculation, hence it is unlikely that such fast-diffusion channel exists in β -W. In conclusion, the small activation energy measured by DSC indicates that the β - to α -W phase transition is unlikely to be diffusional.

On the other hand, the diffusionless phase transition, in which no transition across the large activation barrier is involved, could have a very low activation energy [Sangeeta *et al.*, 2004], hence this mechanism could potentially be responsible for the observed low β to α -W phase transition with low activation energy. In a diffusionless phase transformation, no long range diffusion occurs. Instead, the atoms only moves over distances smaller than the inter-atomic distance by displacement. In this way, the atoms maintain their relative position in the

new phase [Delaey 2006]. A classification of the phase transition by how the atomic configuration changes from its matrix [Cohen *et al.*, 1979] is shown in Figure 7.6. There are two main types of diffusionless phase transformation: In the lattice-distortive transformations, the displacement of all atoms takes place collectively, and there are usually strain energy associated with the corresponding change of shape of the unit cell [Delaey 2006]. One example of lattice-distortive phase transition is martensitic phase transition in steel and shape-memory alloys, in which the driving force is the shear strain energy in the bulk [James *et al.*, 2000]. In the shuffle transformation, the kinetics of phase transition is dominated by the shuffle displacement taking place inside the unit cell, hence there is little strain energy associated with the atom displacement since the overall shape of the unit cell is kept the same after the phase transformation phase [Delaey 2006]. The examples of shuffle phase transformation includes hcp – bcc phase transition in Ti and Zr alloys [Cohen *et al.*, 1979].

Several aspects of the β to α -W phase transformation are consistent with the characteristics of shuffle transformation. It is commonly found that in shuffle transformation, the point group of one phase is the subgroup of the other phase [Delaey 2006], and the 223 space group of β -W $Pm\bar{3}n$ is indeed one of the maximal subgroups of the 229 space group of α -W $Im\bar{3}m$ [Chester 2006]. On the other hand, the β -W phase has a topologically closely packed structure, the A15 structure, and diffusionless phase transitions are commonly found in other topologically closely packed structured materials even below room temperature [Masaki 1981]. Therefore, it does not come as a surprise that the β - to α -W phase transition can occur as diffusionless.

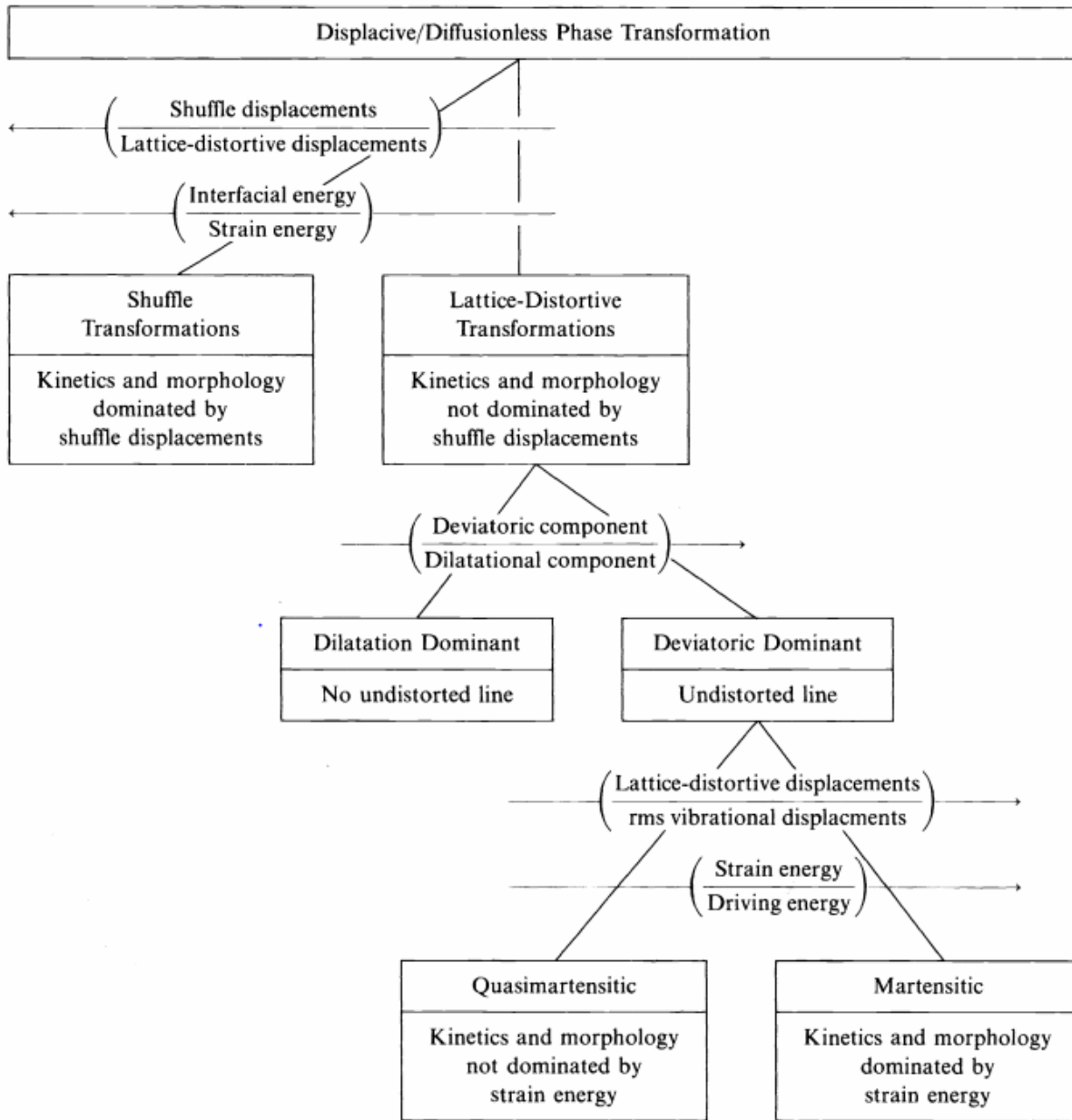


Figure 7.6. The classification of diffusionless classification [Cohen *et al.*, 1979].

7.4 Summary

A lift-off procedure for the deposition of free-standing $1\mu\text{m}$ β -W films was developed, and the enthalpy and the activation energy β - to α -W phase transition were measured. The low activation energy of the phase transition could be explained by the mechanism of diffusionless shuffle phase transformation, and a possible mechanism of the shuffle phase transition is proposed that can avoid the high lattice diffusion activation barrier.

8 – Conclusions

8.1 Summary

In this thesis, the deposition conditions and properties of β -W thin films with the A15 structure were investigated. By introducing N_2 impurity during the deposition process, the β -W phase formed in the tungsten films and it was shown that its volume fraction could be controlled by the pressure of N_2 gas. This deposition process using N_2 impurity has the advantages over known methods, including low deposition rate, high inert gas pressure, or oxygen gas impurity, allowing high purity β -W to be deposited with reasonable yield, with thicknesses of the β -W films larger than $1\ \mu\text{m}$. This technique is useful in producing β -W films for applications as the source of spin-polarized current due to the giant spin Hall effect.

In addition to the dependence on N_2 pressure, the relationship between the volume fraction of β -W and the substrate temperature and deposition rate was also investigated. It was shown that the relationship could be modeled using the Langmuir-Freundlich isotherm, hence this model provided insight into the mechanism of β -W formation, which requires the adsorption of nitrogen molecules onto the substrate. The nitrogen molecules are strongly interacting mediated by their mutual interaction with the tungsten atoms, and as a result of the interaction the nitrogen molecules behave like a cluster that act as the nuclei of the β -W grains during the deposition process.

The effect of underlayer materials on the formation of β -W is also investigated experimentally, and the result shows the β -W phase can only form on the underlayer materials containing non-metal elements. The dependence is attributed by the requirement of covalent bonds in the underlayers, which is inevitable for the stabilization of β -W nuclei at the initial

stage of deposition.

The texture of permalloy thin films deposited on β -W is investigated. The permalloy film forms (002) instead of (111) texture when β -W is the underlayer. This observation provides a useful structure as the seed layer for the formation of (002) textured films on amorphous substrates. However, the mechanism of the (002) texture formation cannot be explained by any of the existing models.

A lift-off recipe for producing free-standing $1\mu\text{m}$ β -W flakes has been developed and used to make specimen for the investigation of β - to α -W phase transition by differential scanning calorimetry using. The enthalpy of phase transition is measured to be 8.3 ± 0.4 kJ/mol, and the value is consistent with the calculation using density functional theory. The low activation energy of phase transition at 2.2 eV is attributed to the mechanism of diffusionless shuffle transformation responsible for the β - to α -W phase transition.

8.2 Suggestions for Future Work

The model for the relationship between the deposition conditions and β -W volume fraction is based upon the simple phase analysis from XRD pattern. However, the calculation is not very accurate as the result is influenced by the texture of the tungsten films. Therefore, a detailed study of the crystallographic orientation of β -W grains by pole figures needs to be conducted in order to understand the evolution of texture. In addition, the phase fraction calculated from the XRD should be compared with that from the TEM images as the cross validation of the volume fraction calculation procedure.

As shown in chapter 4, the recipe for the deposition of β -W on permalloy has been realized by reducing the deposition power to 10W. This structure is ready to be used to measure the spin

diffusion length of β -W thin films accurately in ferromagnetic resonance experiment at different thicknesses of permalloy and β -W.

In addition to N_2 impurity pressure, substrate temperature, and deposition rate investigated in Chapter 4, other deposition conditions, including the pressure of inert gas and the substrate bias, could also be important in determining the phase fraction of β -W in the films and could provide insight into the formation mechanism of β -W. Therefore, a more detailed investigation in the deposition parameter space should provide a better understanding on the relationship between the deposition conditions and β -W formation.

Although in the chapter 5 and 6, the explanation of the dependence of β -W formation on the underlayer materials and the (002) texture formation in permalloy on β -W has been attempted, the explanation is extremely simplistic and in fact no successful model has been found for the (002) texture formation in permalloy. Therefore, the calculation of fundamental parameters at the interface of the bilayers, such as the interfacial energy between the permalloy and the β -W films should be conducted, which could suggest the possible mechanism for the unusual behavior of β -W.

Bibliography

- V. An, Features of Beta-to-Alpha Transformation in Electroexplosive Tungsten Nanopowders, in *Proceedings of The 9th Russian-Korean International Symposium on Science and Technology*, pp. 110, (2005).
- R. J. Antinone and G. W. Brown, *The Modeling of Resistive Interconnects for Integrated Circuits*, IEEE J. Solid-State Circuits **18**, 200 (1983).
- M. S. Aouadi, R. R. Parsons, P. C. Wong, and K. A. R. Mitchell, *Characterization of Sputter Deposited Tungsten Films for X-Ray Multilayers*, J. Vac. Sci. Technol., A **10**, 273 (1992).
- D. D. Awschalom and N. Samarth, *Spintronics without Magnetism*, Physics **2**, 50 (2009).
- J. Ayache, L. Beaunier, J. Boumendil, G. Ehret, and D. Laub, in *Sample Preparation Handbook for Transmission Electron Microscopy: Methodology* (Springer New York, New York, NY, 2010), pp. 83.
- C. C. Baker and S. I. Shah, *Reactive Sputter Deposition of Tungsten Nitride Thin Films*, J. Vac. Sci. Technol., A **20**, 1699 (2002).
- A. A. Bakun, B. P. Zakharchenya, A. A. Rogachev, M. N. Mtkachuk, and V. G. Fleisher, *Observation of a Surface Photocurrent Caused by Optical Orientation of Electrons in a Semiconductor*, JETP Lett. **40**, 1293 (1984).
- S. Basavaiah and S. R. Pollack, *Superconductivity in β -Tungsten Films*, J. Appl. Phys. **39**, 5548 (1968).
- D. C. Berry, *Ultrahigh Density Magnetic Recording Media: The $A1$ to $L1_0$ Phase Transformation in FePt and Related Ternary Alloy Films*, PhD Thesis, Carnegie Mellon University, Pittsburgh, PA, 2007.
- W. M. Bullis and A. J. ABaroody, *Methods of Measurement for Semiconductor Materials, Process Control, and Devices* (NBS Technical Note 555, 1970), pp. 10.
- H. H. Busta and C. H. Tang, *Film Thickness Dependence of Silicon Reduced Lpcvd Tungsten on Native Oxide Thickness*, J. Electrochem. Soc. **133**, 1195 (1986).
- J. W. Cahn and J. Taylor, *Heterogeneous Nucleation*, Phase Transformation **87**, 545 (1988).
- S. Y. Cha, B. T. Jang, D. H. Kwak, C. H. Shin, and H. C. Lee, *Iridium Thin Film as a Bottom Electrode for High Dielectric (Ba, Sr)TiO₃ Capacitors*, Ferroelectr. **17(1-4)**, 187 (1997).
- J. S. Chen, C. J. Sun, and G. M. Chow, *A Review of $L1_0$ FePt Films for High-Density Magnetic Recording*, Int. J. Prod. Dev **5**, 238 (2008).
- T. H. Chester, *International Tables for Crystallography. Vol. A, Space-Group Symmetry* (International Union of Crystallography, 2006), 1st online edn.
- Y.-N. Chiu and F. E. Wang, *Multiple Metal-Metal Bonding and a -Chain Integrity in Superconducting A_3B (β -Tungsten) Alloy*, J. Solid State Chem. **45**, 353 (1982).

- D. Choi *et al.*, *Phase, Grain Structure, Stress, and Resistivity of Sputter-Deposited Tungsten Films*, J. Vac. Sci. Technol., A **29**, 051512 (2011).
- K. Christmann, O. Schober, G. Ertl, and M. Neumann, *Adsorption of Hydrogen on Nickel Single Crystal Surfaces*, J. Chem. Phys. **60**, 4528 (1974).
- L. A. Clevenger, A. Mutscheller, J. M. E. Harper, C. Cabral, and K. Barmak, *The Relationship between Deposition Conditions, the Beta to Alpha Phase Transformation, and Stress Relaxation in Tantalum Thin Films*, J. Appl. Phys. **72**, 4918 (1992).
- M. Cohen, G. B. Olson, and P. C. Clapp, in *Proc. ICOMAT '79* Cambridge, MA), p. 1, (1979).
- P. Collot, B. Agius, P. Estrache, M. C. Hugon, M. Froment, J. Bessot, and Y. Crassin, *Physicochemical Properties in Tungsten Films Deposited by Radio - Frequency Magnetron Sputtering*, J. Vac. Sci. Technol., A **6**, 2319 (1988).
- M. J. Cooke, *A Review of LPCVD Metallization for Semiconductor Devices*, Vacuum **35**, 67 (1985).
- D. Davazoglou and K. Georgouleas, *Low Pressure Chemically Vapor Deposited WO₃ Thin Films for Integrated Gas Sensor Applications*, J. Electrochem. Soc. **145**, 1346 (1998).
- D. Davazoglou, A. Moutsakis, V. Valamontes, V. Psycharis, and D. Tsamakis, *Tungsten Oxide Thin Films Chemically Vapor Deposited at Low Pressure by W (CO)₆ Pyrolysis*, J. Electrochem. Soc. **144**, 595 (1997).
- P. W. DeHaven, L. A. Clevenger, R. F. Schnabe, S. J. Weber, R. C. Iggulden, and K. P. Rodbell, *Crystallographic Texture and Phase Formation in Blanket TifriN/AlCu Films*, Mat. Res. Soc. Symp. Proc. **514**, 105 (1998).
- L. Delaey, in *Materials Science and Technology* (Wiley-VCH Verlag GmbH & Co. KGaA, 2006).
- I. Djerdj, A. M. Tonejc, A. Tonejc, and N. Radić, *XRD Line Profile Analysis of Tungsten Thin Films*, Vacuum **80**, 151 (2005).
- G. Dresselhaus, *Spin-Orbit Coupling Effects in Zinc Blende Structures*, Phys. Rev. **100**, 580 (1955).
- S. R. Droes, T. T. Kodas, and M. J. Hampden-Smith, in *Carbide, Nitride and Boride Materials Synthesis and Processing*, edited by A. W. Weimer (Springer Netherlands, Dordrecht, 1997), pp. 579.
- S. L. Duan, J. O. Artman, B. Wong, and D. E. Laughlin, *Study of the Growth Characteristics of Sputtered Cr Thin Films*, J. Appl. Phys. **67**, 4913 (1990).
- N. Durand, K. F. Badawi, and P. Goudeau, *Influence of Microstructure on Residual Stress in Tungsten Thin Films Analyzed by X-Ray Diffraction*, Thin Solid Films **275**, 168 (1996).
- M. I. Dyakonov and V. I. Perel, *Current-Induced Spin Orientation of Electrons in Semiconductors*, Phys. Lett. A **35**, 459 (1971).

- M. I. D'yakonov and V. I. Perel', *Possibility of Orienting Electron Spins with Current*, JETP Lett. **13**, 467 (1971).
- D. W. Face and D. E. Prober, *Nucleation of Body-Centered-Cubic Tantalum Films with a Thin Niobium Underlayer*, J. Vac. Sci. Technol., A **5**, 3408 (1987).
- L. G. Feinstein and R. D. Huttemann, *Factors Controlling the Structure of Sputtered Ta Films*, Thin Solid Films **16**, 129 (1973).
- Y. C. Feng, D. E. Laughlin, and D. N. Lambeth, *Formation of Crystallographic Texture in RF Sputter-Deposited Cr Thin Films*, J. Appl. Phys. **76**, 7311 (1994).
- L. B. Freund and S. Suresh, *Thin Film Materials: Stress, Defect Formation and Surface Evolution* (Cambridge University Press, UK, 2009).
- E. Gage, K.-Z. Gao, and J.-G. Zhu, in *Ultrahigh-Density Magnetic Recording*, edited by G. Varvaro, and F. Casoli (CRC Press, Boca Raton, FL, 2016).
- M. D. Graef and M. E. McHenry, *Structure of Materials: An Introduction to Crystallography, Diffraction and Symmetry* (Cambridge University Press, UK, 2012), 2nd edn.
- T. Gupta, in *Copper Interconnect Technology* (Springer New York, New York, NY, 2009), pp. 111.
- G. Hägg and N. Schönberg, ' β -Tungsten' as a Tungsten Oxide, Acta Crystallogr. **7**, 351 (1954).
- A. M. Haghiri-Gosnet, F. R. Ladan, C. Mayeux, and H. Launois, *Stresses in Sputtered Tungsten Thin Films*, Appl. Surf. Sci. **38**, 295 (1989).
- Q. Hao, W. Chen, and G. Xiao, *Beta (β) Tungsten Thin Films: Structure, Electron Transport, and Giant Spin Hall Effect*, Appl. Phys. Lett. **106**, 182403 (2015).
- Q. Hao and G. Xiao, *Giant Spin Hall Effect and Switching Induced by Spin-Transfer Torque in a W/Co₄₀Fe₄₀B₂₀/MgO Structure with Perpendicular Magnetic Anisotropy*, Phys. Rev. Appl **3**, 034009 (2015).
- M. Hecq and A. Hecq, *Oxygen Induced Preferred Orientation of DC Sputtered Platinum*, J. Vac. Sci. Technol. **18**, 219 (1981).
- K. Hieber and N. M. Mayer, *Structural Changes of Evaporated Tantalum During Film Growth*, Thin Solid Films **90**, 43 (1982).
- K. Hirokazu, Y. Yusuke, A. Atif Mossad, L. Jun, F. Takafumi, T. Tetsu, and K. Mitsumasa, *Tungsten through-Silicon Via Technology for Three-Dimensional LSIs*, Jpn. J. Appl. Phys. **47**, 2801 (2008).
- E. Hirota, H. Sakakima, and K. Inomata, in *Giant Magneto-Resistance Devices* (Springer Berlin Heidelberg, Berlin, Heidelberg, 2002), pp. 135.
- J. E. Hirsch, *Spin Hall Effect*, Phys. Rev. Lett. **83**, 1834 (1999).
- R. Hoogeveen, M. Moske, H. Geisler, and K. Samwer, *Texture and Phase Transformation of Sputter-Deposited Metastable Ta Films and TaCu Multilayers*, Thin Solid Films **275**, 203 (1996).

- M. C. Hugon, F. Varniere, B. Agius, M. Froment, C. Arena, and J. Bessot, *Stresses, Microstructure and Resistivity of Thin Tungsten Films Deposited by RF Magnetron Sputtering*, Appl. Surf. Sci. **38**, 269 (1989).
- H. Y. Hung, G. Y. Luo, Y. C. Chiu, P. Chang, W. C. Lee, J. G. Lin, S. F. Lee, M. Hong, and J. Kwo, *Detection of Inverse Spin Hall Effect in Epitaxial Ferromagnetic Fe₃Si Films with Normal Metals Au and Pt*, J. Appl. Phys. **113**, 17C507 (2013).
- K. Jabeur, L. D. Buda-Prejbeanu, G. Prenat, and G. D. Pendina, *Study of Two Writing Schemes for a Magnetic Tunnel Junction Based on Spin Orbit Torque*, World Acad. Sci. Eng. Technol., Int. Sci. Index 80, Int. J. Electr., Electron. Sci. Eng. **7**, 517 (2013).
- K. Jabeur, G. D. Pendina, F. Bernard-Granger, and G. Prenat, *Spin Orbit Torque Non-Volatile Flip-Flop for High Speed and Low Energy Applications*, IEEE Electron Device Lett. **35**, 408 (2014).
- K. Jabeur, G. Prenat, G. D. Pendina, L. D. Buda-Prejbeanu, I. L. Prejbeanu, and B. Dieny, *Compact Model of a Three-Terminal Mram Device Based on Spin Orbit Torque Switching*, in *Semiconductor Conference Dresden-Grenoble (ISCDG), 2013 International*, pp. 1, (2013).
- B. Jack and P. P. William, Jr., *Spin-Diffusion Lengths in Metals and Alloys, and Spin-Flipping at Metal/Metal Interfaces: An Experimentalist's Critical Review*, J. Phys.: Condens. Matter **19**, 183201 (2007).
- A. Jain *et al.*, *Commentary: The Materials Project: A Materials Genome Approach to Accelerating Materials Innovation*, APL Mater. **1**, 011002 (2013).
- R. D. James and K. F. Hane, *Martensitic Transformations and Shape-Memory Materials*, Acta Mater. **48**, 197 (2000).
- S. S. Jiang, A. Hu, R. W. Peng, and D. Feng, *Quasiperiodic Metallic Multilayers*, J. Magn. Magn. Mater. **126**, 82 (1993).
- M. Johnson and R. H. Silsbee, *Interfacial Charge-Spin Coupling: Injection and Detection of Spin Magnetization in Metals*, Phys. Rev. Lett. **55**, 1790 (1985).
- T. Jungwirth, J. Wunderlich, and K. Olejnik, *Spin Hall Effect Devices*, Nat. Mater. **11**, 382 (2012).
- T. Karabacak, A. Mallikarjunan, J. P. Singh, D. Ye, G.-C. Wang, and T.-M. Lu, *β -Phase Tungsten Nanorod Formation by Oblique-Angle Sputter Deposition*, Appl. Phys. Lett. **83**, 3096 (2003).
- S. Kasap, C. Koughia, H. Ruda, and R. Johanson, in *Springer Handbook of Electronic and Photonic Materials*, edited by S. Kasap, and P. Capper (Springer US, Boston, MA, 2007), pp. 19.
- Y. K. Kato, R. C. Myers, A. C. Gossard, and D. D. Awschalom, *Observation of the Spin Hall Effect in Semiconductors*, Science **306**, 1910 (2004).
- M. H. Kibel, in *Surface Analysis Methods in Materials Science*, edited by D. J. O'Connor, B. A. Sexton, and R. S. C. Smart (Springer Berlin Heidelberg, Berlin, Heidelberg, 2003), pp. 175.

- Y. Kim, X. Fong, and K. Roy, *Spin-Orbit-Torque-Based Spin-Dice: A True Random-Number Generator*, IEEE Magn. Lett. **6**, 1 (2015).
- T. Kimura, Y. Otani, T. Sato, S. Takahashi, and S. Maekawa, *Room-Temperature Reversible Spin Hall Effect*, Phys. Rev. Lett. **98**, 156601 (2007).
- H. E. Kissinger, *Reaction Kinetics in Differential Thermal Analysis*, Anal. Chem. **29**, 1702 (1957).
- T. Kizuka, T. Sakamoto, and N. Tanaka, *Growth of Fine Crystals with A-15 Type Structure in Vacuum-Deposited Tungsten Films Studied by High-Resolution Electron Microscopy*, J. Cryst. Growth **131**, 439 (1993).
- J. U. Knickerbocker *et al.*, *Three-Dimensional Silicon Integration*, IBM J. Res. Dev. **52**, 553 (2008).
- S. J. Koester *et al.*, *Wafer-Level 3D Integration Technology*, IBM J. Res. Dev. **52**, 583 (2008).
- J. B. Kortright, S. Joksch, and E. Ziegler, *Stability of Tungsten/Carbon and Tungsten/Silicon Multilayer X-Ray Mirrors under Thermal Annealing and X - Radiation Exposure*, J. Appl. Phys. **69**, 168 (1991).
- T. Koyano, C. H. Lee, T. Fukunaga, U. Mizutani, S. Ikeda, Y. Higuchi, M. Nishikawa, E. Kita, and A. Tasaki, *Structural Studies of Multilayered Films Composed of Immiscible Pairs Cu and Ta*, J. Magn. Magn. Mater. **126**, 161 (1993).
- I. V. Kozhevnikov and A. V. Vinogradov, *Multilayer X-Ray Mirrors*, J. Russ. Laser Res. **16**, 343 (1995).
- J. M. Larson and J. P. Snyder, *Overview and Status of Metal S/D Schottky-Barrier MOSFET Technology*, IEEE Trans. Electron Devices **53**, 1048 (2006).
- E. Lassner and W. D. Schubert, in *Tungsten: Properties, Chemistry, Technology of the Element, Alloys, and Chemical Compounds* (Springer US, Boston, MA, 1999), pp. 85.
- H. J. Lee, *Texture and Morphology of Sputtered Cr Thin Films*, J. Appl. Phys. **57**, 4037 (1985).
- J. S. Lee, C. Minkwitz, and C. Herzig, *Grain Boundary Self-Diffusion in Polycrystalline Tungsten at Low Temperatures*, Phys. Status Solidi B **202**, 931 (1997).
- J.-S. Lee, J. Cho, and C.-Y. You, *Growth and Characterization of α and β -Phase Tungsten Films on Various Substrates*, J. Vac. Sci. Technol., A **34**, 021502 (2016).
- F. Liu *et al.*, *A 300-mm Wafer-Level Three-Dimensional Integration Scheme Using Tungsten through-Silicon Via and Hybrid Cu-Adhesive Bonding*, in *2008 IEEE International Electron Devices Meeting*, pp. 1, (2008).
- J. Liu, and K. Barmak, *Topologically Close-Packed Phases: Deposition and Formation Mechanism of Metastable β -W in Thin Films*, Acta Mater. **104**, 223 (2016).

- L. Liu, C. F. Pai, Y. Li, H. W. Tseng, D. C. Ralph, and R. A. Buhrman, *Spin-Torque Switching with the Giant Spin Hall Effect of Tantalum*, *Science* **336**, 555 (2012).
- C. F. Lo, P. McDonald, D. Draper, and P. Gilman, *Influence of Tungsten Sputtering Target Density on Physical Vapor Deposition Thin Film Properties*, *J. Electron. Mater.* **34**, 1468 (2005).
- S. Mahieu, P. Ghekiere, D. Depla, and R. De Gryse, *Biaxial Alignment in Sputter Deposited Thin Films*, *Thin Solid Films* **515**, 1229 (2006).
- L. Maillé, C. Sant, and P. Garnier, *A Nanometer Scale Surface Morphology Study of W Thin Films*, *Mater. Sci. Eng., C* **23**, 913 (2003).
- L. Maillé, C. Sant, C. Le Paven-Thivet, C. Legrand-Buscema, and P. Garnier, *Structure and Morphological Study of Nanometer W and W₃O Thin Films*, *Thin Solid Films* **428**, 237 (2003).
- G. Mannella and J. O. Hougen, *" β -Tungsten" as a Product of Oxide Reduction*, *J. Phys. Chem.* **60**, 1148 (1956).
- L. Marot, G. De Temmerman, V. Thommen, D. Mathys, and P. Oelhafen, *Characterization of Magnetron Sputtered Rhodium Films for Reflective Coatings*, *Surf. Coat. Technol.* **202**, 2837 (2008).
- A. Masashi and N. Isao, *Tungsten Films with the A15 Structure*, *Jpn. J. Appl. Phys.* **32**, 1759 (1993).
- R. I. Masel, *Principles of Adsorption and Reaction on Solid Surfaces* (Wiley, New Jersey, 1996), 1st edn.
- R. Messier, A. P. Giri, and R. A. Roy, *Revised Structure Zone Model for Thin Film Physical Structure*, *J. Vac. Sci. Technol., A* **2**, 500 (1984).
- I. Miccoli, F. Edler, H. Pfnür, and C. Tegenkamp, *The 100th Anniversary of the Four-Point Probe Technique: The Role of Probe Geometries in Isotropic and Anisotropic Systems*, *J. Phys.: Condens. Matter* **27**, 223201 (2015).
- A. Miller and G. D. Barnett, *Chemical Vapor Deposition of Tungsten at Low Pressure*, *J. Electrochem. Soc.* **109**, 973 (1962).
- W. R. Morcom, W. L. Worrell, H. G. Sell, and H. I. Kaplan, *The Preparation and Characterization of Beta-Tungsten, a Metastable Tungsten Phase*, *Metall. Trans.* **5**, 155 (1974).
- O. Mosendz, J. E. Pearson, F. Y. Fradin, G. E. W. Bauer, S. D. Bader, and A. Hoffmann, *Quantifying Spin Hall Angles from Spin Pumping: Experiments and Theory*, *Phys. Rev. Lett.* **104**, 046601 (2010).
- M. Motoyoshi, *Through-Silicon Via (TSV)*, *Proc. IEEE* **97**, 43 (2009).
- B. A. Movchan and A. V. Demchishin, *Investigation of the Structure and Properties of Thick Vacuum- Deposited Films of Nickel, Titanium, Tungsten, Alumina and Zirconium Dioxide*, *Phys. Met. Metallogr* **28**, 653 (1969).
- J. N. Mundy, S. J. Rothman, N. Q. Lam, H. A. Hoff, and L. J. Nowicki, *Self-Diffusion in Tungsten*, *Phys. Rev. B* **18**, 6566 (1978).

- S. Murakami, N. Nagaosa, and S.-C. Zhang, *Dissipationless Quantum Spin Current at Room Temperature*, Science **301**, 1348 (2003).
- K. Murugan, S. B. Chandrasekhar, and J. Joardar, *Nanostructured α/β -Tungsten by Reduction of WO_3 under Microwave Plasma*, Int. J. Refract. Met. Hard Mater. **29**, 128 (2011).
- I. C. Noyan, T. M. Shaw, and C. C. Goldsmith, *Inhomogeneous Strain States in Sputter Deposited Tungsten Thin Films*, J. Appl. Phys. **82**, 4300 (1997).
- M. J. O'Keefe, J. T. Grant, and J. S. Solomon, *Magnetron Sputter Deposition of A-15 and BCC Crystal Structure Tungsten Thin Films*, J. Electron. Mater. **24**, 961 (1995).
- C. F. Pai, L. Liu, Y. Li, H. W. Tseng, D. C. Ralph, and R. A. Buhrman, *Spin Transfer Torque Devices Utilizing the Giant Spin Hall Effect of Tungsten*, Appl. Phys. Lett. **101**, 122404 (2012).
- D. C. Paine, J. C. Bravman, and C. Y. Yang, *Observations of β -Tungsten Deposited by Low Pressure Chemical Vapor Deposition*, Appl. Phys. Lett. **50**, 498 (1987).
- V. K. Pecharsky and P. Y. Zavalij, in *Fundamentals of Powder Diffraction and Structural Characterization of Materials* (Springer US, Boston, MA, 2009), pp. 347.
- N. J. Petch, *α -Tungsten*, Nature **154**, 337 (1944).
- P. Petroff, T. T. Sheng, A. K. Sinha, G. A. Rozgonyi, and F. B. Alexander, *Microstructure, Growth, Resistivity, and Stresses in Thin Tungsten Films Deposited by RF Sputtering*, J. Appl. Phys. **44**, 2545 (1973).
- H. O. Pierson, in *Handbook of Chemical Vapor Deposition (CVD) (Second Edition)* (William Andrew Publishing, Norwich, NY, 1999), pp. 367.
- H. O. Pierson, in *Handbook of Chemical Vapor Deposition (CVD) (Second Edition)* (William Andrew Publishing, Norwich, NY, 1999), pp. 147.
- J. Pressesky, S. Y. Lee, S. Duan, and D. Williams, *Crystallography and Magnetic Properties of CoCrTa Films Prepared on Cr Underlayers with Different Substrate Bias Conditions*, J. Appl. Phys. **69**, 5163 (1991).
- N. Radić, A. Tonejc, J. Ivkov, P. Dubček, S. Bernstorff, and Z. Medunić, *Sputter-Deposited Amorphous-Like Tungsten*, Surf. Coat. Technol. **180–181**, 66 (2004).
- E. Rashba, *Properties of Semiconductors with an Extremum Loop. I. Cyclotron and Combinational Resonance in a Magnetic Field Perpendicular to the Plane of the Loop*, Sov. Phys. Solid State **2**, 1224 (1960).
- D. P. Ravipati, W. G. Haines, and J. L. Dockendorf, *Effects of Argon Pressure and Substrate Heating on the Chromium Underlayer Used for High - Density Longitudinal CoNiCr Media*, J. Vac. Sci. Technol., A **5**, 1968 (1987).
- J. C. Rojas-Sánchez *et al.*, *Spin Pumping and Inverse Spin Hall Effect in Platinum: The Essential Role of Spin-Memory Loss at Metallic Interfaces*, Phys. Rev. Lett. **112**, 106602 (2014).
- S. M. Rossnagel, I. C. Noyan, and C. Cabral, *Phase Transformation of Thin Sputter-Deposited Tungsten Films at Room Temperature*, J. Vac. Sci. Technol., B **20**, 2047 (2002).

- T. Saburo and M. Sadamichi, *Spin Current, Spin Accumulation and Spin Hall Effect*, Sci. Technol. Adv. Mater. **9**, 014105 (2008).
- E. Saitoh, M. Ueda, H. Miyajima, and G. Tatara, *Conversion of Spin Current into Charge Current at Room Temperature: Inverse Spin-Hall Effect*, Appl. Phys. Lett. **88**, 182509 (2006).
- C. W. Sandweg, Y. Kajiwara, A. V. Chumak, A. A. Serga, V. I. Vasyuchka, M. B. Jungfleisch, E. Saitoh, and B. Hillebrands, *Spin Pumping by Parametrically Excited Exchange Magnons*, Phys. Rev. Lett. **106**, 216601 (2011).
- D. Sangeeta and J. R. LaGraff, in *Inorganic Materials Chemistry Desk Reference, Second Edition* (CRC Press, 2004).
- J. Sarkar, in *Sputtering Materials for VLSI and Thin Film Devices* (William Andrew Publishing, Boston, 2014), pp. 291.
- M. Sasikanth, E. N. Dmitri, and A. Y. Ian, *Energy-Delay Performance of Giant Spin Hall Effect Switching for Dense Magnetic Memory*, Appl. Phys Express **7**, 103001 (2014).
- C. S. Selvanayagam, J. H. Lau, Z. Xiaowu, S. K. W. Seah, K. Vaidyanathan, and T. C. Chai, *Nonlinear Thermal Stress/Strain Analyses of Copper Filled TSV (through Silicon Via) and Their Flip-Chip Microbumps*, IEEE Trans. Adv. Packag. **32**, 720 (2008).
- J. J. Senkevich, T. Karabacak, D. L. Bae, and T. S. Cale, *Formation of Body-Centered-Cubic Tantalum Via Sputtering on Low-Kappa Dielectrics at Low Temperatures*, J. Vac. Sci. Technol. B **24**, 534 (2006).
- Y. G. Shen and Y. W. Mai, *Influences of Oxygen on the Formation and Stability of Al₁₅β-W Thin Films*, Mater. Sci. Eng., A **284**, 176 (2000).
- Y. G. Shen, Y. W. Mai, W. E. McBride, Q. C. Zhang, and D. R. McKenzie, *Structural Properties and Nitrogen-Loss Characteristics in Sputtered Tungsten Nitride Films*, Thin Solid Films **372**, 257 (2000).
- M. Shin'ichi, *Ta/W/AlO_x-Al/Ta/Nb Josephson Junctions for X-Ray Detector*, Jpn. J. Appl. Phys. **34**, L1352 (1995).
- A. K. Sinha, *Topologically Close-Packed Structures of Transition Metal Alloys*, Prog. Mater Sci. **15**, 81 (1972).
- J. Sinova, D. Culcer, Q. Niu, N. A. Sinitsyn, T. Jungwirth, and A. H. MacDonald, *Universal Intrinsic Spin Hall Effect*, Phys. Rev. Lett. **92**, 126603 (2004).
- J. Sinova, S. O. Valenzuela, J. Wunderlich, C. H. Back, and T. Jungwirth, *Spin Hall Effects*, Rev. Mod. Phys. **87**, 1213 (2015).
- H. L. Skriver and N. M. Rosengaard, *Surface Energy and Work Function of Elemental Metals*, Phys. Rev. B **46**, 7157 (1992).
- M. Stavrev, D. Fischer, F. Praessler, C. Wenzel, and K. Drescher, *Behavior of Thin Ta-Based Films in the Cu/Barrier/Si System*, J. Vac. Sci. Technol., A **17**, 993 (1999).

- M. Suenaga, in *Superconductor Materials Science: Metallurgy, Fabrication, and Applications*, edited by S. Foner, and B. B. Schwartz (Springer US, Boston, MA, 1981), pp. 201.
- K. Suguro, Y. Nakasaki, T. Inoue, S. Shima, and M. Kashiwagi, *Reaction Kinetics in Tungsten/Barrier Metal/Silicon Systems*, *Thin Solid Films* **166**, 1 (1988).
- N. Susa, S. Ando, and S. Adachi, *Properties of Tungsten Film Deposited on GaAs by RF Magnetron Sputtering*, *J. Electrochem. Soc.* **132**, 2245 (1985).
- C. C. Tang and D. W. Hess, *Plasma-Enhanced Chemical Vapor Deposition of β -Tungsten, a Metastable Phase*, *Appl. Phys. Lett.* **45**, 633 (1984).
- X. D. Tao, Z. Feng, B. F. Miao, L. Sun, B. You, D. Wu, J. Du, W. Zhang, and H. F. Ding, *The Spin Hall Angle and Spin Diffusion Length of Pd Measured by Spin Pumping and Microwave Photoresistance*, *J. Appl. Phys.* **115**, 17C504 (2014).
- A. C. Thompson, Y. Wu, J. H. Underwood, and T. W. Barbee, *Focussing of Synchrotron Radiation X-Ray Beams Using Synthetic Multilayer Mirrors*, *Nucl. Instrum. Methods Phys. Res., Sect. A* **255**, 603 (1987).
- J. A. Thornton, *Influence of Apparatus Geometry and Deposition Conditions on the Structure and Topography of Thick Sputtered Coatings*, *J. Vac. Sci. Technol.* **11**, 666 (1974).
- Y. Tserkovnyak, A. Brataas, and G. E. W. Bauer, *Enhanced Gilbert Damping in Thin Ferromagnetic Films*, *Phys. Rev. Lett.* **88**, 117601 (2002).
- W. R. Tyson and W. A. Miller, *Surface Free Energies of Solid Metals: Estimation from Liquid Surface Tension Measurements*, *Surf Sci.* **62**, 267 (1977).
- Y. Utsumi, H. Kyuragi, T. Urisu, and H. Maezawa, *Tungsten-Beryllium Multilayer Mirrors for Soft X Rays*, *Appl. Opt.* **27**, 3933 (1988).
- S. O. Valenzuela and M. Tinkham, *Direct Electronic Measurement of the Spin Hall Effect*, *Nature* **442**, 176 (2006).
- T. J. Vink, W. Walrave, J. L. C. Daams, A. G. Dirks, M. A. J. Somers, and K. J. A. van den Aker, *Stress, Strain, and Microstructure in Thin Tungsten Films Deposited by DC Magnetron Sputtering*, *J. Appl. Phys.* **74**, 988 (1993).
- L. Vitos, A. V. Ruban, H. L. Skriver, and J. Kollár, *The Surface Energy of Metals*, *Surf Sci.* **411**, 186 (1998).
- F. T. N. Vüllers and R. Spolenak, *Alpha- Vs. Beta-W Nanocrystalline Thin Films: A Comprehensive Study of Sputter Parameters and Resulting Materials' Properties*, *Thin Solid Films* **577**, 26 (2015).
- B. Wang, *Ultrahigh Density Magnetic Recording Media: Quantitative Kinetic Experiments and Models of the $A1$ to $L1_0$ Phase Transformation in FePt and Related Ternary Alloy Films*, PhD Thesis, Carnegie Mellon University, Pittsburgh, PA, 2011.
- F. E. Wang, *Some Crystal Chemical Aspects of $A_3B(\beta-W)$ Type Compounds*, *J. Solid State Chem.* **6**, 365 (1973).

- G.-C. Wang and T.-M. Lu, in *Rheed Transmission Mode and Pole Figures: Thin Film and Nanostructure Texture Analysis* (Springer New York, New York, NY, 2014), pp. 133.
- X. Wang, C. O. Pauyac, and A. Manchon, *Spin-Orbit-Coupled Transport and Spin Torque in a Ferromagnetic Heterostructure*, *Phys. Rev. B* **89**, 054405 (2014).
- I. A. Weerasekera, S. I. Shah, D. V. Baxter, and K. M. Unruh, *Structure and Stability of Sputter Deposited Beta-Tungsten Thin Films*, *Appl. Phys. Lett.* **64**, 3231 (1994).
- W. L. Winterbottom, *Equilibrium Shape of a Small Particle in Contact with a Foreign Substrate*, *Acta Metall.* **15**, 303 (1967).
- H. S. Witham, P. Chindaudom, I. An, R. W. Collins, R. Messier, and K. Vedam, *Effect of Preparation Conditions on the Morphology and Electrochromic Properties of Amorphous Tungsten Oxide Films*, *J. Vac. Sci. Technol., A* **11**, 1881 (1993).
- H. A. Wittcoff, B. G. Reuben, and J. S. Plotkin, *Industrial Organic Chemicals* (Wiley, New Jersey, 2012), 3rd edn.
- S. A. Wolf, D. D. Awschalom, R. A. Buhrman, J. M. Daughton, S. von Molnár, M. L. Roukes, A. Y. Chtchelkanova, and D. M. Treger, *Spintronics: A Spin-Based Electronics Vision for the Future*, *Science* **294**, 1488 (2001).
- S. A. Wolf, A. Y. Chtchelkanova, and D. M. Treger, *Spintronics - a Retrospective and Perspective*, *IBM J. Res. Dev.* **50**, 101 (2006).
- S. Yoshihiko, *Tungsten-Carbon X-Ray Multilayered Mirror Prepared by Photo-Chemical Vapor Deposition*, *Jpn. J. Appl. Phys.* **28**, 920 (1989).
- S. Zhang, *Spin Hall Effect in the Presence of Spin Diffusion*, *Phys. Rev. Lett.* **85**, 393 (2000).
- W. Zhang, V. Vlaminck, J. E. Pearson, R. Divan, S. D. Bader, and A. Hoffmann, *Determination of the Pt Spin Diffusion Length by Spin-Pumping and Spin Hall Effect*, *Appl. Phys. Lett.* **103**, 242414 (2013).
- A. Zunger and M. L. Cohen, *Self-Consistent Pseudopotential Calculation of the Bulk Properties of Mo and W*, *Phys. Rev. B* **19**, 568 (1979).
- I. Žutić, J. Fabian, and S. Das Sarma, *Spintronics: Fundamentals and Applications*, *Rev. Mod. Phys.* **76**, 323 (2004).